12-17-2010

Estuarine Dynamics as a Function of Barrier Island Transgression and Wetland Loss: Understanding the Transport and Exchange Processes

Jennifer Schindler
University of New Orleans

Estuarine Dynamics as a Function of Barrier Island Transgression and Wetland Loss: Understanding the Transport and Exchange Processes

A Thesis

Submitted to the Graduate Faculty of the
University of New Orleans
in partial fulfillment of the
requirements for the degree of

Master of Science
in
Earth and Environmental Science
Coastal Sciences

by

Jennifer Schindler

B.S. University of New Orleans, 2008

December, 2010

ACKNOWLEDGMENTS

I consider this master's thesis to be a major accomplishment in my life. Therefore, I owe my deepest gratitude to all those who have made this thesis a possibility. First, I would like to thank my major professor, Dr. Ioannis Georgiou, who has taught me most of what I know about numerical modeling while working for him over the last 4 years. This research would not have been possible if it were not for his guidance and support. On a similar note, I would like to thank my committee members, Dr. Mark Kulp and Dr. Alex McCorquodale for their expertise and advice not just during this research, but throughout my undergraduate and graduate career as well. The field data used in this research would not exist if it were not for the people responsible for the field deployments and retrievals: Mike Brown, Chris Esposito, Dr. Ioannis Georgiou, Phil McCarty, Kevin Trosclair, and Dallon Weathers. Funding provided by the USGS Northern Gulf of Mexico (NGOM) Ecosystem Change and Hazard Susceptibility Project made field efforts and research work possible. Therefore, I would like to thank this organization for its generosity and support. To my friends, family, teachers, and colleagues who provided help and encouragement over the years, I would like to extend my deepest gratitude and appreciation. Finally, I would like to thank Mr. David Billesbach, my high school teacher and Environmental Science Club sponsor, for encouraging the passion I have for science. I cannot begin to describe how much I value the lessons learned during my time as his student. Thanks to you all!

TABLE OF CONTENTS

LIST OF FIGURES

LIST OF TABLES

ABSTRACT

The Northern Gulf of Mexico and coastal Louisiana are experiencing accelerated relative sea level rise rates; therefore, the region is ideal for modeling the global affects of sea level rise (SLR) on estuarine dynamics in a transgressive barrier island setting. The field methods and numerical modeling in this study show that as barrier islands are converted to inner shoals, tidal exchange increases between the estuary and coastal ocean. If marshes are unable to accrete at a pace comparable to SLR, wetlands will deteriorate and the tidal exchange and tidal prism will further increase. Secondary to hurricanes, winter storms are a primary driver in coastal morphology in this region, and this study shows that wind direction and magnitude, as well as atmospheric pressure change greatly affect estuarine exchange. Significant wetland loss and winter storm events produce changes in local and regional circulation patterns, thereby affecting the hydrodynamic exchange and resulting transport.

Keywords: tidal exchange, 3-Dimensional numerical modeling, tidal prism, circulation, sea level rise, winter storms, FVCOM, Gulf of Mexico, barrier islands, wetland loss

CHAPTER 1

Introduction

On low gradient continental shelves around the world, including the northern Gulf of Mexico (Figure 1), the abandonment of an active delta lobe due to upstream avulsion and reduced sediment supply leads to barrier island development across interdistributary bays (Penland, Boyd, and Suter, 1988; Roberts, 1997). These processes follow a conceptual model described by Penland, Boyd, and Suter (1988). This three-stage model explains how deltaic headlands submerge and sediment is reworked by marine processes, eventually forming barrier islands. As these processes continue, eroding headlands produce spit systems and breaching events generate inlets. Tidal inlets control the exchange between the coastal ocean and interior bays and sounds; therefore, they strongly influence the evolution of barrier islands. An increase in the size of tidal inlets causes an increase in the tidal prism, or volume of water passing through the tidal inlet (O'Brien, 1969; Jarrett, 1976; Hughes, 2002). After continued transgression due to longshore and cross-shore transport and with effects from rising sea levels, only inner-shelf shoals will remain. Marine processes cause these subaqueous sand bodies to slowly migrate landward (Penland, Boyd, and Suter, 1988; Roberts, 1997).

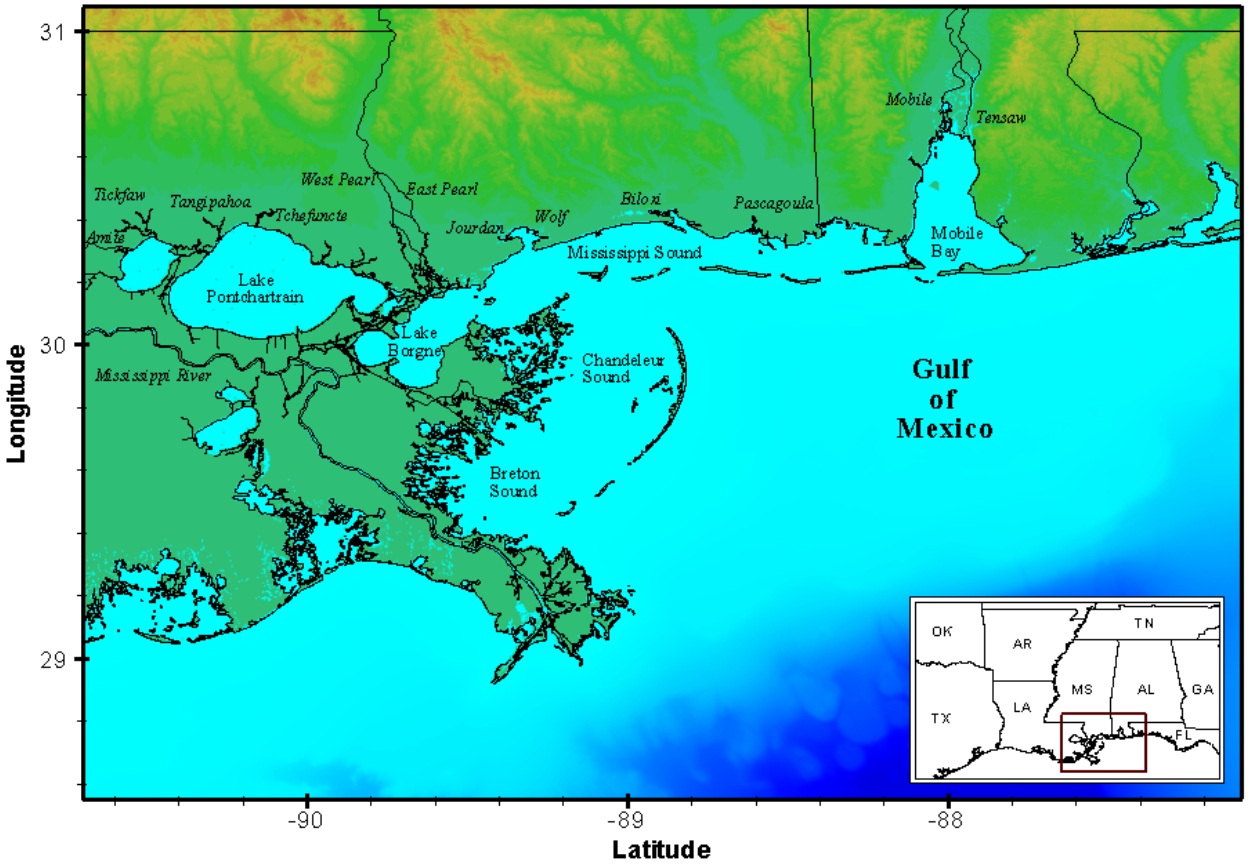

Figure 1 – The inset shows a map of the states surrounding the northern Gulf of Mexico, while the red box outlines the area shown in the large image. The large image is a relief map of the region surrounding the northern Gulf of Mexico (the study area) with water bodies and rivers labeled.

The major initiators of shoreline evolution in these transgressive depositional systems are the supply of sediment and its composition, the rate of sea level rise, and the frequency and intensity of tropical and winter storms (Georgiou *et al.*, 2010; Georgiou, FitzGerald, and Stone,

2005). These factors directly determine wetland loss or gain, tidal exchange, and the bay tidal prism (Georgiou *et al.*, 2010; FitzGerald *et al.*, 2008). Presently, the Chandeleur Island arc, created when the Mississippi River abandoned the St. Bernard Delta complex, is fragmented with subaqueous shoals at both ends of the barrier island arc. The impact of major storms and the asymmetry in longshore transport along the islands (Georgiou and Schindler, 2009) will likely accelerate this process until, in the absence of an active littoral zone, cross-shore transport begins to dominate (Miner *et al.*, 2009; Twichell *et al.*, 2009).

Therefore, the Chandeleur Islands serve as a model for transgressive barrier islands having a limited supply of sand along storm-dominated coasts. Recent studies (Sallenger *et al.*, 2009) show that the Chandeleur Islands have lost 86% of their subaerial exposure during Hurricane Katrina in 2005, and an additional 20% during winter, extra-tropical, and tropical storms in the three years following hurricane Katrina. Therefore, this system provides a unique opportunity to study the estuarine dynamics during this transitional stage from barrier arc to segmented sandy shoals in a regime of accelerated sea-level-rise (SLR) and increased storminess(Goldenberg *et al.*, 2001; Emanuel, 2005; Blum and Roberts, 2009).

Two key objectives of this research were to obtain physical measurements from the interior bay or sound landward of the Chandeleur Islands and to investigate (through numerical modeling) exchange processes during moderate-energy conditions, such as those produced by winter storms. These storms are important to the region's morphology, as they have a higher frequency of occurrence than tropical storms and hurricanes. There are at least 20 to 40 winter storms each year in this area (Georgiou, FitzGerald, and Stone, 2005).

The key research questions included the following: (1) During barrier fragmentation, to what degree will the exchange between the coastal ocean and back-barrier basins influence the transport and mixing processes of conservative and dissolved substances; (2) Does an increase in the tidal exchange along barrier systems increase marine conditions in interior bays; (3) How does the astronomical forcing and spring neap variation influence tidal transport in back basins; and (4) How do estuarine dynamics in the bays respond to north/northwesterly wind direction, longer wind duration, and higher wind intensity during winter storms?

Background and Significance

Roberts (1997) describes the delta cycle as consisting of two phases: a regressive phase and a transgressive phase. Delta lobes are formed as streams capture sediment from runoff and well-defined river channels deliver sediment to wetlands and bays. Since the river has many distributaries and avulsions that vary with time, there can be many delta lobes per delta complex. Eventually the river will switch course and begin a new delta complex, starving the first delta complex of sediment input. The abandoned delta complex will subside due to compaction and deteriorate due to marine processes. This transgressive reworking forms beaches, spits, barrier islands, and, finally, subaqueous shoals. In this way, the Mississippi River has built the wetlands, bayous, barrier islands, natural levees, and tidal channels of the Mississippi Delta Plain.

To better describe the response of barrier islands to this deltaic abandonment, Penland, Boyd, and Suter (1988) created a three-stage conceptual model describing the geomorphologic stages of transgressive depositional systems. In this model, once the river has abandoned the deltaic headland, longshore transport redistributes sand deposits from the erosional headland into recurved spits and flanking barrier islands (Stage 1; Figure 2). Submergence causes the barrier island arc, primarily occupied by tidal inlets and washover terraces, to detach from the headland (Stage 2; Figure 2). Continued submergence and storm attacks remove sediment from the system, which is already lacking in sediment input. This process transforms the barrier island into a sand shoal that slowly migrates landward due to marine processes (Stage 3; Figure 2).

The Chandeleur Island chain, as the oldest subaerial transgressive barrier island arc in the Mississippi River delta plain, has been an important feature in the southeastern Louisiana topography. Barrier islands form the first line of defense in protecting coastal wetlands and shorelines from the direct effects of wind, waves, and storm surge, especially during tropical events (Stone and McBride, 1998; Stone, Zhang, and Sheremet, 2005). Additionally, barrier islands aid in the establishment of estuarine gradients (Reyes *et al.*, 2005). Therefore, these features create a transition zone between marine and freshwater environments, as well as offer subaerial nesting habitat for shorebirds, shallow habitat nurseries for marine life, and spawning grounds for fisheries (Reyes *et al.*, 2005; van Heerden and DeRouen, 1997).

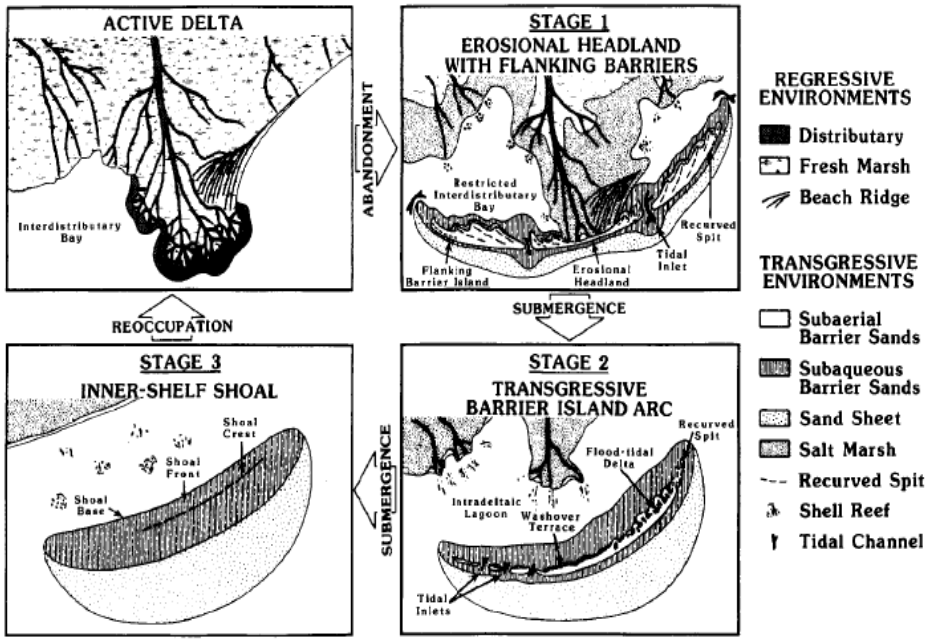

Figure 2 - The Penland Model of transgressive depositional systems describes three stages of geomorphology including Stage 1 with erosional flanking barriers, Stage 2 with a transgressive barrier island arc, and Stage 3 with a transformation to inner-shelf shoals (Penland, Boyd, and Suter, 1988).

The Chandeleur Islands, however, are rapidly transforming into subaqueous sand shoals, fragmenting, and undergoing shoreface erosion (Lavoie *et al.*, 2009). These islands, unlike most transgressive barrier islands, are experiencing transgressive submergence and in-place drowning, not migrating landward (Fearnley *et al.*, 2009). Dominant winds from the southeast and tropical cyclone-related wind-waves promote persistent net northerly longshore sediment transport along the barrier island chain (Georgiou and Schindler, 2009). Due to decreasing sediment supply, this northerly transport trend has resulted in the formation of a large subtidal recurved spit extending to Hewes Point (Twichell *et al.*, 2009). Shoreline erosion rates in the area range from 13.7 ft/yr to 18 ft/yr (Penland *et al.*, 2005). This shoreline erosion, in addition to reduced sediment supply, continuous wave attack during frontal weather, and impacts produced by tropical storms, has increased wave and inundation overwash, reduced the Chandeleur Islands' subaerial extent, and increased the frequency of tidal inlets along the barrier island chain(Georgiou and Schindler, 2009; Lavoie *et al.*, 2009). As tidal inlets become larger and more frequent, the transition zone between the coastal ocean and estuarine environments diminishes. Since inlets dominate the processes responsible for barrier island migration through cross-shore sediment transport (Rosati and Stone, 2009), they are the likely pathways for other particulates and water exchange as well.

Understanding the relationship between barrier island fragmentation and tidal prism, therefore, is imperative in predicting changes to the interior wetlands and coastline.

Miner et al. (2009) state that the drastic and unpredictable nature of changes in tidal inlets results from "complex bathymetry and resulting wave refraction patterns, as well as increased wave-generated and tidal current-induced sediment transport." While there has been little research previously conducted to study the effect of barrier island fragmentation (and therefore tidal inlet formation) on estuarine exchange (FitzGerald *et al.*, 2007; FitzGerald *et al.*, 2008; Feng, 2009; Feng and Li, 2010), there have been numerous studies that attempt to define a relationship between an area's tidal prism and tidal inlet cross-sectional area (O'Brien, 1969; Jarrett, 1976; Hughes, 2002).

Most recently, D' Alpaos *et al.* (2010) tested the applicability of such an empirical relationship for sheltered inlets:

$$\Omega = kP^{\alpha} \qquad \text{(Eqn. 1)}$$

where Ω is the cross-sectional area of the tidal inlet in m^2, P is the tidal prism in m^3, and α typically ranges from 0.85 to 1.10 (O'Brien, 1969; Jarrett, 1976; Hughes, 2002). Using one-dimensional numerical modeling, D' Alpaos et al. (2010) found that a value of $k = 1.3 \times 10^{-3}$ $m^{2-3\alpha}$ and $\alpha = 0.67$ (as originally derived empirically by O'Brien (1969) and theoretically by Marchi (1990)) produced results concurrent with observational data. Deemed accurate by D' Alpaos et al. (2010), the Marchi Law (Marchi, 1990) relates *k* to the channel width:

$$k \sim B^{1/7} \qquad \text{(Eqn. 2)}$$

where *B* is the channel width in meters. These theoretical relationships, however, may not apply to inlets on open coasts (D' Alpaos *et al.*, 2010), due in part to the effects of longshore transport , sediment transport due to direct and intense wave attack, and wetting and drying of neighboring marshes. Additionally, D' Alpaos *et al.* (2010) proved that for larger tidal inlets and prisms, $\alpha = 0.67$ is more appropriate in Equation 1. For tidal inlet cross-sectional areas less than 50 m^2 and/or tidal prisms less than 10^6 m^3, the tidal prism changes at a much faster rate than the tidal inlet cross-sectional area.

In a report by Jarrett (1976), data were used to establish a regression equation for Gulf of Mexico tidal inlets with and without jetties. The data used displayed more scatter than in other regions such as the east coast (Jarrett, 1976), and therefore the regression equation may not be entirely accurate. Jarrett (1976) proposes that this scatter is the result of the Gulf of Mexico's microtidal environment, which varies from diurnal to semi-diurnal depending on geographic location and declination of the moon. To reduce uncertainty, tidal inlet cross-sectional areas used to establish this equation were measured during diurnal tide conditions, since the inlet cross-sectional areas in the Gulf coast region are largely influenced by prior astronomical and/or meteorological effects (Jarrett, 1976). For unjettied or single-jettied inlets along the Gulf Coast, this relationship is:

$$A = 3.51 \times 10^{-4} V^{0.86} \qquad \text{(Eqn. 3)}$$

where *A* is the minimum cross-section of the entrance channel measured below mean sea level (ft^2) and *V* is the tidal prism corresponding to the diurnal or spring range of tide (ft^3).

Tidal inlets form major transport pathway across the Chandeleur Islands, since overwash events are only common during storm events. As tidal inlet size and frequency increase, the exchange between the coastal ocean and estuary, as well as the possibility for wave energy to

intensify landward of the islands per unit length along a cross-shore profile, increases (Georgiou and Schindler, 2009). Both astronomical and meteorological effects influence this exchange. Studies show that winds along the long axis of the Chandeleur/Breton Sound cause extensive setup (~0.2 m with 9 m/s wind speeds) along the downwind coast, but currents and water levels rapidly normalize within three hours when the wind stops (Hart and Murray, 1978). During cold front conditions, waves are fetch-limited within the sounds and depth-limited over shoals and near islands (Keen, 2002). These dynamic conditions can provide additional controls and ultimately further increase the exchange between the coastal ocean and interior bays and sounds.

Relationships that describe the morphological changes anticipated with variations in tidal prism or tidal inlet cross-sectional area can be applied to better understand the effects of sea level rise on barrier islands, interior wetlands, and back-basins (FitzGerald *et al.*, 2008). If marshes are unable to accrete at the same rate as SLR, wetlands will convert to open water under the effects of SLR. This transition will increase the tidal exchange, thereby increasing tidal prism (FitzGerald *et al.*, 2008). Moreover, shoreline change analysis as a function of recent tropical storm activity predicts (through extrapolation) that if the current storm activity persists, the shoreline along the barrier arc would intercept the edge of the back-barrier marsh of the Chandeleur Islands, and could vanish as soon as 2013 (Fearnley *et al.*, 2009). This back-barrier stabilizes the islands by promoting sediment accumulation and reducing wave energy (FitzGerald *et al.*, 2008; Lavoie *et al.*, 2009). Therefore, the Chandeleur Islands in the northern Gulf of Mexico (NGOM) will serve as an ideal model for areas experiencing transgressive processes under the effects of SLR and increased storm activity (Goldenberg *et al.*, 2001; Emanuel, 2005).

Key Hypotheses

Hypothesis 1: A threshold crossing of barrier islands to inner shoals will not increase the tidal prism if the interior marsh's accretion rate is equal to or exceeds the relative sea level rise (RSLR) rate.

Hypothesis 2: If the interior marsh is not able to accrete at the same rate as RSLR, then the bay area will increase thereby causing an increase in the tidal prism. This process may be accelerated during barrier island fragmentation and increase the exchange between interior bays and the coastal ocean.

Research Questions

- During barrier island fragmentation and transgression, to what degree will the exchange between the coastal ocean and back-barrier basins influence the transport and mixing processes of conservative and dissolved substances?
- Does an increase in the tidal exchange along barrier systems increase marine conditions in interior bays?
- How does the astronomical forcing and spring neap variation influence tidal transport in back-basins? How does this variability affect circulation and transport trends in the estuary?
- How do estuarine dynamics in the bays respond to north/northwesterly wind direction, longer wind duration, and higher wind intensity during winter storms?

CHAPTER 2

Study Area

Mississippi Delta Plain

The Mississippi River collects sediment from approximately 70% of the continental United States and parts of two Canadian provinces, a drainage basin totaling 3,344,560 km^2 (Coleman, 1988). The Holocene MDP includes over one-third of southern Louisiana (more than 30,000 km^2), its coastline spanning from Vermillion Bay in the west to the Chandeleur Islands in the east (Georgiou *et al.*, 2010). The Mississippi River has been depositing sediment since the Late Jurassic epoch (over 7000 years BP), occupying many delta complexes in this time (Georgiou *et al.*, 2010; Frazier, 1967; Coleman, 1988; Penland, Boyd, and Suter, 1988). As changes in upstream river avulsions and distributaries occur, the river takes a new course and deposits sediment to form a new delta complex in the process (Roberts, 1997). Overall, the Holocene MDP has occupied six delta complexes: the Maringouin (7,500 - 5,000 yrs BP), Teche (5,500 – 3,800 yrs BP), St. Bernard (4,000 – 2,000 yrs BP), Lafourche (2,500 – 400 yrs BP), Balize (1,000 yrs BP – present), and Atchafalaya (400 yrs BP – present) (Figure 3) (Frazier, 1967; Coleman, 1988; Penland, Boyd, and Suter, 1988; Roberts, 1997). Much of the MDP has a foundation of 10 to 15 km thick Mesozoic and Cenozoic sediment overlying a highly attenuated crystalline basement that was formed during Late Paleozoic fragmentation of the Pangaea landmass (Georgiou *et al.*, 2010).

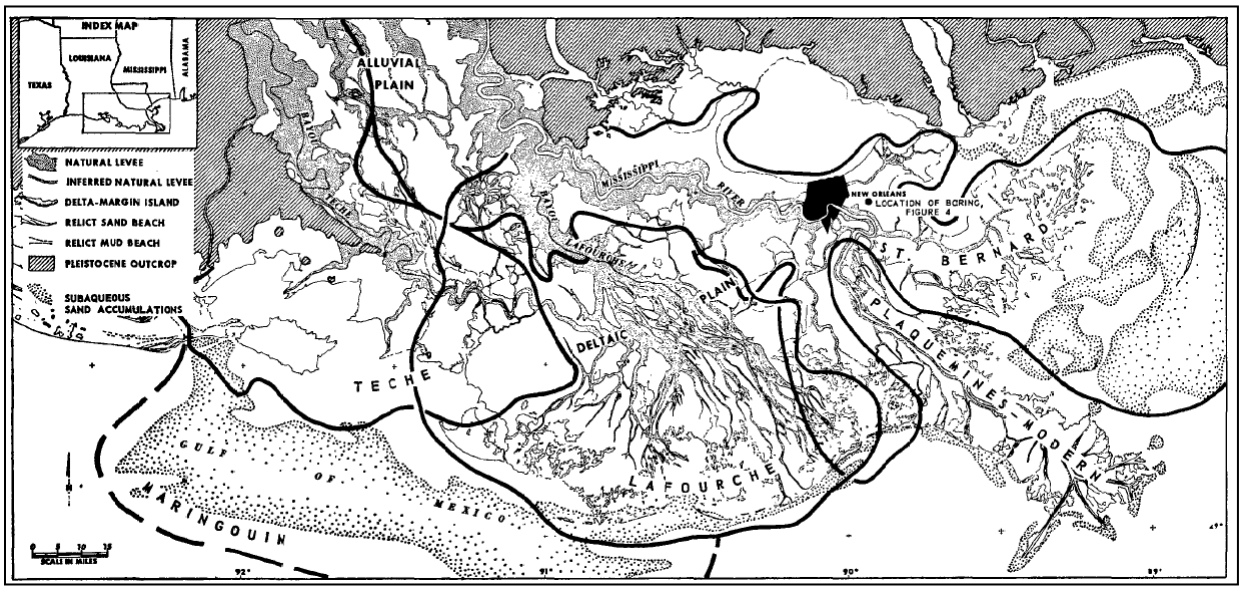

Figure 3 - A map of the six delta complexes within the Holocene MDP. The two active complexes are the Atchafalaya and Modern (Balize) complex (Frazier, 1967).

It is estimated that the main channel of the Mississippi River transports approximately 150 million metric tons of sediment to the Gulf of Mexico annually (Meade and Moody, 2008; Thorne *et al.*, 2008; Horowitz, 2010). However, the Mississippi River's discharge has been reduced significantly (from ~ 400 million metric tons/yr) over the last century due to the construction of artificial levees and dams, changes in soil conservation practices, and other anthropogenic alterations along the Mississippi River (Keown, Dardeau, and Causey, 1986; Milliman and Syvitski, 1992). This reduction in sediment supply due to human effects as well as eustatic sea-level rise, salt-water intrusion, and subsidence has caused unprecedented coastal change. Since the 1960's, the MDP has been recognized as a region with the highest wetland land loss rates on Earth - maximum rates reached 102 km^2/yr in the 1970's (Allison and Meselhe, 2010; Day *et al.*, 2000;

Barras *et al.*, 2003). Other physical processes such as wave-generated longshore sediment transport, storm-driven sediment transport, bay and estuarine tidal exchange and circulation, inlet hydraulics, and bay-wetland interaction play a role in coastal morphology; however, these processes generally remain constant with time (Georgiou *et al.*, 2010).

Pontchartrain Estuary

The Pontchartrain Estuary stretches over the Florida Parishes of Louisiana in the Gulf Coast Plain and the entire MDP (Figure 4). As one of the largest estuaries in the NGOM, the Pontchartrain Estuary includes more than 12,000 km^2 of southeast Louisiana (Georgiou *et al.*, 2009). The upper Pontchartrain Estuary is composed of three lakes (from west to east - Maurepas, Pontchartrain, and Borgne). Natural tidal channels and artificial navigation complexes connect these lakes. The estuary occupies a shallow depression between the alluvial ridge of the Mississippi River to the west, the sloping uplands to the north, the Pearl River basin to the east, and the Mississippi Sound to the southeast (U.S. Army Corps of Engineers New Orleans District, 1982; Kindinger, 1988). Two natural tidal passes connect these lakes to the Breton, Chandeleur, and Mississippi Sounds: the Rigolets (opening into Lake Borgne/Western Mississippi Sound) and the Chef Menteur (opening into Lake Borgne).

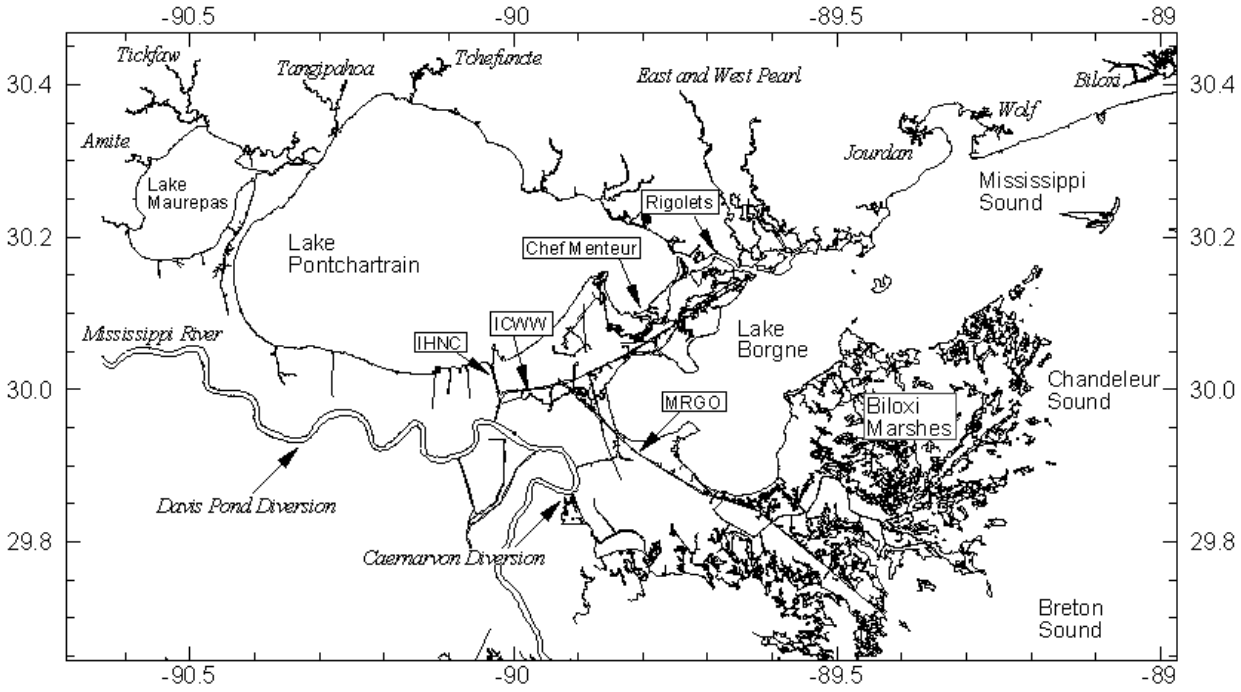

Figure 4 - Map of the upper and central Pontchartrain Estuary. River names are shown in italics. (Figure adapted from Georgiou et al., 2009.)

Additionally, an artificial navigation canal, the Inner Harbor Navigation Canal (IHNC), is located on the south of Lake Pontchartrain and opens into the Intracoastal Waterway (ICWW) and the Gulf of Mexico through the Mississippi River Gulf Outlet (MRGO). The MRGO, authorized by the River and Harbor Act of 1956 as an alternate navigation route to the port of New Orleans, was constructed from 1958 through 1968. It was de-authorized in 2009 due to a number of channel enlargements due to shoreline erosion by tidal currents and vessel wakes, saltwater intrusion, increased conveyance during storms, and other negative effects (Lake Pontchartrain Basin Foundation, 2006). Prior to MRGO closure, flow distribution among the three main passes during

spring tides (IHNC, Chef Menteur, and the Rigolets) was approximately 6%, 30%, and 64% respectively (Haralampides, 2000).

Barataria Basin

The Barataria Basin is bordered by Bayou Lafourche on the west and the Plaquemines delta lobe to the east (Figure 5). The sediment transported through these distributary headlands formed the barrier islands between Barataria Bay and the Gulf of Mexico as well as the area's beach ridge/Chenier systems (FitzGerald *et al.*, 2007; Georgiou *et al.*, 2010). Caminada Pass, Barataria Pass, Pass Abel, and Quatre Bayou are the principal tidal inlets that control the flux of water and nutrients between Barataria Bay and the Gulf of Mexico. Additionally, tidal channels connect Barataria Bay to a series of oligohaline lakes by way of tidal channels known as bayous. The region is comprised of extensive wetlands that transition from saltwater to freshwater marsh along the modern salinity gradient.

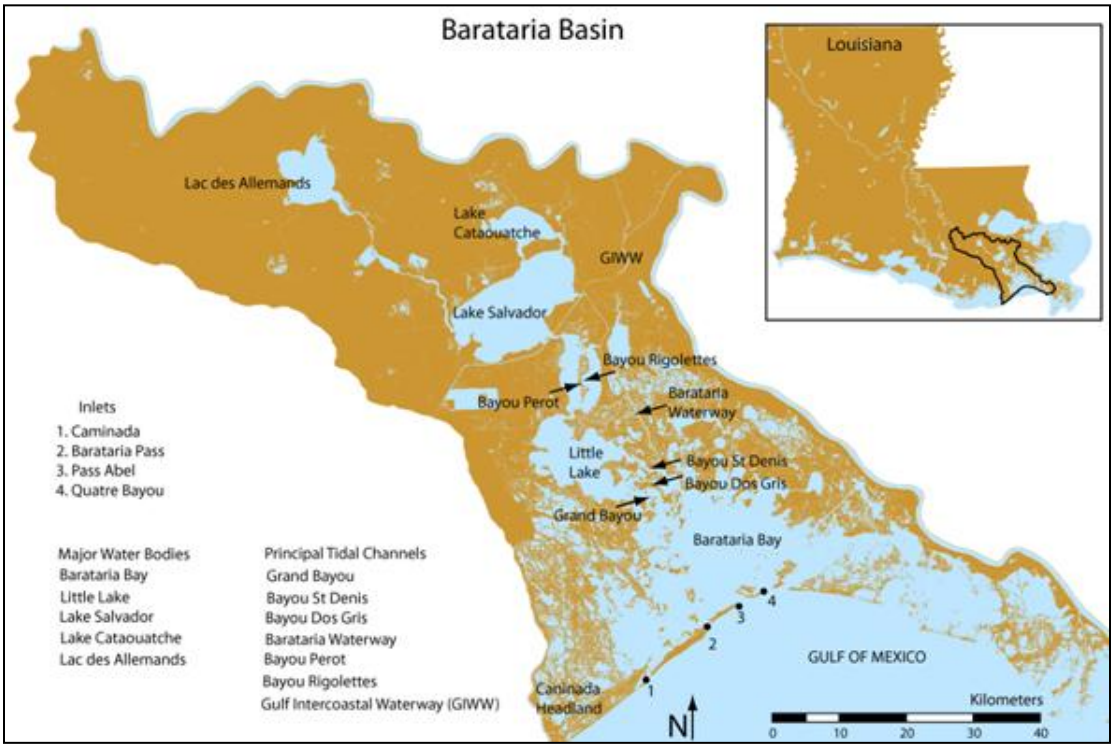

Figure 5 - Principal hydrodynamic features within Barataria Basin (Georgiou *et al.*, 2010).

Regional trends

Salinity

The Pontchartrain Estuary is shallow and mostly well-mixed (Haralampides, 2000). Salinity in the upper Pontchartrain Estuary is relatively low due to narrow tidal passes and subsequently small tidal fluctuations. Consequently, the estuarine gradient has a mild slope in the upper estuary in comparison to the lower estuary (Georgiou *et al.*, 2009)(Figure 6). Due to the shallow nature of the lakes, stratification in the Pontchartrain Estuary is rare except near the IHNC and the MRGO. At the other extreme, Meade (1972) and Geyer et al. (2004) suggest that the Mississippi River is one of the most highly stratified river-mouth estuaries in the world because of limited tidal and wave mixing and high freshwater input (Allison and Meselhe, 2010).

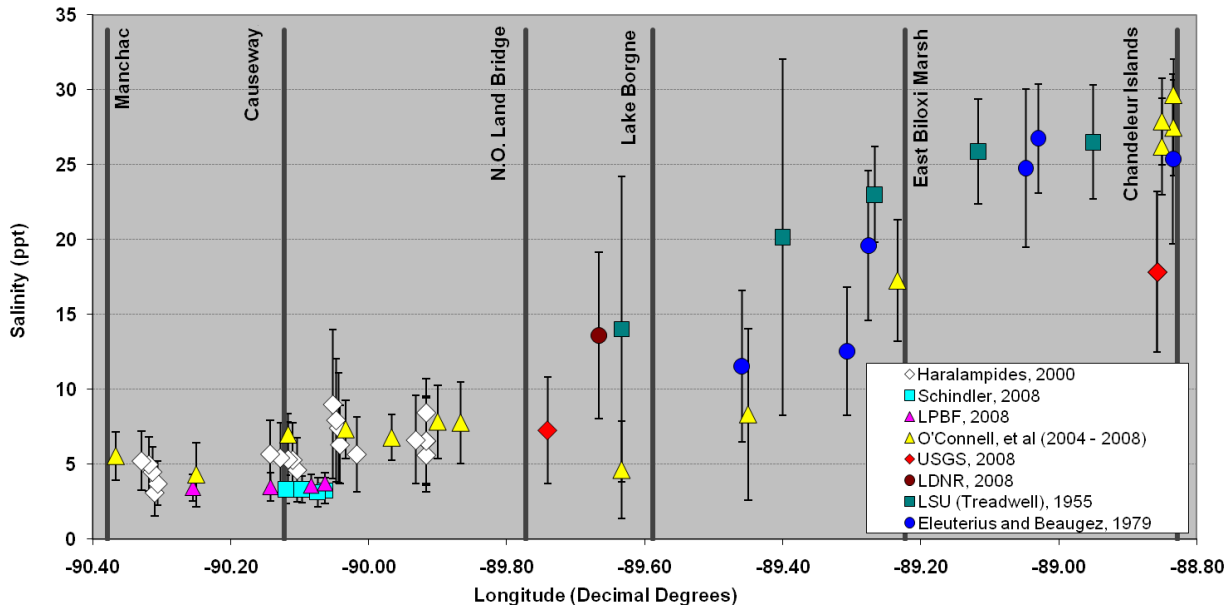

Figure 6 - Estuarine salinity gradients as a function of longitude; error bars represent one standard deviation (Georgiou *et al.*, 2009).

Salinity in Barataria Basin varies between the Upper, Middle, and Lower Barataria Basin. The Upper Barataria Basin, comprised of the area north of Lake Salvador, is a freshwater environment (less than 1 ppt). The Middle Barataria Basin, the region from Little Lake to Lake Salvador, is a transition zone with low to moderate salinities (approximately 6 ppt), while the Lower Barataria region, south of Little Lake, has marine salinities averaging between 14 and 18 ppt (Georgiou *et al.*, 2010).

Salinity along the Mississippi to Florida coast reduces to freshwater levels in estuaries near river discharges; this causes episodic stratification depending on the magnitude of river discharge (Shroeder, Dinnel, and Wiseman, 1990). Otherwise, the salinities along sandy coasts and barrier islands reflect Gulf of Mexico salinities (Shroeder, Dinnel, and Wiseman, 1990).

Waves and Tidal Signature

Mean annual significant wave height along the Louisiana coast varies from 0.95m to 0.5m for Barataria Bay and the Chandeleur Islands, respectively (Georgiou *et al.*, 2010; Georgiou, FitzGerald, and Stone, 2005). Meanwhile, the mean annual tidal range across the Louisiana coast is 0.3m (Georgiou *et al.*, 2010). The tidal range and signature along the coast decreases and changes from mixed with a strong diurnal component to strongly diurnal as one moves from the western edge of the coast toward the Chandeleur Islands (Georgiou, FitzGerald, and Stone, 2005). The tidal range in the region varies from 15 cm during the neap tidal cycle to 100 cm during the spring tidal cycle (Georgiou, FitzGerald, and Stone, 2005). The tropic tidal range in the Pontchartrain Estuary varies along the estuarine axis with a typical range in the central portion of the estuary (in Lake Pontchartrain) of approximately 0.15 m. Total exchange flow through the tidal passes during tropic ebb/flood tides is approximately 7,800 m^3/s, with approximately 1,000 m^3/s going through Pass Manchac (Haralampides, 2000). Tides near the Alabama and Florida coast are principally diurnal with an average range of 0.4 m, a maximum tropic tide range of 0.8 m, and a minimum equatorial tide range of 0.0m (Shroeder, Dinnel, and Wiseman, 1990; Marmar, 1954)

Due to low wave energy and microtidal regime throughout the region, the most dramatic changes to the NGOM's coast occur during winter storms and tropical/extratropical events (Georgiou, FitzGerald, and Stone, 2005; Stone *et al.*, 2004). Circulation currents in the region are

largely wind driven and vary in direction and magnitude (Georgiou and McCorquodale, 2002; Haralampides, 2000; Signell and List, 1997). During the winter cold front season, winds predominately come from the southeast and northwest before and after the frontal passage, respectively (Georgiou and Schindler, 2009). Frontal winds are approximately 15.3 m/s while postfrontal winds range from 18 to 24 m/s (Rosati and Stone, 2009). The region experiences one cold front per week (20 to 40 per year) on average, and waves generated offshore during these fronts can reach two to four meters (Stone, Zhang, and Sheremet, 2005; Georgiou, FitzGerald, and Stone, 2005; Georgiou *et al.*, 2010). Meteorological tides also have a significant effect on water levels in the region. With the passing of a cold front, water levels are elevated 0.3 to 0.9 m and can persist for days after the frontal passage (Boyd and Penland, 1981; Keen, 2002). It is the high frequency and spatial extent of cold fronts that make these storms such important factors in coastal geomorphology in the region (Keen, 2002; Georgiou, FitzGerald, and Stone, 2005; Rosati and Stone, 2009).

Tropical cyclones frequently affect the Gulf Coast region, causing high winds (and therefore increased wave heights) and storm surge for multiple hours. Ritchie and Penland (1988) indicate that the NGOM experiences one tropical storm or weak hurricane (Category 1 or 2) every 1.6 years and one moderate to severe hurricane (Category 3 and above) every 10 to 30 years. These tropical cyclones can produce storm surges of 1.0 to 5.0 m and deepwater wave heights of 5.0 to 20.0 m (Ritchie and Penland, 1985; Georgiou and Schindler, 2009)

Sea-level Rise

Eustatic (or global) sea-level rise (SLR) and subsidence play a major role in determining the deterioration of marshes. These factors, when combined, are referred to as relative sea level rise (RSLR). Subsidence is caused by natural processes such sediment compaction, faulting, and isostatic adjustments to regional crustal loading (Georgiou, FitzGerald, and Stone, 2005; Yuill, Lavoie, and Reed, 2009; Törnqvist *et al.*, 2006). Additional anthropogenic factors such as the withdrawal of gas, oil, and water from the earth by the petroleum industry contribute to subsidence (Morton *et al.*, 2005; Allison and Meselhe, 2010). Subsidence and RSLR across the Louisiana coastal zone affect coastal wetlands by increasing water levels relative to the marsh's surface elevation and slowly increasing salinities (Day *et al.*, 2000; Howes *et al.*, 2010; Reed, de Luca, and Foote, 1997). As plant species die due to increased salinity levels, the subsurface root structures disappear (Howes *et al.*, 2010). Without the reinforcing matrix of roots, the coastal wetlands are more vulnerable to wave attack and erosion (Howes *et al.*, 2010). It is very difficult to prove, however, that the conversion of marsh to open water has been caused by salt-water intrusion (Day *et al.*, 2000). Therefore, it will be described here as a factor in wetland loss. To survive, coastal marshes must respond to increases in relative sea level and prevent submergence through marsh accretion (Day *et al.*, 2007; Reed, de Luca, and Foote, 1997). If mineral sediments and organic material accumulates on or within the marsh soil at a rate equal to RSLR, then the relative position of the marsh surface will remain constant in relation to tidal flooding and drainage (Reed, de Luca, and Foote, 1997; Day *et al.*, 2007; Reed and Cahoon, 1993). When marsh accretion rates cannot match the rate of RSLR, the marsh is increasingly inundated by water until it eventually becomes submerged (Baumann, Day, and Miller, 1984; Reed, de Luca, and Foote, 1997)

The impact subsidence has on the MDP is substantial, as the rates of SLR and RSLR are 1.5 mm/yr and 10 mm/yr, respectively (Day *et al.*, 2007; Yuill, Lavoie, and Reed, 2009). However, as one moves away from the Mississippi River, subsidence rates differentially change or diminish according to the relative contribution of the specific mechanism(Yuill, Lavoie, and Reed, 2009; Blum and Roberts, 2009). Despite this reduction in subsidence as one moves toward the eastern edge of the NGOM, the entire coast is vulnerable to changes in eustatic sea level rise. The International Panel for Climate Change (2007) suggests that by the end of the century there will be an average

global sea-level rise increase of 0.18 to 0.59 m. These rates, with a lack of fluvial sediment input, are cause for concern for the health of wetlands in the region. At the Grand Isle tide gage in Barataria Bay, for instance, RSLR rates of 0.94 cm/yr over the last half century (from cumulative sources) have led to the conversion of more than 1,100 km^2 of wetlands to open water since 1935 (Georgiou *et al.*, 2010).

CHAPTER 3

Methods/Testing of Hypotheses

Both field methods and numerical modeling efforts were used to test research hypotheses. Field methods included moored deployments, which provided wave data and current profiles as well as near bottom salinity, temperature, pressure, and turbidity measurements at pre-determined locations (Figure 7). In an effort to determine transport pathways and magnitude at representative locations, current profiles and waves were determined at two locations: in the back-barrier of the barrier islands and in a deep-water tidal inlet.

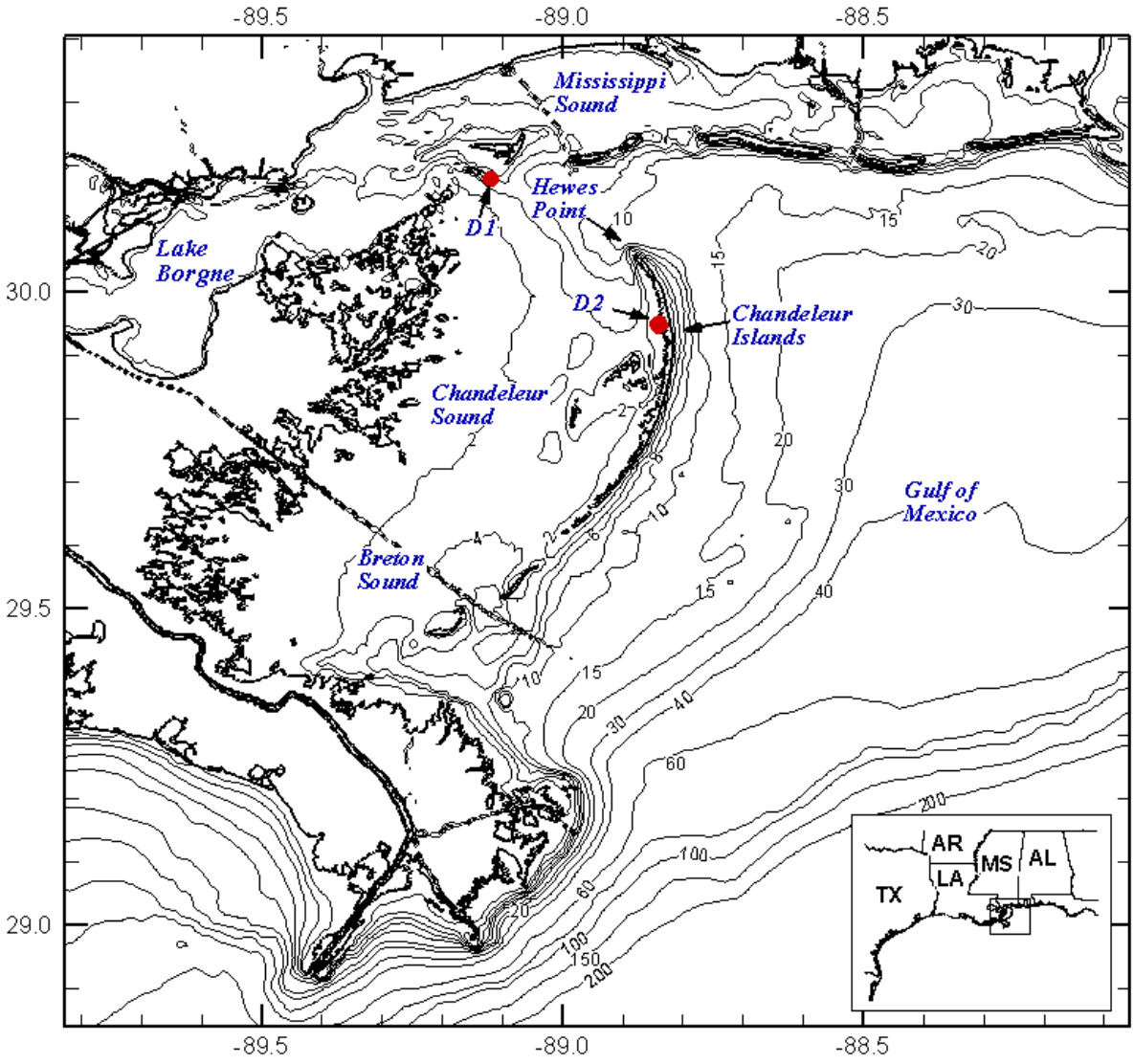

Figure 7 - The inset shows a map of the states surrounding the northern Gulf of Mexico, while the box outlines the area shown in the large image. The large image is a map of southeast Louisiana showing the regional bathymetry (meters) and coastline features as well as the location of the Chandeleur Islands (Georgiou and Schindler, 2009). Red circles indicate deployment locations (D1 and D2).

Data collected during the deployment period provided important current profiles and wave characteristics during winter storms, calm weather events (tidal conditions), and during intertidal conditions (March through May 2010). This data were used in conjunction with current, tidal, and meteorological stations to drive unsteady hydrodynamic models. These simulations provided local and regional hydrodynamics that were later used in model calibration and validation, estimation of flood and ebb volumes during normal conditions and during storms, and general circulation and transport trends throughout the basin. A numerical model was implemented to study the general effects of barrier island transgression in idealized basins. This allowed for conclusions and predictions to be made on a wider scale and in more generalized conditions. The goal of this generalized model was to formulate universal predictions for areas undergoing SLR and barrier island transgression.

Field Methods

Moored Deployments

The deep-water tidal channel deployment (D1) measured deep-water wave/velocity fields and collected continuous salinity-temperature data near a primary channel of hydrodynamic exchange between the Chandeleur/Mississippi Sound and the middle and upper Pontchartrain Estuary. The platform, deployed at location (30.18° N, 89.12° W) was located in a microtidal environment at a depth of approximately 11.2 m at mean tide level. The following instruments were mounted on an Oceanscience Barnacle platform from 3/1/2010 – 6/7/2010: a Sentinel Workhorse Monitor Acoustic Doppler Current Profiler (ADCP) (Burchard, 2002), a YSI 6600 multiparameter sonde, a RBR non-directional wave gauge rated for 50 m depths, and a Fiobuoy acoustic, submersible marine marker buoy. Details pertaining to each instrument's configuration can be found later in this section. The data from D1 were used to study the transient flow field and wave climate in the area. Additionally, the flow and waves observed were correlated to meteorological and astronomical events such as tides, wind events, etc.

The back-barrier deployment (D2) measured wave and velocity fields in a shallow back-barrier environment. Additionally, salinity, temperature, and turbidity were collected at this location (29.95° N, 88.84° W) using a Nortek Aquadopp Profiler, a YSI 6600 multiparameter sonde, and a non-directional wave gauge rated for 20 m depths. Mounted on a tripod deployment system, these units formed the back-barrier deployment system and collected data from 3/11/2010 to 5/6/2010.

The 1,200 kHz, upward facing ADCP was located approximately 0.5 m above the bed on the D1 deployment system. It used 2,159 total bursts (each burst containing 1,200 samples collected at 2.0 Hz), with one burst every 60 minutes. Additionally, the unit had 42 depth cells (or bins) of 0.50 m depth, starting 1.05 m above the transducer. Current profiles were determined using 50 pings averaged every 15 minutes. Directional wave data were collected every 20 minutes using a maximum cutoff frequency of 0.50 Hz and a minimum included wave period of 2.0 seconds. The height and directional spectrum have 128 frequency bands from zero to 1.0 Hz.

Wave data including wave heights and periods were also collected every 30 minutes using non-directional wave gauges (RBR TWR-2050P) mounted with sensors approximately 0.9m above the bed at D1 and approximately 0.7 m above the bed at D2. The wave gauge at D1 was accurate for depths up to 50 m, while the gauge at D2 was accurate for depths up to 20 m. Both units were configured to collect wave samples at a frequency of 4 Hz and 1024 samples per burst with no averaging. The depth channel on these units is calibrated to an accuracy of 0.05% full scale. To compare the difference in instrument readings, current velocity, temperature, and pressure readings were also reported every 15 minutes. Unfortunately, at the D2 location the lower half of the tripod was buried by sediment and prevented retrieval of the system. While attempting to pull

up the system, the upper half of the tripod (containing the Aquadopp Profiler and YSI 6600) came free while the lower half (containing the RBR wave gauge) was left buried. Therefore, no wave gauge data from D2 were recovered.

Two YSI 6600 multiparameter sondes were used to collect salinity, temperature, pressure, and turbidity measurements every 15 minutes. One YSI 6600 was attached to the Barnacle's exterior with sensors approximately 0.4m above the bed in the D1 system and one YSI 6600 was mounted with sensors approximately 0.6 m above the bed in the D2 system. The YSI 6600 has an optical turbidity sensor with 90-degree scatter and automated mechanical wiping before every reading. The turbidity sensor has an accuracy of ± 2% of the reading or 0.3 NTU (whichever is greater) and a resolution of 0.1 NTU. The salinity is calculated from conductivity and temperature probes: the conductivity probe is a four-electrode cell with auto ranging and the temperature probe is a thermistor. The salinity sensor is accurate up to ± 1.0% of the reading or 0.1 ppt, whichever is greater, and the resolution is 0.01 ppt. Depth readings are taken using a stainless steel strain gauge.

A Nortek Aquadopp Current Profiler was positioned with sensors approximately 1.05 m above the bed on the D2 deployment system. The current profiler used 20 cells of 0.10 m depth, starting 0.10 m beyond the transducer. Current profiles were determined using pings averaged for 60 seconds every 30 minutes. The horizontal velocity range detected with this unit is ±10 m/s with an accuracy of 1% of the measured value ±0.5 cm/s. Directional wave data were determined using 1,024 total wave samples (with a sample taken at 2.0 Hz every two hours), with one burst every 60 minutes. The wave cell size was 0.5 m. The unit was configured for an east, north, up coordinate system with the profiler looking up. A salinity of 28 ppt was assumed during device configuration.

The Fiobuoy acoustic, submersible marine marker buoy was used to ensure that the D1 deployment system was undetectable to passers-by. This unit is designed to release when an acoustic signal is fired under water. Upon recovery of the D1 deployment system, the Fiobuoy line was seen without the marker buoy. It is believed that a trawling vessel caught the Fiobuoy mooring line and drug the deployment system until the rope broke, releasing the buoy. The Barnacle and attached instruments were recovered, but a sudden change in depth, heading, and pitch measurements indicates that the incident happened around 4/16/10 and the measurements taken after that time were omitted.

The continuous data from D1 and D2 were correlated with both meteorological and astronomical forcing from several continuous monitoring stations throughout the basin. Continuous monitoring stations used include National Data Buoy Center (NDBC), National Oceanographic and Atmospheric Association (NOAA), U.S. Army Corps of Engineers (USACE) Rivergages, Louisiana Universities Marine Consortium (LUMCON), NOAA National Ocean Service (NOS), and NOAA Physical Oceanographic Real-Time System (PORTS) stations. These stations are discussed in detail in Chapter 4.

Numerical Modeling

To test Hypotheses 1 and 2, hydrodynamic modeling was conducted using a computational grid or domain that included a portion of the Northern Gulf of Mexico and all major geographic features, including interior wetlands, barrier islands, and tidal channels. This domain covers the entire Breton/Chandeleur Sound, Barataria Basin, and Pontchartrain Estuary, as well as part of the Mississippi Sound. The model was driven by meteorological and tidal forcing during the time of the field deployments. Table 1 summarizes the model simulations and the objective of each simulation. Specifics regarding the model are discussed in Chapter 4. Model results were calibrated and validated using the field data collected at D1 and D2, in addition to other gauging locations throughout the computational domain.

Table 1 - Simulation table describing the simulation name, objective, computational grid details, and analysis methods used.

Simulation Name	Objective	Grid details	Methods
Base-case	Test Hypothesis 1. Will the tidal prism increase if barrier islands are converted to inner shoals?	Original barrier island and interior shoreline grid. (No RSLR or shoaling)	Tidal prism calculations
H1		Barrier islands converted to inner shoals with 10 years of RSLR.	
Base-case	Test Hypothesis 2. Will the tidal prism increase if the bay area increases?	Original barrier island and interior shoreline grid. (No RSLR or shoaling)	Tidal prism calculations
H2		Barrier islands converted to inner shoals. Retreated interior shoreline. 100 years of RSLR.	

For the H1 and H2 scenarios, the grid was altered according to generalized RSLR and subsidence equations. The RSLR equation is applied to subaerial nodes and is as follows:

$$Depth_{final} = Depth_{bc} + (RSLR - accretion)(years) \quad \text{(Eqn. 4)}$$

where $Depth_{final}$ is the depth of the node after RSLR impact, $Depth_{bc}$ is the depth of the node before RSLR impact (or the base-case scenario), $RSLR$ is the relative sea level rise rate, $accretion$ is the accretion rate, and $years$ is the number of years over which the RSLR/ accretion occurs. The subsidence equation is applied to submerged nodes and is as follows:

$$Depth_{final} = Depth_{bc} + (subsidence - sedimentation)(years) \quad \text{(Eqn. 5)}$$

where $Depth_{final}$ is the depth at a node after subsidence, $Depth_{bc}$ is the depth of the node before subsidence (or the base-case scenario), $subsidence$ is the subsidence rate, $sedimentation$ is the sedimentation rate, and $years$ is the number of years over which the subsidence/sedimentation occurs.

To answer key research questions, the tidal exchange through major tidal channels were quantified. Model results were extracted at equidistant points along primary tidal exchange transects and used to compute the instantaneous flow and volume flux across each transect. These fluxes were computed and compared for all scenarios. Small tidal exchange channels had only two points, one at each bounding edge. Transects were chosen so that conclusions could be made about the total flux through an area. For instance, the flow through the ICWW, Chef Menteur, and Rigolets should approximately equal the flow through the Half Moon Island and Bayou La Loutre transects, less any tidal dissipative forces such as friction. Similarly, the flow through the Chandeleur Island and Ship to Hewes Point transects should describe approximately the total flow entering Breton and Chandeleur sounds, less the flow passing through the Mississippi Sound north of Ship Island. Figure 8 shows the location of each transect, while Table 2 describes the transect number, transect name, and number of equidistant computation points.

Table 2 - Transect number, name, and number of equidistant points corresponding with Figure 8.

Transect number	Transect name	Number of points
1	Chef Menteur	2
2	Rigolets	3
3	ICWW	2
4	Bayou La Loutre	4
5	Half Moon Island	14
6	Cat Island	15
7	Ship Island to Hewes Point	15
8	Chandeleur Islands	100

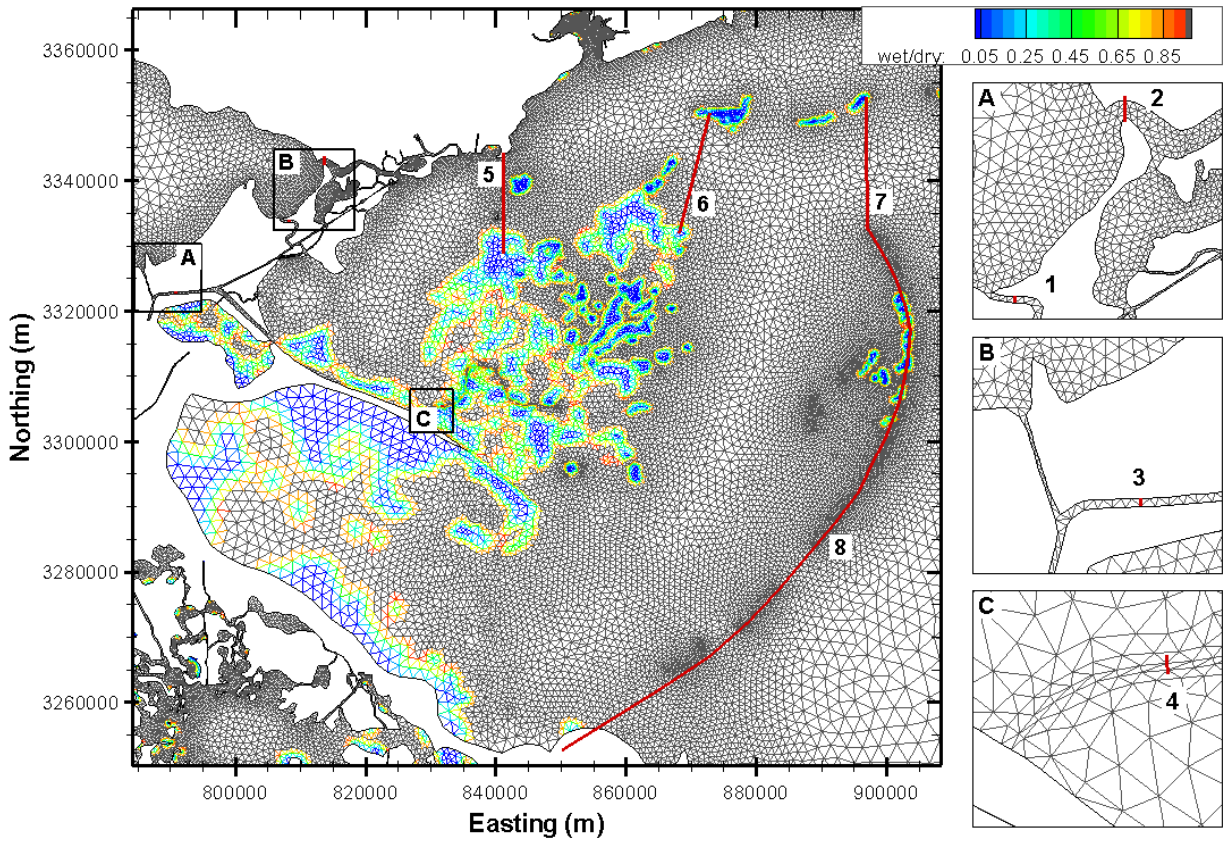

Figure 8 - Map of tidal exchange transects. Contours show the wet/dry parameter for the base-case scenario. (Zero value represents subaerial elements; gray color represents water elements.)

The following formula (Taylor, 1920) is used to find the rate of energy input E_{total} into the system through the tidal inlet width L:

$$E_{total} = E_{kinetic} + E_{potential} \quad \text{(Eqn. 6)}$$

$$E_{kinetic} = \frac{1}{2}\int_0^L (sin\,\theta) \cdot (2g\eta^2 + hS^2 + \eta S^2) dl \quad \text{(Eqn. 7)}$$

$$E_{potential} = \rho g \int_0^L h\eta (S\,sin\,\theta)\, dl \quad \text{(Eqn. 8)}$$

$$E_{ratio} = E_{kinetic}/E_{potential} \quad \text{(Eqn. 9)}$$

where ρ is the water density; g is the acceleration due to gravity; η is the water elevation above mean sea level (sea surface anomaly); S is the absolute current speed (the magnitude of the u_{along} and u_{across} components); h is the water depth below mean sea level; and θ is the angle between an element in the water column and the direction of the current. Figure 9 gives a graphical description of these variables. Eqn. 4, Eqn. 5, and Eqn. 6 were used successfully for computational purposes in Hart and Murray (1978). Eqn. 7 is used to calculate the kinetic to potential energy ratio across a transect.

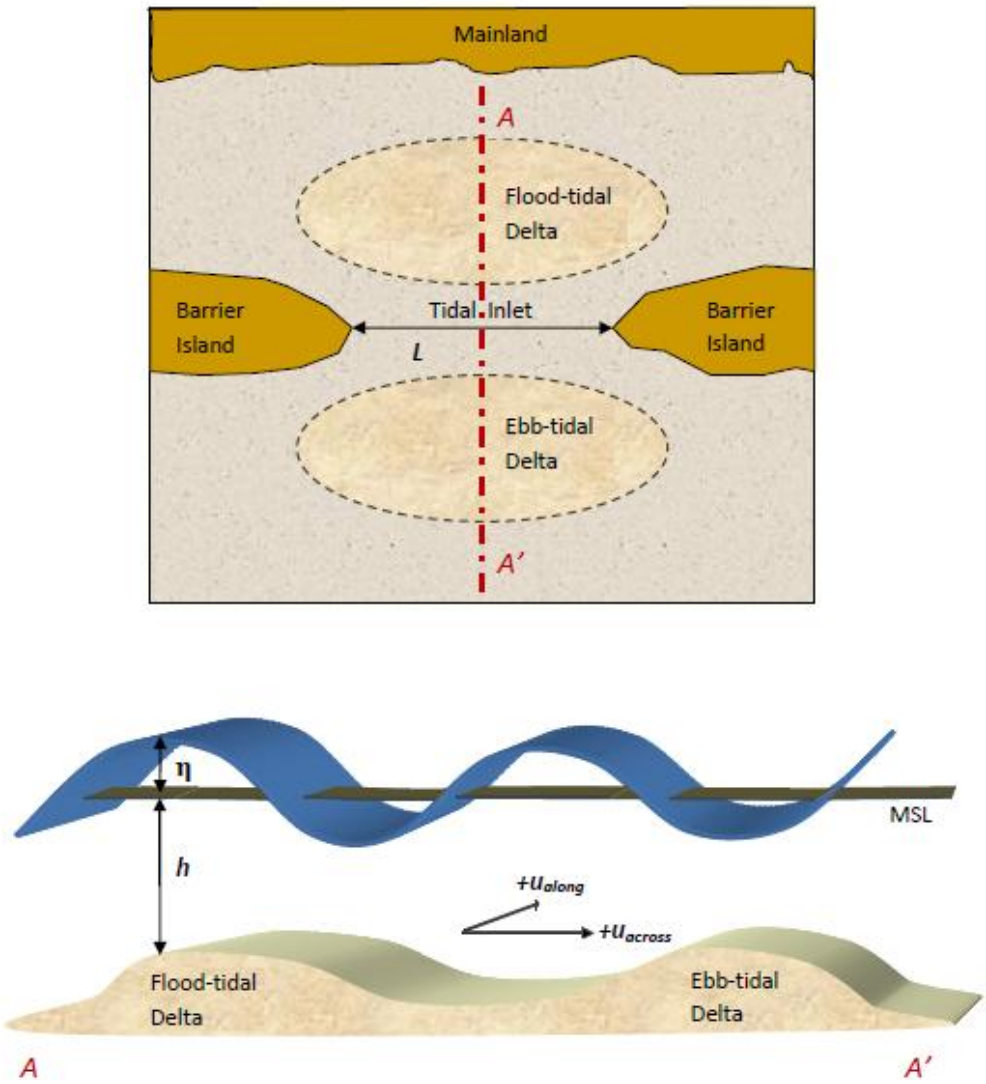

Figure 9 - Schematic diagram of variables used in the definition of the energy equation.

Instantaneous tidal prism calculations were calculated through the equations described in Hart and Murray (1978) and Jarrett (1976). The instantaneous flow crossing each tidal exchange transect was calculated by using the equation:

$$Q_i = \int_0^L (h_i + \eta_i)\left(u_{across,i}\right)dl \qquad \text{(Eqn. 10)}$$

where Q_i is the instantaneous flow rate through the inlet and $u_{cross,i}$ is the depth-averaged velocity perpendicular to the transect orientation. Negative velocities indicate flood currents while positive velocities indicate ebb currents (Figure 9). Subsequently, the tidal volume V passing through the transect can be calculated by integrating Eqn. 7 over the desired time period using:

$$V = \int_t^{t+dt} Q_i \, dt \qquad \text{(Eqn. 11)}$$

CHAPTER 4

Model Description

The Finite-Volume Coastal Ocean Model (FVCOM) was selected for this study because it is a prognostic, unstructured-grid, finite-volume, free surface, three-dimensional primitive equation coastal ocean circulation model developed by Chen, Liu, and Beardsley (2003). The model consists of momentum, continuity, temperature, salinity, and density equations and is closed physically and mathematically using turbulence closure submodels (Burchard, 2002; Mellor and Yamada, 1982). The horizontal grid is composed of unstructured triangular cells, and the irregular bottom is represented using generalized terrain-following coordinates (otherwise known as sigma coordinates). The general ocean turbulent model (GOTM) developed by Burchard (2002) has been added to FVCOM to provide optional vertical turbulent closure schemes. FVCOM is solved numerically by a second-order accurate discrete flux calculation in the integral form of the governing equations over an unstructured triangular grid. This approach combines the best features of finite-element methods (grid flexibility) and finite-difference methods (numerical efficiency and code simplicity) and provides a better numerical representation of both local and global momentum, mass, salt, heat, and tracer conservation. The equations for momentum, continuity, temperature, salinity, and density are as follows:

$$\frac{\partial u}{\partial t} + u\frac{\partial u}{\partial x} + v\frac{\partial u}{\partial y} + w\frac{\partial u}{\partial t} - fv = -\frac{1}{\rho_0}\frac{\partial P}{\partial x} + \frac{\partial}{\partial z}\left(K_m\frac{\partial u}{\partial z}\right) + F_u \qquad \text{(Eqn. 12)}$$

$$\frac{\partial v}{\partial t} + u\frac{\partial v}{\partial x} + v\frac{\partial v}{\partial y} + w\frac{\partial v}{\partial t} + fu = -\frac{1}{\rho_0}\frac{\partial P}{\partial y} + \frac{\partial}{\partial z}\left(K_m\frac{\partial v}{\partial z}\right) + F_v \qquad \text{(Eqn. 13)}$$

$$\frac{\partial P}{\partial z} = -\rho g \qquad \text{(Eqn. 14)}$$

$$\frac{\partial u}{\partial x} + \frac{\partial v}{\partial y} + \frac{\partial w}{\partial z} = 0 \qquad \text{(Eqn. 15)}$$

$$\frac{\partial \theta}{\partial t} + u\frac{\partial \theta}{\partial x} + v\frac{\partial \theta}{\partial y} + w\frac{\partial \theta}{\partial t} = \frac{\partial}{\partial z}\left(K_h\frac{\partial \theta}{\partial z}\right) + F_\theta \qquad \text{(Eqn. 16)}$$

$$\frac{\partial s}{\partial t} + u\frac{\partial s}{\partial x} + v\frac{\partial s}{\partial y} + w\frac{\partial s}{\partial t} = \frac{\partial}{\partial z}\left(K_h\frac{\partial s}{\partial z}\right) + F_s \qquad \text{(Eqn. 17)}$$

$$\rho = \rho(\theta, s) \qquad \text{(Eqn. 18)}$$

where x, y, and z are the east, north, and vertical axes of the Cartesian coordinate system; u, v, and w are the x, y, and z velocity components; θ is the potential temperature; s is the salinity; ρ is the density; P is the pressure; f is the Coriolis parameter; g is the gravitational acceleration; K_m is the vertical eddy viscosity coefficient; and K_h is the thermal vertical eddy diffusion coefficient. Here F_u, F_v, and F_s represent the horizontal momentum, thermal, and salt diffusion terms.

FVCOM uses modified Mellor and Yamada level 2.5 (MY-2.5) and Smagorinsky turbulent closure schemes to simulate vertical and horizontal mixing, respectively (Chen, Liu, and Beardsley, 2003). For a more detailed description of model development and other capabilities, the reader is directed to Chen, Liu, and Beardsley (2003). The model was used in three-dimensional mode because of the episodic and seasonal stratification that the estuary experiences (Abadie and Poirrier, 2000; Georgiou and McCorquodale, 2002; Li *et al.*, 2008) and to capture additional stratification potentially induced near freshwater input sources. As an additional deciding factor,

the freely available source code for FVCOM does not readily offer salinity transport under the two-dimensional mode without code modifications.

Model Implementation

The model computational domain includes the NGOM from Port Fourchon, Louisiana, to Santa Rosa Island, Florida. This domain includes key features such as the Pontchartrain Estuary (including Lakes Maurepas, Pontchartrain, and Borgne as well as the Biloxi Marshes); the Mississippi River Delta; the Barataria Basin; and the Mississippi, Breton, and Chandeleur Sounds. The computational domain consists of 43,768 computational nodes and 79,596 elements (Figure 10 and Figure 11). Figure 12 and Figure 13 show the areas of primary interest in this study, the northwestern and southeastern areas of the grid, in more detail. Additional detailed maps of the model domain can be found in Appendix A. The horizontal grid resolution varies spatially from 80 m in navigation channels and tidal passes to more than 10 km near the open boundary. The vertical resolution of the model includes eleven vertical sigma layers equally distributed over the water column. To prevent the use of a very small time step and afford reasonable simulation times, the maximum bathymetric depth was limited to 200 m. This change affects about 2% of the model domain.

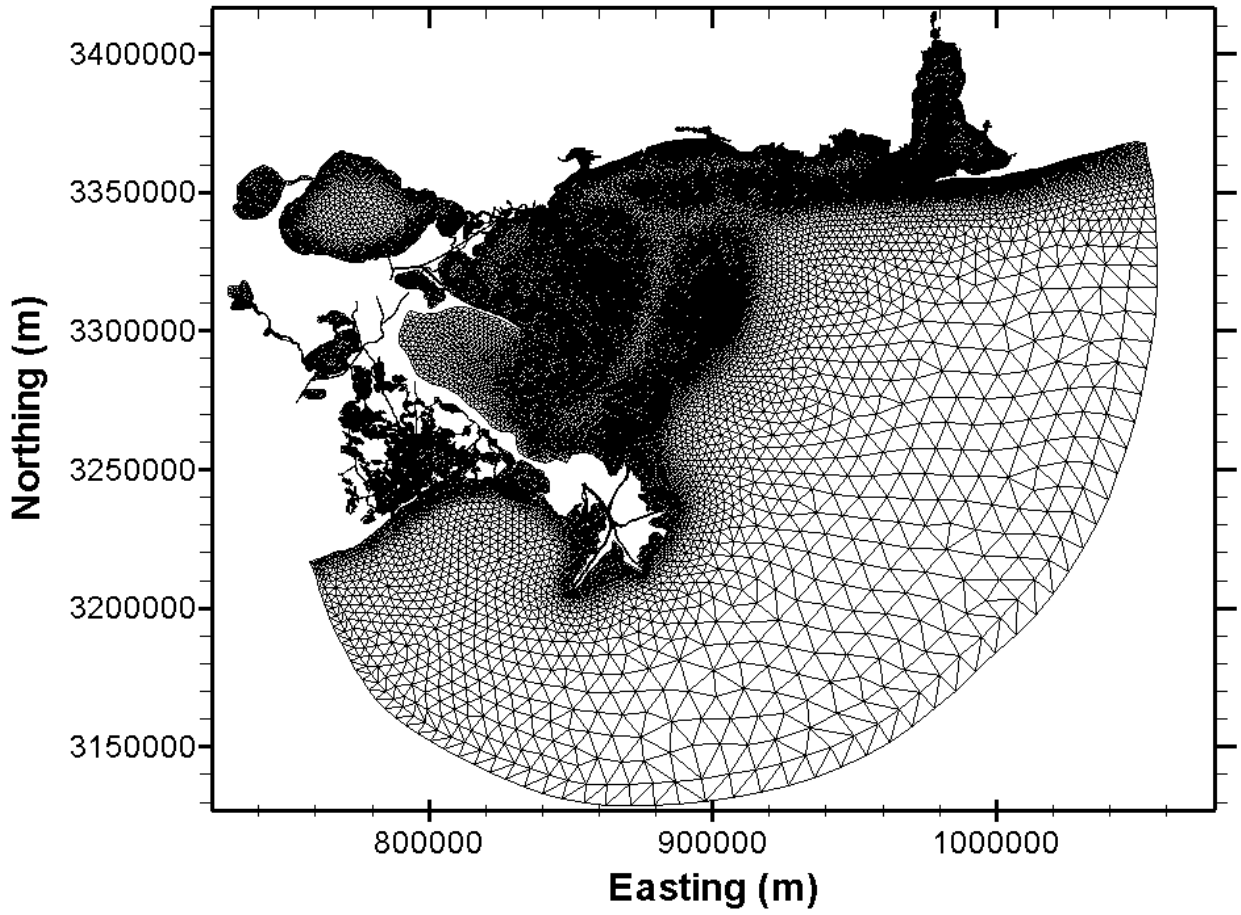

Figure 10 -Entire computational grid domain mesh from southeast Louisiana to the Florida/Alabama state line (coordinates in UTM 15, meters).

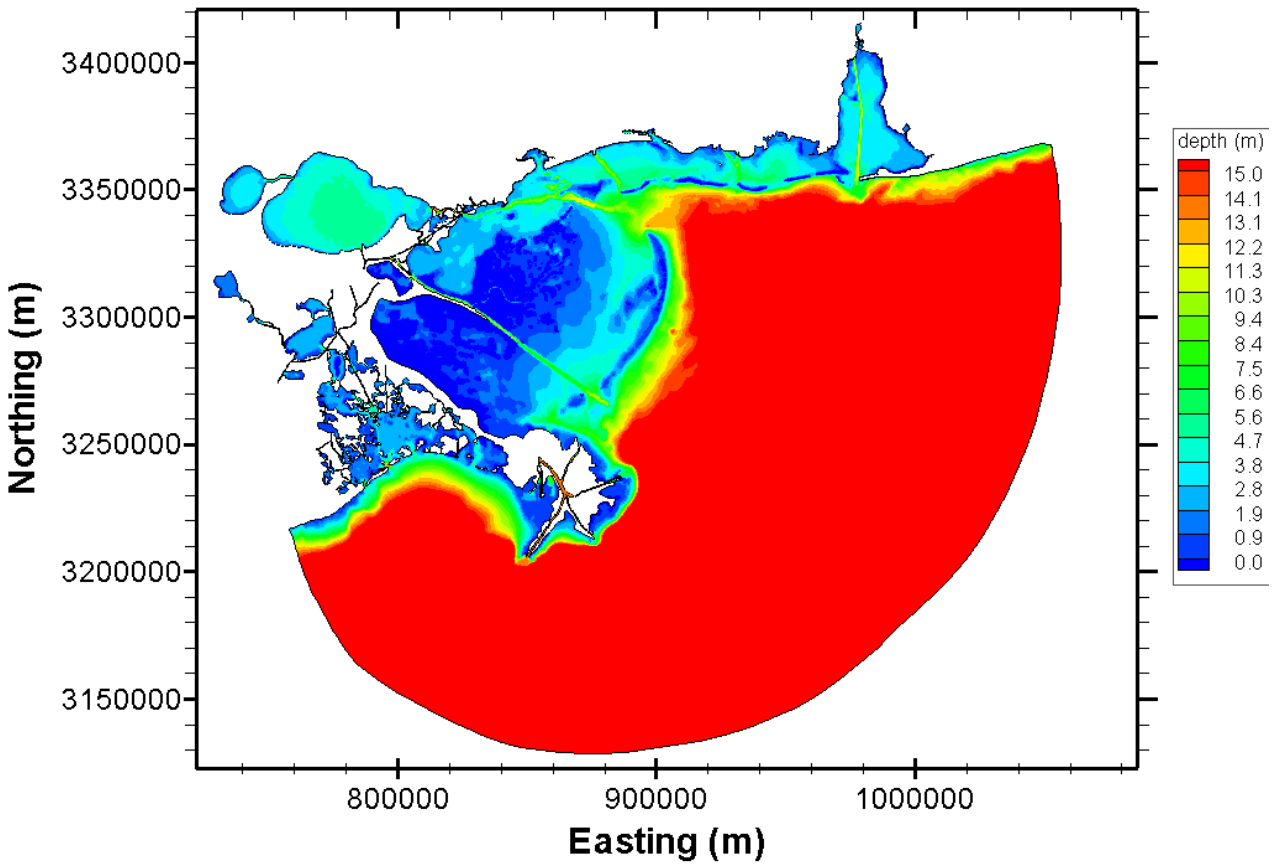

Figure 11 - Entire computational grid domain from southeast Louisiana to the Florida/Alabama state line (coordinates in UTM 15, meters). Bathymetric contours are shown with depth in meters.

The FVCOM grid was created using the grid-generation module developed for the finite-element Surface-water Modeling System (SMS) program. Coastline and bathymetry files were imported into SMS to create the grid. For this study, grids from previous projects were combined to form the domain boundaries. These projects were the Barataria diversion study (Georgiou *et al.*, 2010) and the Pontchartrain Estuary diversion study (Georgiou *et al.*, 2009). The Barataria grid was used as a guide for the domain west of the Mississippi River including the interior of the Barataria Basin. The shoreline was created using a combination of satellite imagery and DOQQ images. Both datasets obtained were from post-Katrina images; the Landsat Thematic Mapper 5 satellite image was acquired on October 9, 2005, while the DOQQ images were captured October-November 2005. Based on the initial investigation using satellite imagery, a vector shoreline was digitized from the 2005 DOQQ's map of the Basin using ESRI ArcMap™. The high-resolution (sub-100 meter) Barataria shoreline file was imported to SMS 9.2. The Barataria project used an ADCIRC grid SL15v06r09 composite LIDAR/bathymetry dataset. Because of quality issues with the bathymetric coverage in the region, LIDAR data above MSL (~0.08m NAVD88) was retained, while bathymetry was replaced with survey and transect data. All bathymetry was converted into a common horizontal and vertical datum (UTM zone 15, meters and NAVD 88, meters) and interpolated onto the mesh.

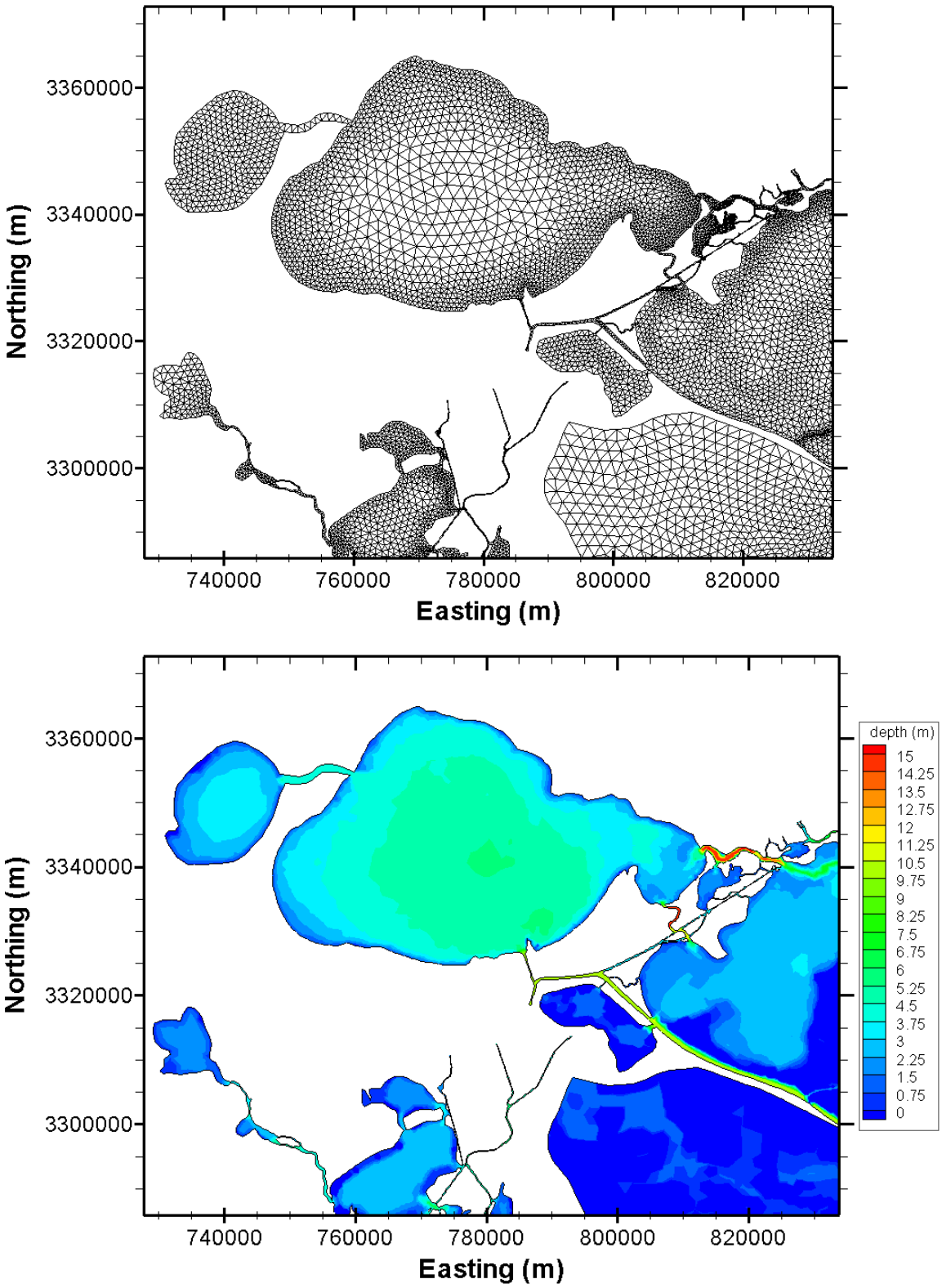

Figure 12 - Northwestern area of domain including Lakes Pontchartrain, Maurepas, and Borgne as well as connecting channels such as the IHNC, Rigolets, MRGO, and ICWW: (Top) Domain mesh and (Bottom) Base-case bathymetric contours with depth shown in meters.

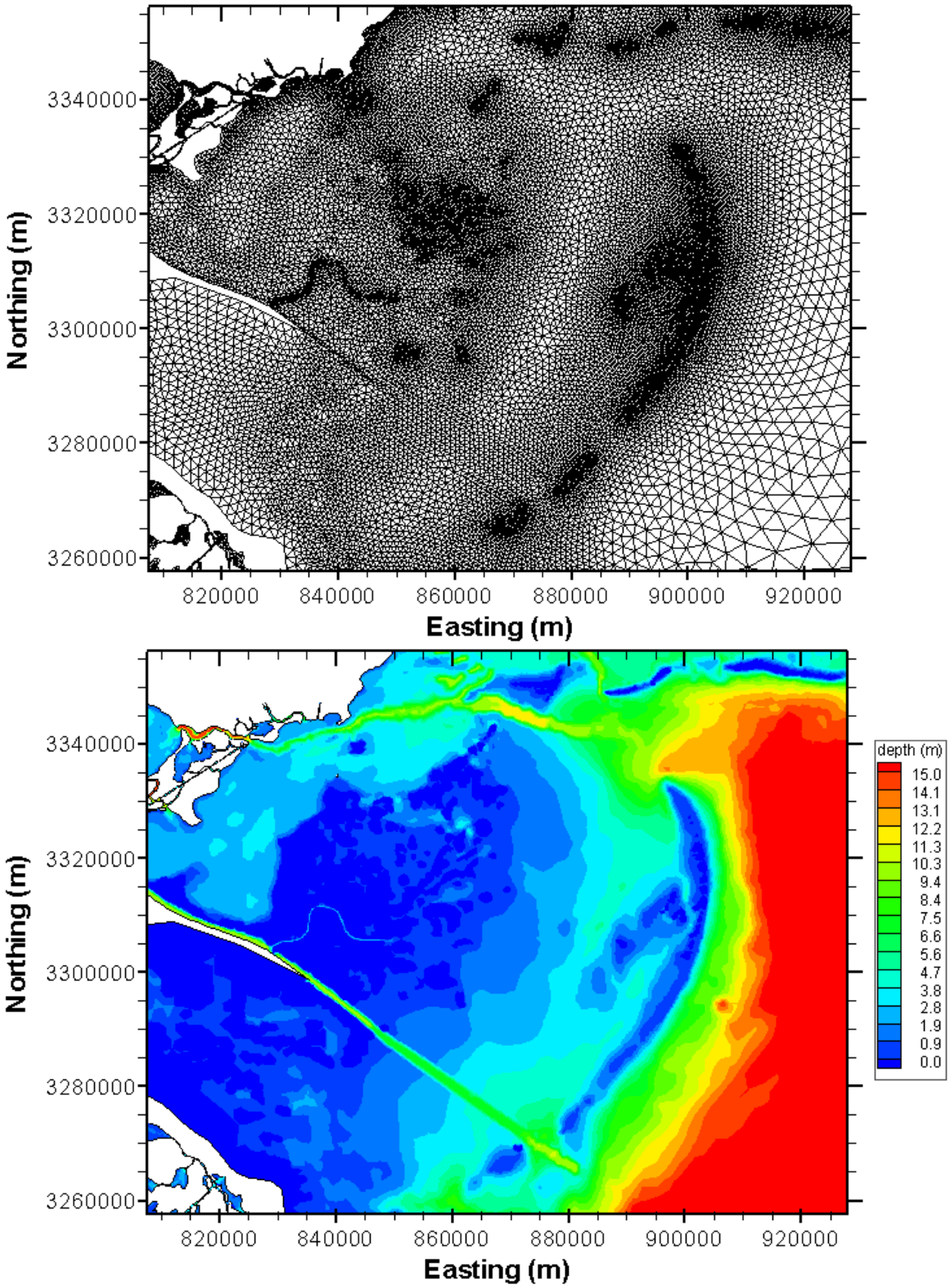

Figure 13 - Southeastern area of domain including the Biloxi Marsh, Chandeleur Islands and Sound, Mississippi barrier islands and Sound, MRGO, and Lake Borgne: (Top) Domain mesh and (Bottom) Base-case bathymetric contours with depth shown in meters.

The grid from the Pontchartrain Estuary diversion study was used for the domain east of the Mississippi River. The model bathymetry was obtained from a combination of sources: National Oceanic and Atmospheric Administration (NOAA), National Ocean Service (NOS) hydrographic surveys, and supplements from hydrographic surveys conducted by the U.S. Geological Survey (USGS) in 1996. Additional data in Breton and Chandeleur sounds were obtained from historic NOAA hydrographic surveys (Georgiou *et al.*, 2009).

The comparison of the base-case and H1 simulations test Hypothesis 1 and thereby answer the question: Will the tidal prism increase if barrier islands are converted to inner shoals? The base-case has a grid domain with barrier islands, marshes, and interior shorelines similar to present-day conditions (Figure 14). Therefore, this grid features a transgressive depositional system in Stage 2 of the Penland Model. H1 is intended to represent the system in Stage 3 of the Penland Model, when barrier islands have converted to inner shoals and eroded due to increased storminess (Figure 15). In this scenario, however, the interior, deltaic marsh has been able to accrete at the same rate as RSLR. The barrier islands have received the brunt of the storm energy and waves, thereby leaving the marsh relatively unscathed. Bathymetric alterations were achieved using a FORTRAN code to adjust the depth of the Mississippi barrier islands' and Chandeleur Islands' subaerial nodes (hereby referred to as "barrier island nodes") within the geographic bounds of 730,400 m to 868,925 m easting and 3,203,070 m to 3,366,670 m northing. Barrier island nodes with a negative depth were adjusted by 0.6m to represent barrier island loss due to a major storm. The equation used follows:

$$Depth_{H1,bi} = Depth_{bc,bi} + 0.6m \quad \text{(Eqn. 19)}$$

where $Depth_{H1,bi}$ is the depth of the barrier island node in the H1 scenario and $Depth_{bc,bi}$ is the depth of the barrier island node in the base-case scenario.

In the H1 scenario, subaerial marsh nodes within the geographic bounds of 869,820 m to 1,004,340 m easting and 3,258,970 m to 3,371,300 m northing were adjusted by a RSLR rate of 0.6 cm/yr less an accretion rate of 0.1 cm/yr over ten years. The equation used follows:

$$Depth_{H1,marsh} = Depth_{bc,marsh} + \left(\frac{0.006m}{yr} - \frac{0.001m}{yr}\right)(10\ yr) \quad \text{(Eqn. 20)}$$

where $Depth_{H1,marsh}$ is the depth of the marsh node in the H1 scenario and $Depth_{bc,marsh}$ is the depth of the marsh node in the base-case scenario.

All other nodes (namely, submerged nodes) were adjusted by a RSLR rate of 0.57 cm/yr less a sedimentation rate of 0.11 cm/yr over ten years. The equation used follows:

$$Depth_{H1,submerged} = Depth_{bc,submerged} + \left(\frac{0.0057m}{yr} - \frac{0.0011m}{yr}\right)(10\ yr) \quad \text{(Eqn. 21)}$$

where $Depth_{H1,submerged}$ is the depth of the submerged node in the H1 scenario and $Depth_{bc,submerged}$ is the depth of the submerged node in the base-case scenario.

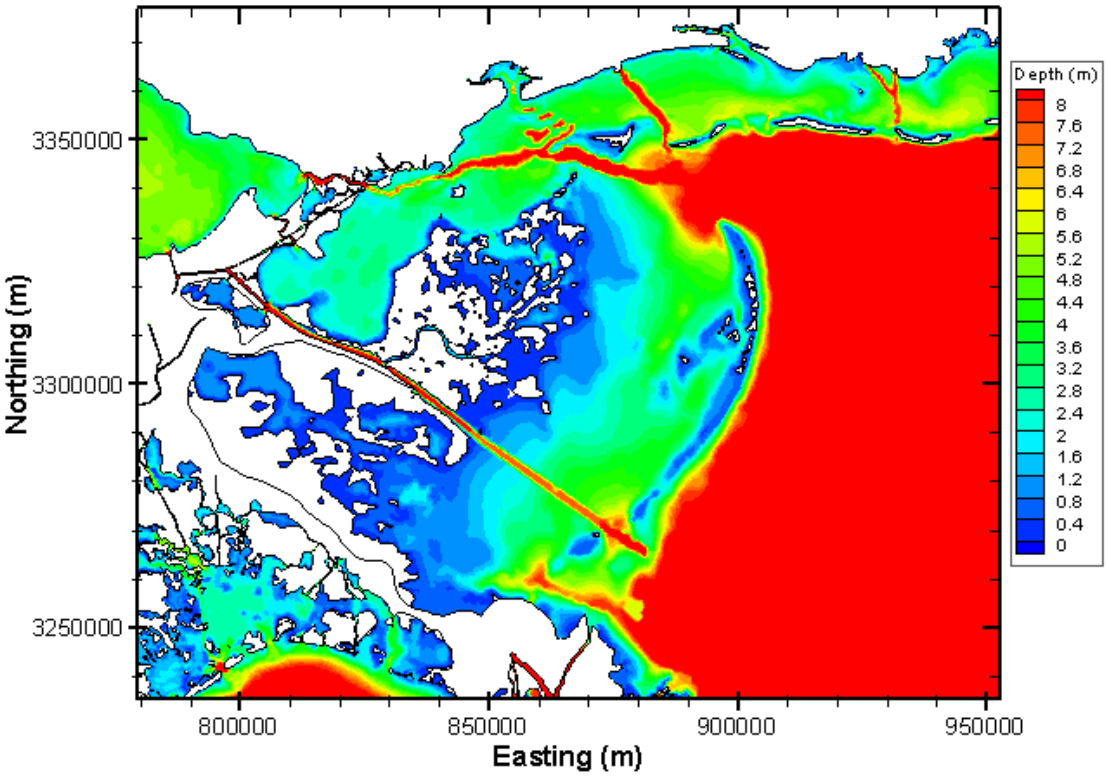

Figure 14 - Base-case contour plot of water depth in meters.

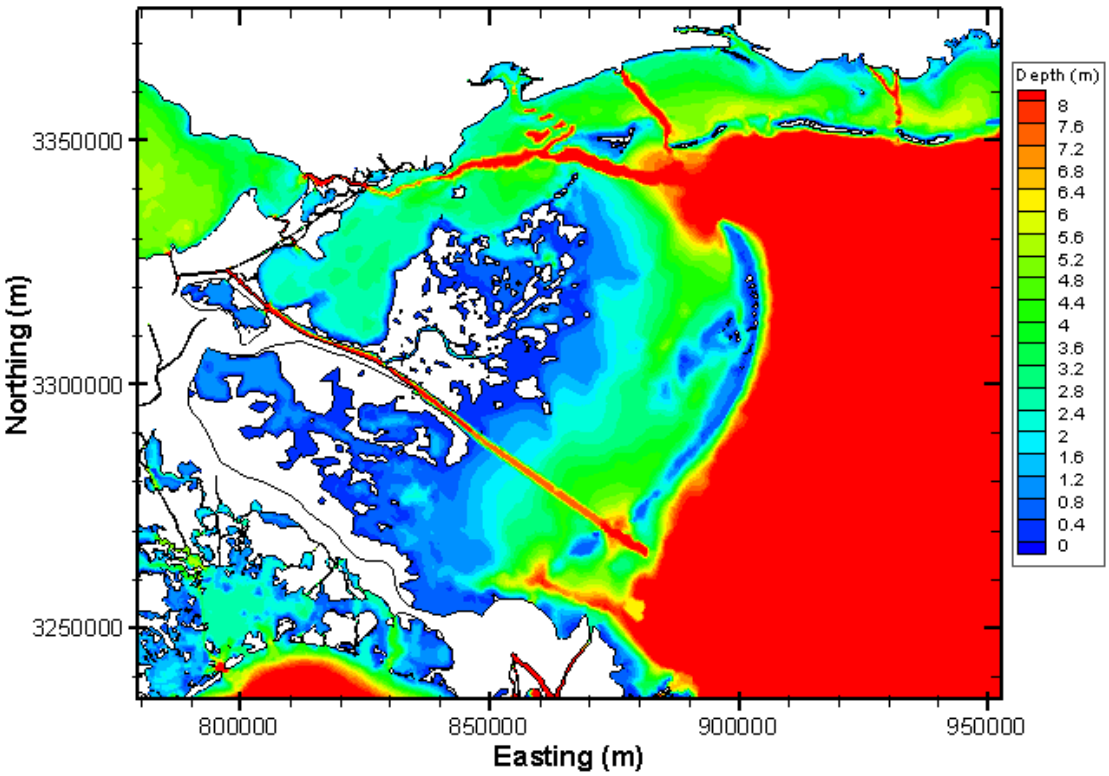

Figure 15 – H1 contour plot of water depth in meters.

The comparison of the base-case and H2 simulations test Hypothesis 2 and thereby answer the question: Will the tidal prism increase if the bay area increases? H2 represents the system in Stage 3 of the Penland Model, when barrier islands have converted to inner shoals. This scenario reflects a system in which the barrier islands and interior deltaic marsh have been submerged and eroded due to increased RSLR (Figure 16). Unlike H2, the marsh in H2 was unable to accrete at a rate comparable to SLR. Bathymetric adjustments were achieved by using a FORTRAN code to adjust the depth of the marsh nodes and barrier island nodes within the geographic bounds of 869,820 m to 1,004,340 m easting and 3,258,970 m to 3,371,300 m northing. All nodes with a negative depth (subaerial nodes) were adjusted by the estimated RSLR rate of 0.6 cm/yr less an accretion rate of 0.1 cm/yr over 100 years. The equation used follows:

$$Depth_{H2,subaerial} = Depth_{bc,subaerial} + \left(\frac{0.006m}{yr} - \frac{0.001m}{yr}\right)(100\ yr) \qquad \text{(Eqn. 22)}$$

where $Depth_{H2,subaerial}$ is the depth of the subaerial node (either marsh or barrier island) in the H2 scenario and $Depth_{bc,subaerial}$ is the depth of the subaerial node in the base-case scenario.

All other nodes (namely submerged nodes) were adjusted by a RSLR rate of 0.57 cm/yr less a sedimentation rate of 0.11 cm/yr over 100 years. The equation used follows:

$$Depth_{H2,submerged} = Depth_{bc,submerged} + \left(\frac{0.0057m}{yr} - \frac{0.0011m}{yr}\right)(100\ yr) \qquad \text{(Eqn. 23)}$$

where $Depth_{H2,submerged}$ is the depth of the submerged node in the H2 scenario and $Depth_{bc,submerged}$ is the depth of the submerged node in the base-case scenario. There is no change in barrier island nodes between H1 and H2, therefore any difference in results between these scenarios is due to changes in elevation of the surrounding sea floor and marsh nodes.

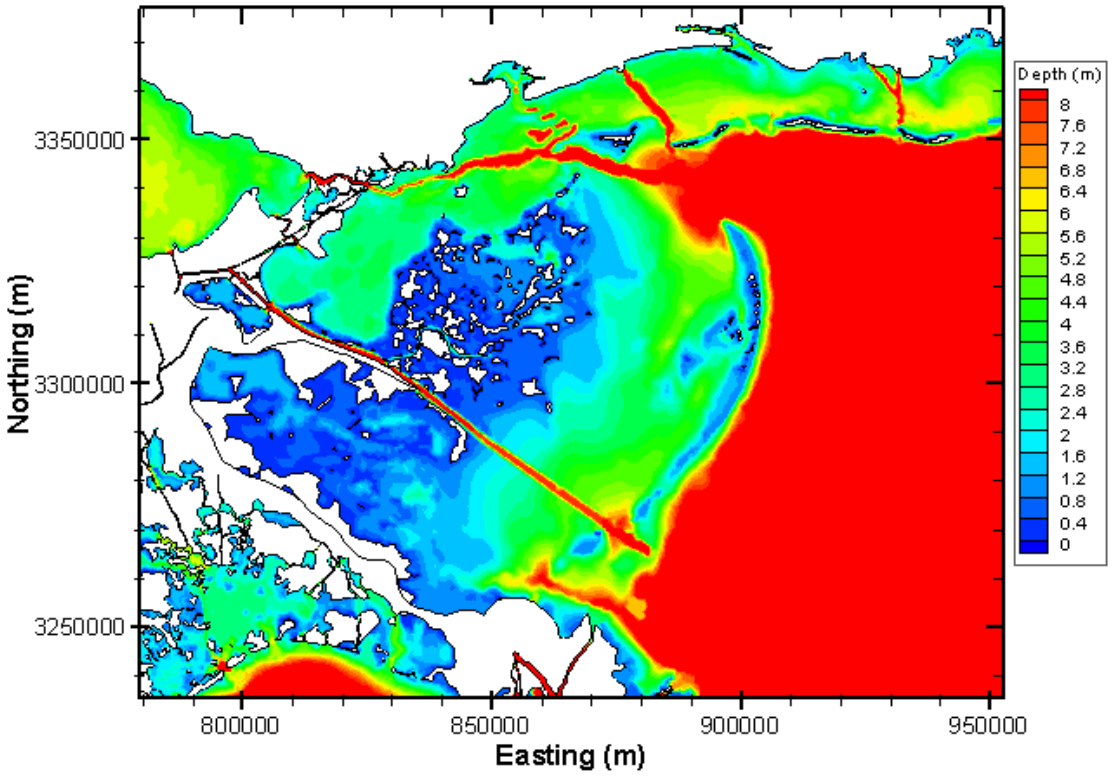

Figure 16 – H2 contour plot of water depth in meters.

Initial Conditions

Datasets collected from various sources (Georgiou, 2002; Haralampides, 2000) were used to generate average salinity conditions for a normal year. These datasets were used to spatially interpolate initial salinity values across the model computational grid while maintaining the natural estuarine gradient (Figure 6). For all simulations, the initial water elevation was set to zero (relative to mean sea level). The model subsequently started each simulation from rest (still water surface), and the spin-up times for all boundary conditions (tributary flows and tidal elevations at open boundaries) were of the order of one day.

Boundary Conditions

Tidal elevations were interpolated along the open boundary using NOAA Station data from Pensacola, Florida and Pilots Station East, SW Pass, Louisiana. After studying calibration results (discussed in more detail in the next section), the elevation data at SW Pass were increased by 25% to provide more accurate tidal amplitudes across the western half of the domain due to the absence of a tidal gauge close to the western boundary. Salinity values at all open boundary nodes were kept constant in time and space at 32 ppt. The temperature values were kept constant at 25 degrees Celsius throughout the domain, including along the open boundary. The open boundary was assumed to be fully mixed (i.e., no stratification was applied) and was constant in time. All simulations used the same boundary conditions.

A sponge layer along the open boundary was used to suppress wave energy reflected back into the computational domain along the open boundary (Chen, Liu, and Beardsley, 2003). The use of a sponge layer is necessary in this domain because of the high depths along the open boundary. For this study, a maximum depth of 200m was used in deeper Gulf of Mexico nodes (Chen, Liu, and Beardsley, 2003). Simulations varied from not using a sponge layer to using a sponge layer with friction coefficients from 0.01 to 0.005. It was decided that the friction coefficient of 0.005 produced the most stable model results. Interior numerical solutions are not affected by the sponge layer; therefore, this friction coefficient has no effect on model accuracy (Chen, Cowles, and Beardsley, 2004). The friction coefficient was kept constant for all nodes and between all simulations. Without a sponge layer in this environment, high gravity waves will reflect off the open boundary and cause unreasonable water elevations along the interior domain. The radius of influence of this sponge layer was 1,525 m at node 1 (near Pensacola, FL) and node 81 (near the Caminada Headland). This radius of influence increased linearly to 22,000 m at the central node (node 40) where the deepest water (200 m) is present and could have the highest influence.

Daily tributary discharges obtained from the USGS were used for all major rivers flowing into the NGOM including the Amite and Tickfaw Rivers in Lake Maurepas, the Tangipahoa and Tchefuncte rivers in Lake Pontchartrain, the Pearl River near the Louisiana and Mississippi state line, the Tensaw and Mobile Rivers in Mobile Bay, the Pascagoula and Biloxi Rivers in Mississippi, and the Wolf and Jourdan rivers in Bay St. Louis (Figure 1). Additionally, the model included discharges at the Caernarvon Outfall Channel at Caernarvon, Louisiana; Davis Pond Freshwater Diversion near Boutte, Louisiana; and the Mississippi River at Belle Chasse, Louisiana. Discharge data used coincided with model simulation periods. For the Mississippi River, a discharge balance was conducted to find the percent of flow from the Mississippi River at Belle Chasse into each river reach (Grand Tiger Pass, West Bay, and Baptiste Collette). It was decided that Grand Tiger Pass, West Bay, and Baptiste Collette would receive 10%, 6.2%, and 11% of Mississippi River at Belle Chasse flow, respectively.

Model Calibration and Validation

Calibration

Eleven stations with tides and/or salinity data were chosen for calibration, including stations in the upper Pontchartrain Estuary, tidal and navigation channels, and open water stations (Figure 17). These stations are operated by NOAA, USGS, NOAA PORTS, LUMCON, and USACE Rivergages. The D1 and D2 field data from this study were also used for model calibration. Table 3 lists the names of stations used, their identification numbers as designated by the operating agency, and the name of the operating agency. This table also specifies whether each station was used to calibrate tides (i.e., tidal amplitude and phase) or both tides and salinity.

The model was calibrated to reproduce observed tidal amplitude and phase variations at selected locations in the NGOM domain. The goal of this study was not to predict exact tidal elevations but to predict amplitude fluctuations and changes in tidal exchange. For example, this study was not designed to determine the exact tidal elevation 100 years from now, but rather what the change in tidal exchange would be after 100 years of RSLR. Therefore, station tidal elevations and model tidal elevations were not referenced to the same vertical datum. To account for these datum discrepancies, a suitable adjustment of tidal magnitude was applied to align the base-case model results with station observations. The adjustment applied varied with each station but was kept constant for all scenarios.

Salinity was also calibrated within the region, but to a less significant degree. The use of interpolated average annual values for initial salinity conditions instead of observed data for the simulated time period made it difficult to replicate observed salinities in the model. A lack of stations with salinity data during the period of interest prevented a more accurate initial salinity interpolation from being used in this project. Therefore, calibration efforts for salinity concentrated on reproducing reasonable salinity trends over the entire domain. For salinity calibration, adjustments of salinity magnitude were applied to observed station data to account for differences in sensor height. For instance, at D1, the salinity sensor was 0.4 m above the bottom of the bed, thereby representing bottom salinity. However, surface salinity results from the model were used for calibration. The adjustment applied accounts for the salinity gradient through the water column.

The calibration simulations were driven with meteorological and tide conditions from 3/31/10 to 4/22/10. During the calibration/validation process, efforts concentrated on calibrating the previously mentioned stations (shown in Figure 17) during the period of 4/16/10 to 4/22/10. This period was chosen for its relatively low winds and barometric pressure (Figure 18). By choosing a period with limited meteorological influences, the model's tidal calibration was conducted with more accuracy and confidence. It has been documented that the estuarine response to wind produces stronger circulation currents and setup than those produced by tidal motion (Georgiou and McCorquodale, 2002; Haralampides, 2000; Signell and List, 1997). Additionally, the passing of a seasonal front is accompanied by a high or low-pressure system that causes changes in barometric pressure. This change in atmospheric pressure greatly influences the water level in the vicinity of the front.

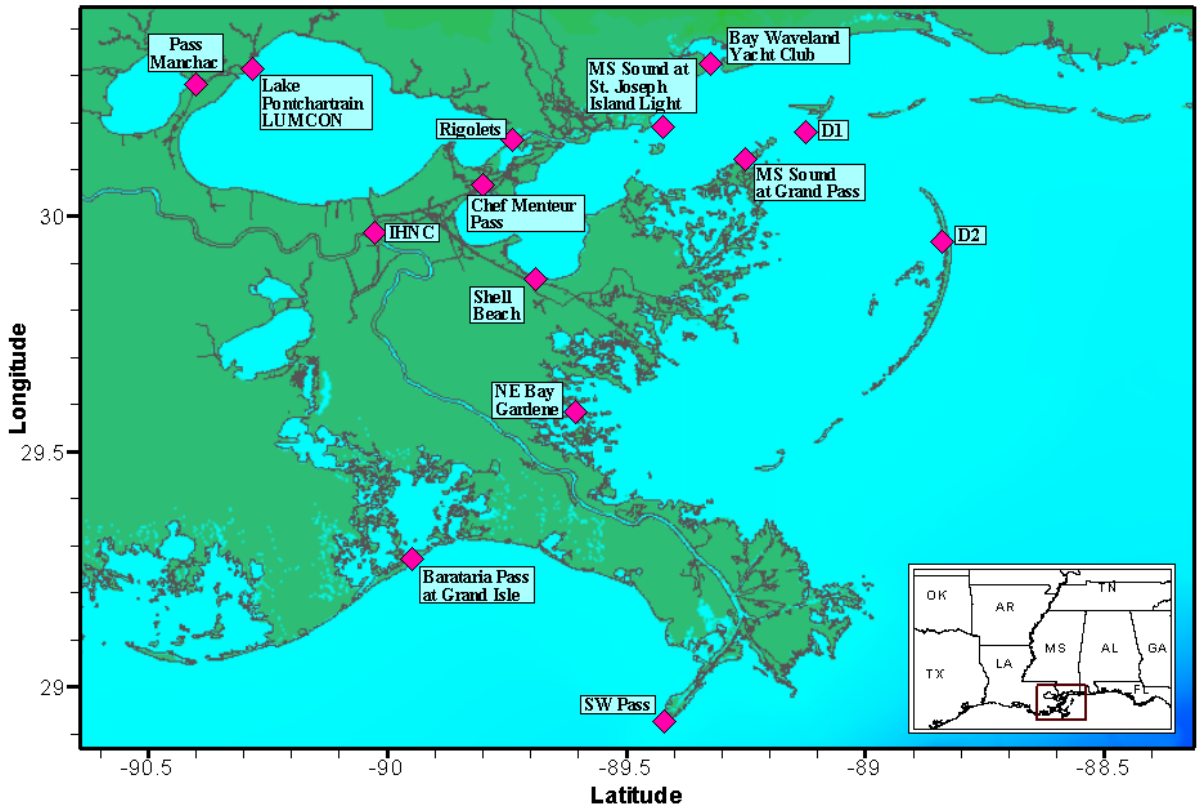

Figure 17 - The inset shows a map of the states surrounding the northern Gulf of Mexico, while the red box outlines the area shown in the large image. The large image is a map of the calibration stations within the domain. Table 3 describes these stations in more detail.

Table 3 - Stations used for model calibration. Station name, number, and operating agency, as well as calibration parameter are provided. Station numbers are in parentheses after station name.

Station	Agency	Calibration Type
Lake Pontchartrain LUMCON (103)	LUMCON	Tides, Salinity
IHNC (76160)	USACE Rivergages	Tides
Pass Manchac near Ponchatoula (85420)	USACE Rivergages	Tides
MS Sound at Grand Pass (300722089150100)	USGS	Tides, Salinity
Shell Beach (8761305)	NOAA	Tides
NE Bay Gardene near Point à la Hache (07374527)	USGS	Tides, Salinity
Rigolets near Lake Pontchartrain (85700)	USACE Rivergages	Tides, Salinity
Chef Menteur Pass near Lake Borgne (85750)	USACE Rivergages	Tides
Barataria Pass at Grand Isle (073802516)	USGS	Tides
Pilots Station East, SW Pass (8760922)	NOAA	Tides
Bay Waveland Yacht Club (8747437)	NOAA	Tides
MS Sound at St Joseph Island Light (301104089253400)	USGS	Tides, Salinity
D1	UNO	Tides, Salinity
D2	UNO	Tides, Salinity

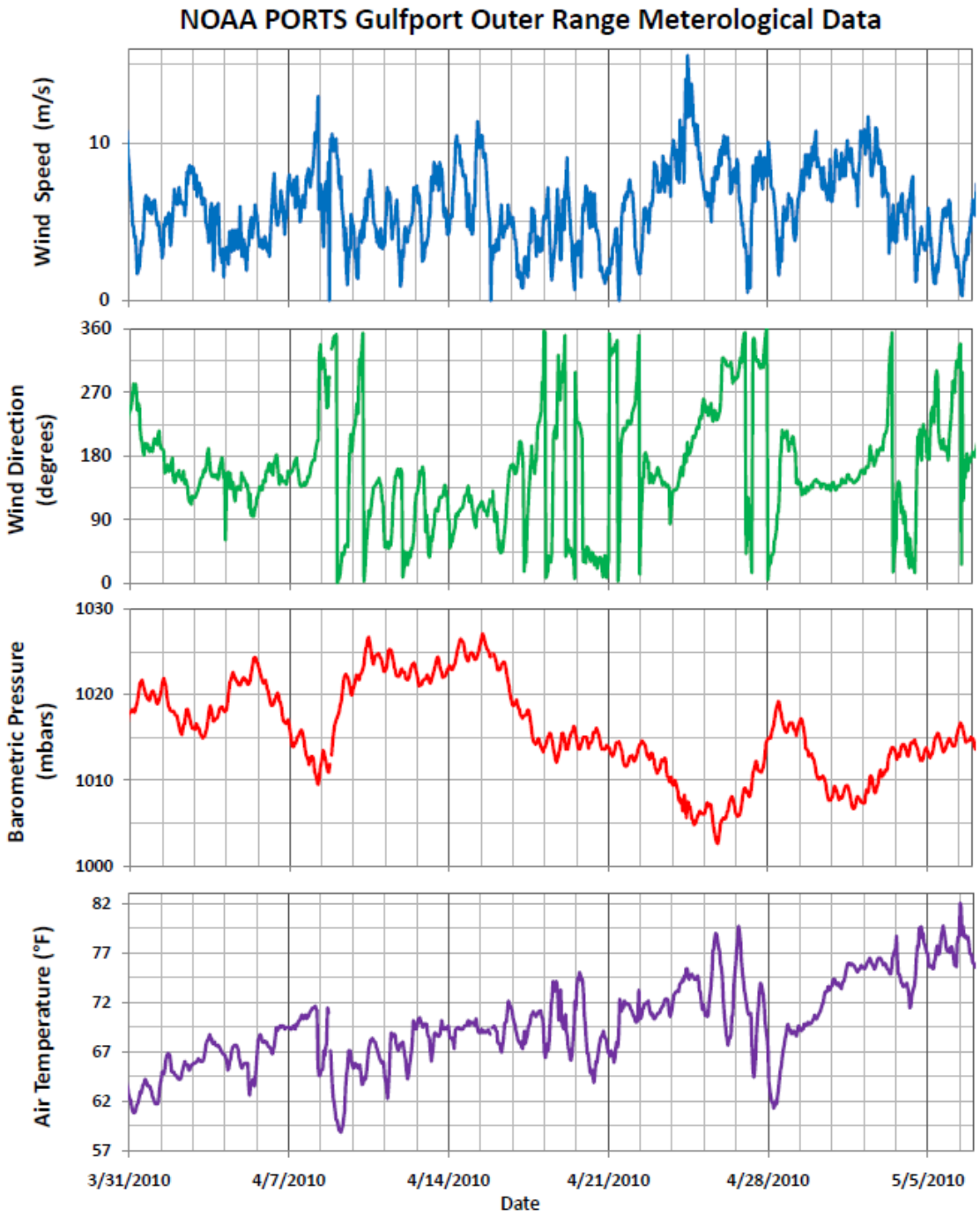

Figure 18 - Meteorological conditions at the NOAA NOS Gulfport Outer Range station (Station GPOM6 – 8744707) for the period of 3/31/10 to 5/7/10.

In the first simulations, tidal amplitudes deviated from observed amplitudes as the station location neared the western boundary. This was because tides at the westernmost node (node 81) were propagated by tides at the SW Pass station (more than 92.8 km east of node 81). As previously mentioned, the SW Pass tidal elevations at node 81 were increased by 25% to correct this problem, and initial tidal conditions along the open boundary were linearly interpolated to vary the tide from the easternmost (Pensacola tides) to westernmost node (SW Pass magnified by

25%). Additionally, bottom roughness heights (z_{0b}) were adjusted during the calibration phase to correct inland tidal propagation and attenuation. For instance, when tidal amplitudes were represented accurately at Grand Pass but under-represented at Pass Manchac, the bottom roughness height was reduced. By reducing the bottom roughness, tidal amplitudes were less dampened. Simulations were conducted with bottom roughness heights of 0.0013 m, 0.0011 m, and 0.0009 m; a bottom roughness height of 0.0009m produced the most accurate results.

Validation

The following tidal validation plots provide a graphical comparison between the base-case scenario and the observed station tides. Graphs for stations not shown in this section can be found in Appendix B.

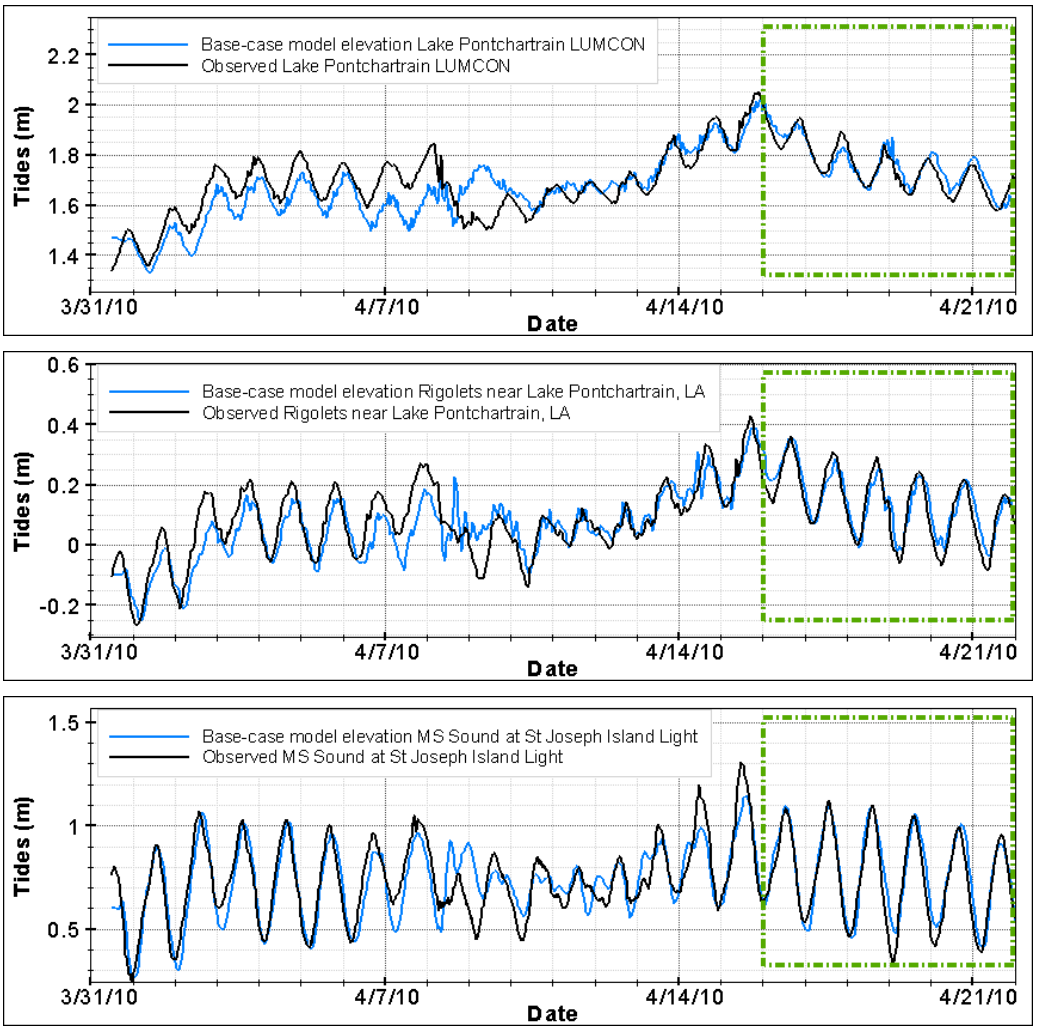

Figure 19 – Comparison of base-case scenario tides (meters) and observed tide data for the calibration period (3/31/10 to 4/22/10). Calibration efforts focused on good correlation during the period of 4/16/10 to 4/22/10 (inside the green box) at the following locations (from top to bottom): Lake Pontchartrain at LUMCON, Rigolets near Lake Pontchartrain, and Mississippi Sound at St. Joseph Island Light. An adjustment was applied to observed data to account for vertical datum differences.

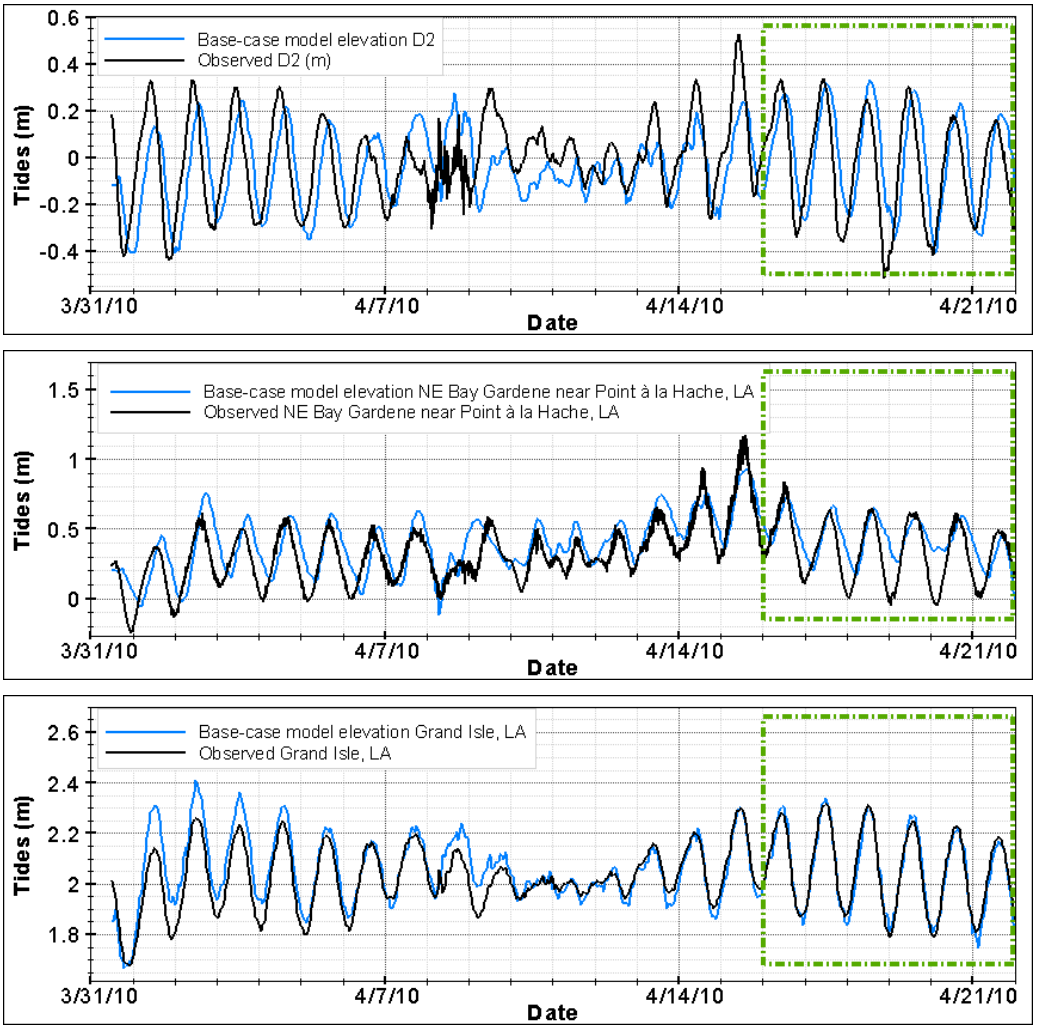

Figure 20 - Comparison of base-case scenario tides (meters) and observed tide data for the calibration period (3/31/10 to 4/22/10). Calibration efforts focused on good correlation during the period of 4/16/10 to 4/22/10 (inside the green box) at the locations (from top to bottom): D2, NE Bay Gardene near Point à la Hache and Barataria Pass at Grand Isle. An adjustment was applied to observed data to account for vertical datum differences.

Figure 19 and Figure 20 show that the model replicated the tidal amplitude within a maximum range of approximately 13 cm (reinforced by the results shown in Table 4). Results were generally in-phase, with the largest phase deviations at shallow nodes (such as NE Bay Gardene and D2). Accurate bathymetry in these areas was unavailable at the time of grid generation, and it is believed that local discrepancies in bathymetry are the cause of the larger phase and amplitude disparity at these sites. The Lake Pontchartrain stations replicated phase well, but underestimated amplitude during the beginning of the period. The good phase correlation indicates that the problem is not due to tidal attenuation near the interior domain (a common problem in a domain as large as this, but resolved during the calibration phase). It is believed that these differences in amplitude result from corresponding changes in barometric pressure. FVCOM does not account for changes in atmospheric pressure, and therefore produces tidal elevations resulting from wind and astronomical tides only. The aforementioned stations do replicate tidal signatures during normal periods well (a difference of less than 10 cm), however all stations poorly simulate the tidal conditions (both phase and amplitude) around the dates of 4/8/10 to 4/9/10. A cold front passed

through the area during this time, producing strong northerly winds and drastic changes in barometric pressures (See Figure 18).

Validation of salinity data was performed using the same graphical and mathematical procedures. The following salinity validation plots (Figure 21) provide a graphical comparison between the base-case scenario results and the observed station salinities. Salinity plots for the calibration stations not shown here can be found in Appendix B. The model replicates phase and changes in amplitude well, but the magnitude of the amplitude is not being simulated well in the model. Again, these discrepancies could be due to bathymetric inconsistencies or sensor height differences. The model does simulate the transport of salinity well, and overall trends (tidal influence on phase and change in amplitude) should be used from the model data, not salinity magnitudes.

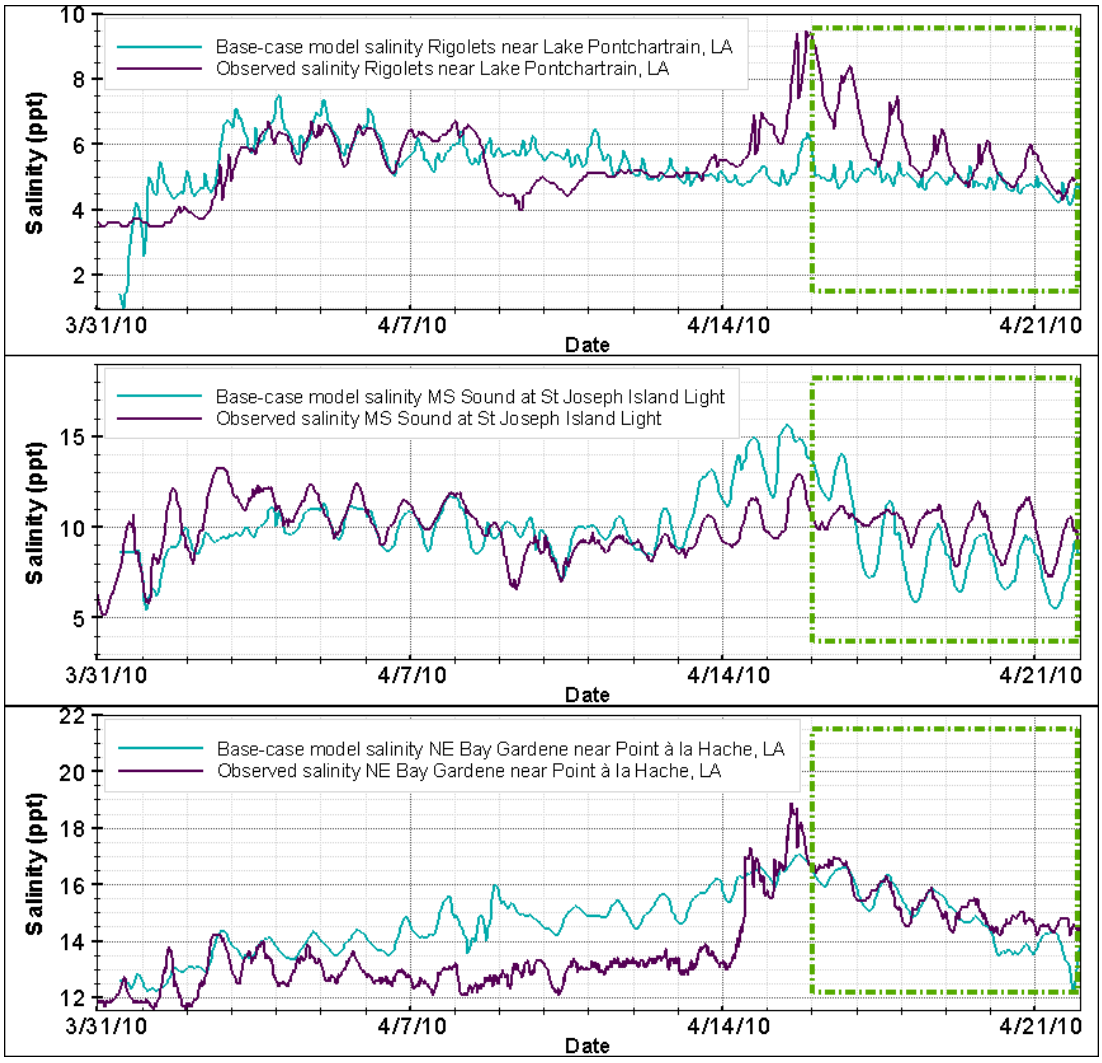

Figure 21 - Comparison of base-case scenario salinities (ppt) and observed salinity data for the calibration period (3/31/10 to 4/22/10). Calibration efforts focused on good correlation during the period of 4/16/10 to 4/22/10 (inside the green box) at the locations (from top to bottom) Rigolets near Lake Pontchartrain, Mississippi Sound at St. Joseph Light, and NE Bay Gardene near Point à la Hache. An adjustment was applied to observed data to account for sensor height differences.

For a numerical comparison of these signals, mean absolute error (MAE) and root-mean-square error (RMSE) were computed (Jin, Hamrick, and Tisdale, 2000). The MAE was calculated with the equation:

$$\text{MAE} = \frac{\sum_{i=1}^{n}|X_{obs} - X_{sim}|}{n} \quad \text{(Eqn. 24)}$$

where X_{obs} and X_{sim} represent the observed and simulated data points and n is the number of data points. The RMSE was computed as

$$\text{RMSE} = \sqrt{\frac{\sum_{i=1}^{n}(X_{obs} - X_{sim})^2}{n}} \quad \text{(Eqn. 25)}$$

The range of the observed data provides an important gauge for determining the degree of error. Smaller ratios of MAE to range indicate that the simulated data has a small degree of deviation from the observed data. The range is calculated by subtracting the minimum value ($X_{obs,min}$) from the maximum value ($X_{obs,max}$) of each observed dataset.

$$\text{Range} = X_{obs,max} - X_{obs,min} \quad \text{(Eqn. 26)}$$

These values, calculated for the period of 4/16/2010 to 4/22/2010, provide a mathematical assessment of the base-case scenario validation. Table 4 lists each station and its corresponding tidal MAE and RMSE values in ascending order of error. The highest tidal MAE and RMSE rates (Shell Beach to D2 in Table 4) are found at stations where recent bathymetric data were unavailable and bathymetries had to be estimated for the mesh. Considering this fact, and the fact that model results will be used to determine trends not magnitudes, the errors at these stations are within a reasonable range. Stations with recent bathymetries and less complex topographies (interior domain and channels) had lower error values.

Table 4 – MAE and RMSE values (in meters) at each tidal calibration station during the period of 4/16/10 to 4/22/10. Stations are shown in ascending order of error.

Station	Tidal MAE (m)	Tidal RMSE (m)	Range (m)
Rigolets	0.0422	0.0520	0.5090
LUMCON	0.0435	0.0592	0.4650
MS Sound at St Joseph Island Light	0.0475	0.0620	0.7803
Pass Manchac	0.0479	0.0643	0.4328
SW Pass, LA	0.0576	0.0693	0.5883
Barataria Pass at Grand Isle	0.0599	0.0765	0.6736
IHNC	0.0621	0.0732	0.5791
Chef Menteur	0.0630	0.0775	0.5761
Shell Beach	0.0790	0.0954	0.6462
MS Sound at Grand Pass	0.0895	0.1100	0.6797
Bay Waveland Yacht Club	0.1092	0.1328	0.8595
D1	0.1180	0.1427	0.9508
NE Bay Gardene	0.1358	0.1717	0.8595
D2	0.1374	0.1627	0.8467

MAE and RMSE values for salinity follow a noticeable trend of increasing error with increasing station depth. This supports the assumption that differences in sensor height account for the majority of the error. Once more, since the model does simulate the transport (signal phase) of salinity trends fairly well, the model data can safely be used for understanding the fluctuations in salinity transport due to barrier island transgression and interior wetland loss.

Table 5 - MAE and RMSE values (in ppt) at each salinity calibration station during the period of 4/16/10 to 4/22/10. Stations are shown in ascending order of error.

Station	Salinity MAE (ppt)	Salinity RMSE (ppt)	Range (ppt)
LUMCON	0.399	0.491	0.652
NE Bay Gardene	0.642	0.893	3.500
Rigolets	0.963	1.338	5.100
D2	1.029	1.158	1.810
D1	1.304	1.800	6.220
MS Sound at St Joseph Island Light	1.383	1.881	5.400
MS Sound at Grand Pass	2.174	2.512	6.100

CHAPTER 5

Results

Tidal Simulation Results

Figure 22 through Figure 25 compare the tidal elevations in meters between model scenarios (Base-case, H1, and H2) for the entire period. Tidal simulation plots for locations not shown in this chapter can be found in Appendix C. The winter storm period of 4/22/10 through 5/7/10 is bounded by the purple box in each figure. These figures (when viewed with the meteorological record in Figure 18) indicate that deviations in tidal simulations coincide with events characterized by increased wind speeds and northerly winds. However, these deviations rarely exceed 2.5 cm. Larger deviations are seen at the NE Bay Gardene station only. Additionally, open water stations (Mississippi Sound and Grand Isle, specifically) seem to be less affected by the changes in bathymetry reproduced in the different scenarios. The tidal phase does not vary significantly between scenarios, but the tidal amplitude does vary with each scenario. The base-case and H1 scenarios have nearly identical phases and amplitudes at all stations except D2.

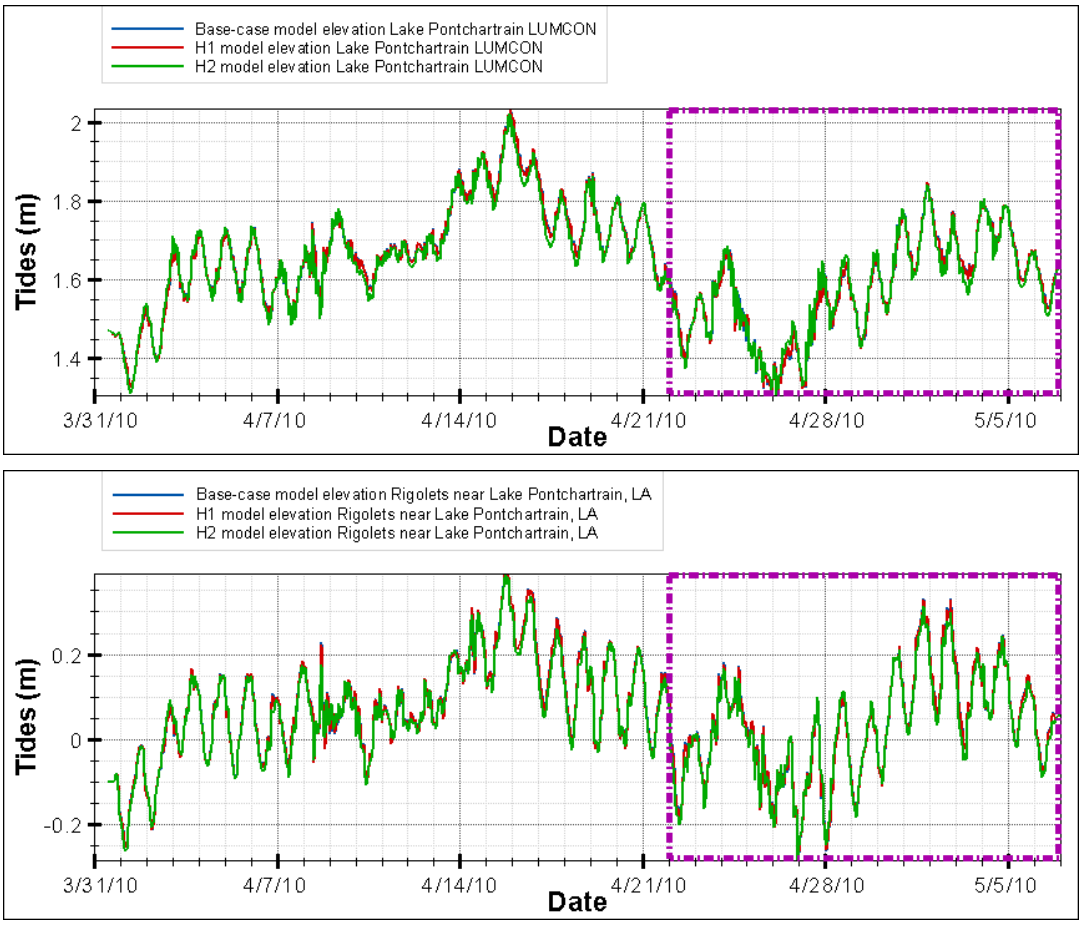

Figure 22 – A comparison of the tidal elevations (in meters) across the model scenarios (Base-case, H1, and H2) at Lake Pontchartrain LUMCON(top) and Rigolets (bottom) for the entire simulation period. The winter storm period of 4/22/10 through 5/7/10 is bounded by the purple box.

The LUMCON and Rigolets tidal signals are similar, but the LUMCON tides show a smaller deviation in elevation between scenarios (Figure 22). The H2 scenario shows a general decrease in

tidal magnitude when compared to the other scenarios. When the base-case and H1 signals deviate, the base-case signal typically has a lower tidal magnitude than the H1 signal.

Similar to Figure 22, the Mississippi Sound at St. Joseph Island Light and D2 stations show similar signals, but the D2 signal has greater deviations between scenarios Figure 23). Peaks where the base-case simulation experienced greater tidal magnitude coincide with strong winds (often from the north). Both stations show a reduction in tidal amplitude between the scenarios, but the deviation is twice as large at the D2 station. At the Mississippi Sound at St. Joseph Island Light station, the H1 signal has a 2.5 cm increase in amplitude from the other scenarios. Where the base-case and H1 signals vary, the base-case amplitude is slightly higher. At D2, the variations in signals occur as a 2.5 cm reduction in tidal amplitude in the H2 case.

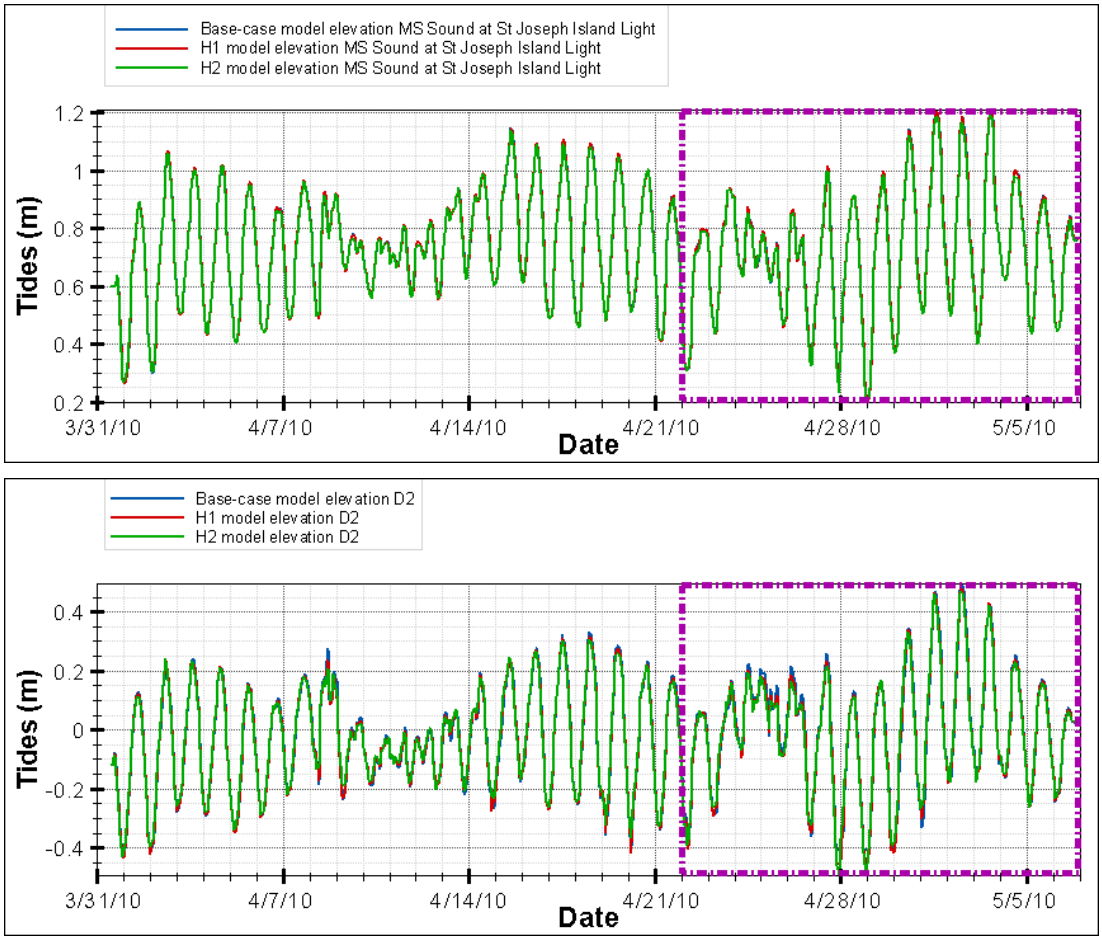

Figure 23 - A comparison of the tidal elevations (in meters) across the model scenarios (base-case, H1, and H2) at the Mississippi Sound at St. Joseph Island Light (top) and D2 (bottom) stations for the entire simulation period. The winter storm period of 4/22/10 through 5/7/10 is bounded by the purple box.

Figure 24 compares scenario results at NE Bay Gardene. This station shows a large variation between model scenarios. The base-case and H1 scenarios are very similar, but they differ from the H2 signal by 0.05 to 0.3 m. The largest variations occur during low tide, and coincide with high or northerly winds. Across the entire period, the H2 tides have a smaller amplitude versus the other scenarios. This station, located in the marsh, logically experiences the most variations during H2 conditions, as it is no longer sheltered by adjacent subaerial marsh.

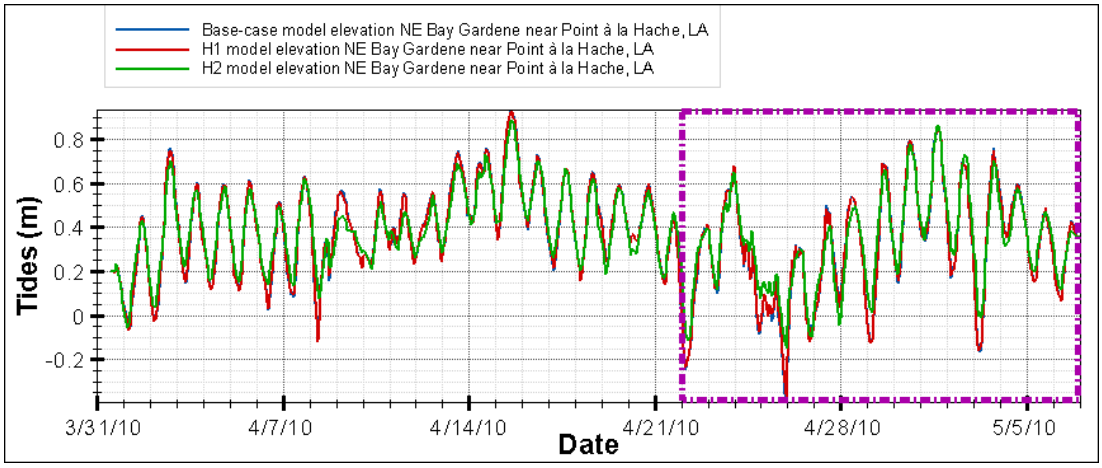

Figure 24 - A comparison of the tidal elevations (in meters) across the model scenarios (base-case, H1, and H2) at the NE Bay Gardene station for the entire simulation period. The winter storm period of 4/22/10 through 5/7/10 is bounded by the purple box.

The Grand Isle station shows the least variability between scenarios. This result is expected since the region is mostly open water and had no marsh or barrier island bathymetric changes. Therefore, the only changes to the surrounding area were due to subsidence. This station indicates that, under the affect of sea level rise alone, the tidal amplitude will differ by a small amount (less than 1 cm) regardless of the scenario. Following the same trend as the other stations, deviations in magnitude between scenarios occur during strong or northerly winds.

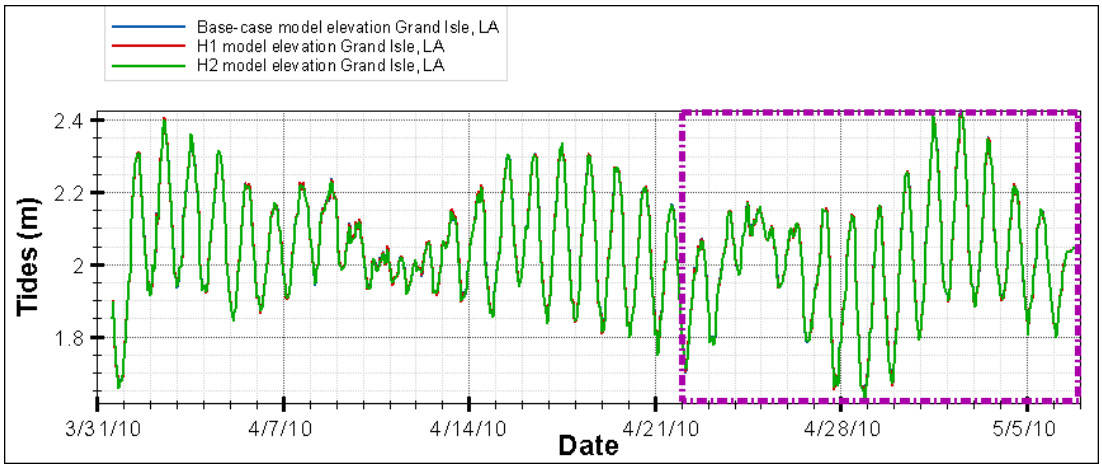

Figure 25 - A comparison of the tidal elevations (in meters) across the model scenarios (base-case, H1, and H2) at the Grand Isle station for the entire simulation period. The winter storm period of 4/22/10 through 5/7/10 is bounded by the purple box.

Salinity Simulation Results

At interior Lake Pontchartrain stations, the differences between scenarios are not noticeable. At open water stations (i.e., Mississippi Sound, D1, and D2), there is an increase in salinity with H2 during normal periods and a decrease during winter storm periods. This indicates that the tidal exchange at open water stations, and therefore exchange of salinity between the coastal ocean and estuary, is amplified under H2 conditions.

Figure 26 through Figure 30 compare the salinity between the model scenarios (base-case, H1, and H2) for the entire simulation period. Salinity simulation plots for stations not shown in this

chapter can be found in Appendix C. The winter storm period of 4/22/10 through 5/7/10 is bounded by the yellow box in each figure. These figures (when viewed with the meteorological record shown in Figure 18) indicate that larger fluctuations in salinity occur during the winter storm period. Deviations in salinity between scenarios and peaks in salinity across all scenarios coincide with high wind speeds. For all stations, these deviations are small (between 0.01 and 0.91 ppt) between the base-case and H1 scenarios (see Figure 48 in the Discussion section). Average differences in salinity are largest (between 0.09 and 2 ppt) between the base-case and H2 scenarios (see Figure 49 in the Discussion section). For all scenario comparison, stations in the marsh and back-barrier of islands had an average difference in salinity that was twice that of interior stations. In all stations except Lake Pontchartrain LUMCON, north winds produce higher salinity levels for at least one day after. This is likely due to increased horizontal mixing resulting from an increase in wind shear. Only D2 showed changes in phase between scenarios.

The LUMCON and Rigolets stations (Figure 26) show a similar reduction in salinity during the H2 scenario, while the base-case and H1 scenarios are very similar. Larger deviations between these scenarios coincide with periods of strong or northerly winds.

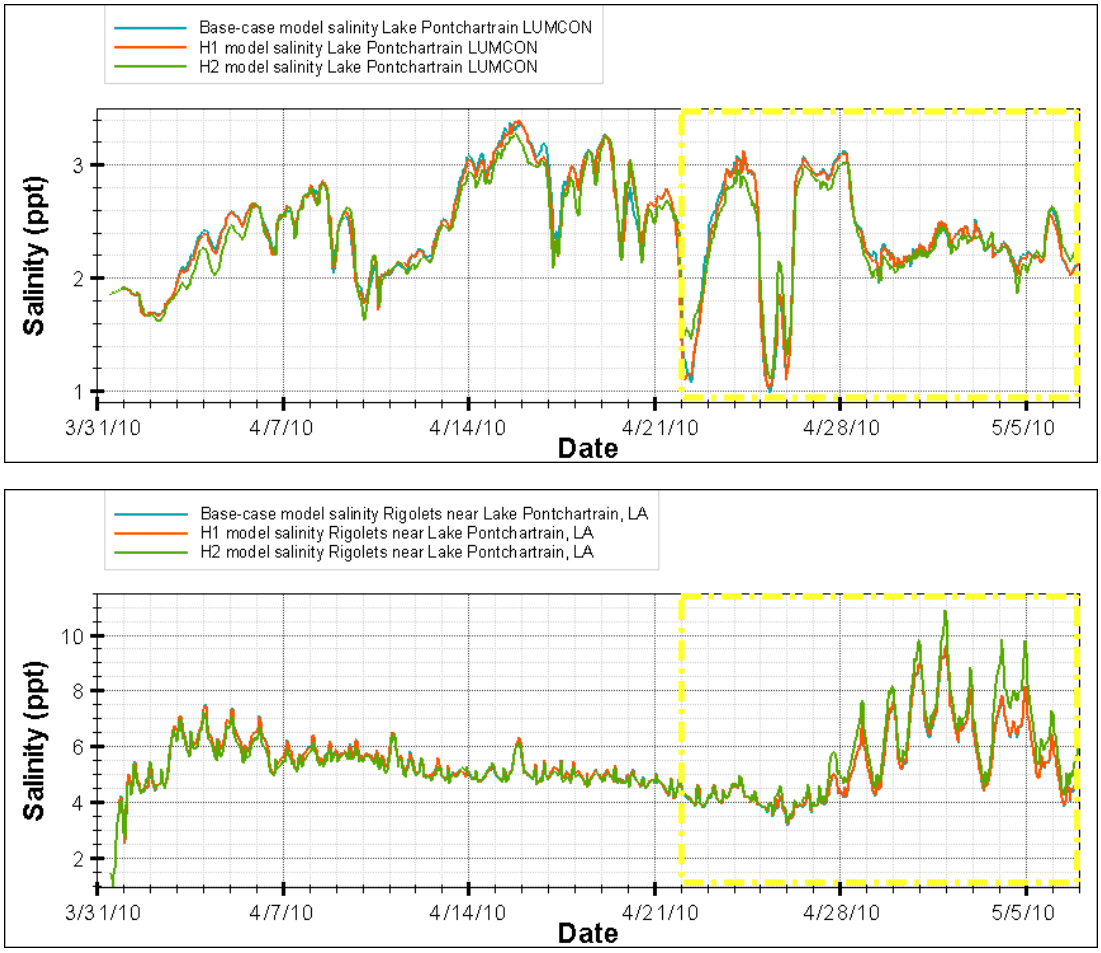

Figure 26 - A comparison of the salinity fluctuations (in ppt) across the model scenarios (base-case, H1, and H2) at Lake Pontchartrain LUMCON (top) and Rigolets (bottom) for the entire simulation period. The winter storm period of 4/22/10 through 5/7/10 is bounded by the yellow box.

The Mississippi Sound at St. Joseph Island Light station (Figure 27) exhibits higher deviations in salinity between scenarios during northerly wind events. Additionally, the H2 salinity levels are constantly higher at this station. Base-case salinities are only slightly smaller than during the H1 scenario throughout the period.

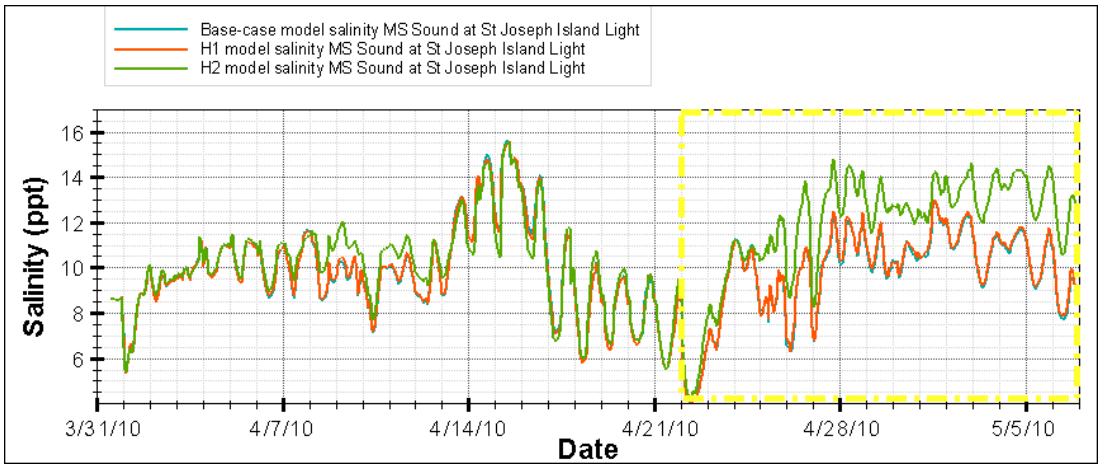

Figure 27 - A comparison of the salinity fluctuations (in ppt) across the model scenarios (base-case, H1, and H2) at the Mississippi Sound at St. Joseph Island Light station for the entire simulation period. The winter storm period of 4/22/10 through 5/7/10 is bounded by the yellow box.

The D2 station had some of the most noticeable signal differences from the plots shown in this section (Figure 28). Variations in wind direction cause departures between the base-case/H2 and H1, while variations in wind speed cause deviations in the base-case/H1 and H2. Increased wind speeds promote higher salinities during the H2 scenario, and generally, these high fluctuations in salinity occur during the winter storm period.

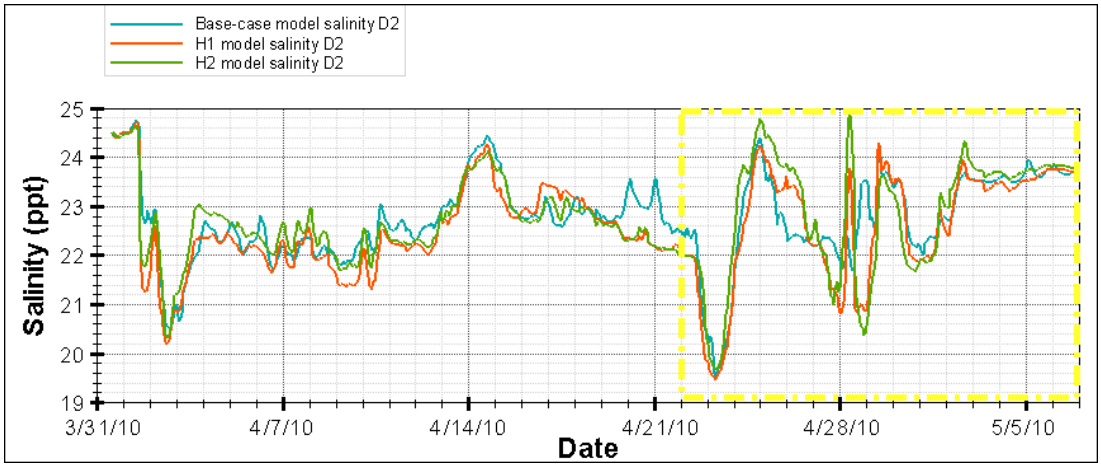

Figure 28 - A comparison of the salinity fluctuations (in ppt) across the model scenarios (base-case, H1, and H2) at the D2 for the entire simulation period. The winter storm period of 4/22/10 through 5/7/10 is bounded by the yellow box.

The salinity at NE Bay Gardene, similar to D2, has large fluctuations during the winter storm event (Figure 29). A decreasing trend in the salinity during the H2 scenario indicates a more uniformly mixed system once the marsh has deteriorated. The H2 signal has greater amplitudes as well, implying that this station is more dynamic due to a lack of sheltering by adjacent marsh during the H2 scenario.

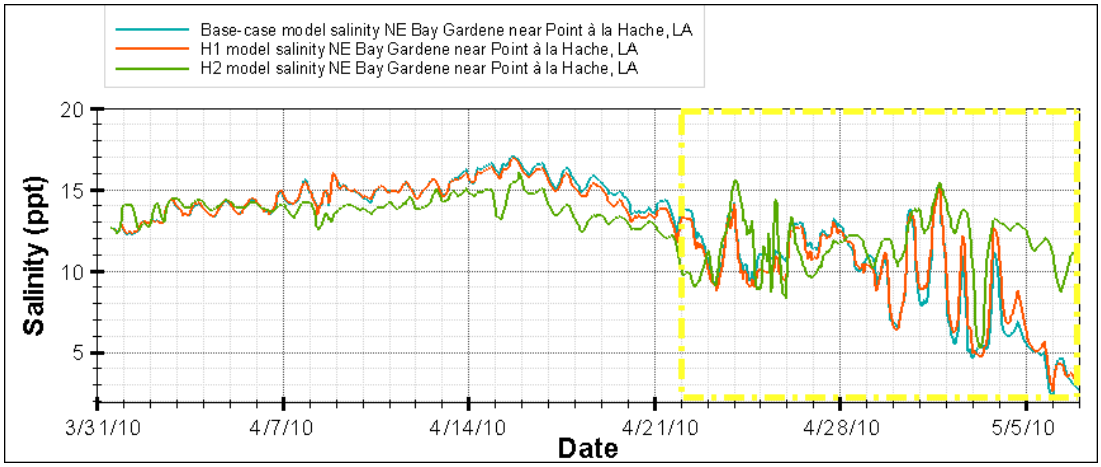

Figure 29 - A comparison of the salinity fluctuations (in ppt) across the model scenarios (base-case, H1, and H2) at the NE Bay Gardene station for the entire simulation period. The winter storm period of 4/22/10 through 5/7/10 is bounded by the yellow box.

Similar to tidal elevations, at Grand Isle there are slight differences in salinity between scenarios. A small difference (maximum ~ 1 ppt) between the base-case/H1 and H2 scenarios occurs during strong wind events. Again, the winter storm period produces greater fluctuations in salinity magnitude.

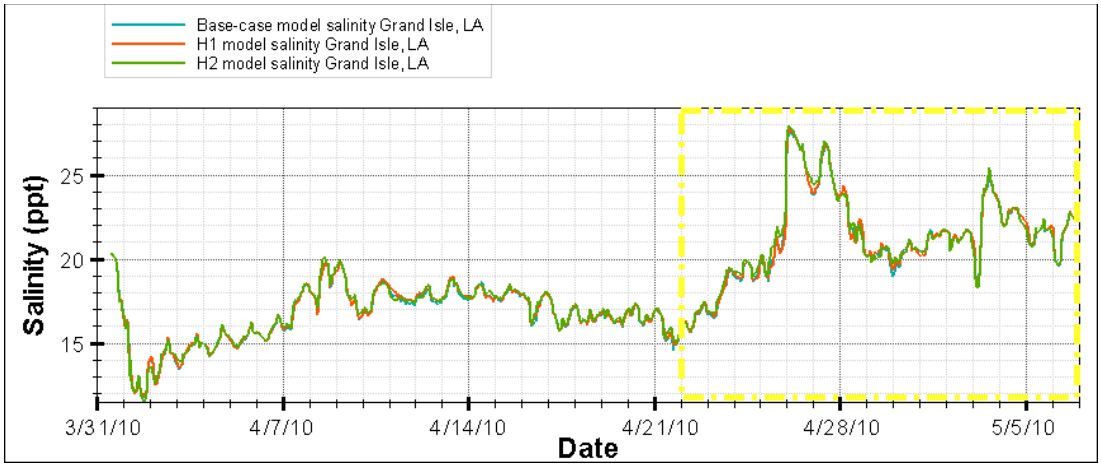

Figure 30 - A comparison of the salinity fluctuations (in ppt) across the model scenarios (base-case, H1, and H2) at the Grand Isle station for the entire simulation period. The winter storm period of 4/22/10 through 5/7/10 is bounded by the yellow box.

Flow Analysis

Flow analysis was conducted to determine instantaneous flow through critical areas of the estuary and to assess tidal prism, flood, and ebb average flow during the period of interest. The flow analysis results for a period representing average conditions (April 16 through April 21), as well as one that represents a winter storm condition (April 22 through May 7) can be found in Table 6 and Table 7, respectively. These tables show that during normal conditions the entire system is ebb-dominant with the exception of Bayou La Loutre, which becomes flood dominant after marsh degradation (H2). During winter storm conditions, however, the ICWW, and Ship Island to Hewes Point are flood-dominant. The Rigolets, Chef Menteur, and Bayou La Loutre are flood-dominant except during H2, which indicates that the lack of marsh causes a new circulation pattern to develop when strong north winds are present. The remaining transects are ebb-dominant during all winter storm scenarios. This analysis indicates that northerly winds introduce a new circulation pattern into the system. Once the marsh deteriorates, the sites (except the ICWW) have the same flow dominance as during normal or average conditions.

Table 6 - Average flood and ebb flows (m^3/s) through each transect during normal conditions (April 16 through April 21).

Transect Name	Average flood flow (m^3/s)			Average ebb flow(m^3/s)			Flow Dominance
	Base-case	H1	H2	Base-case	H1	H2	
Bayou La Loutre	-68.1	-69.1	-105	38.7	46.9	112	Flood except H2
Cat Island	-8218	-8413	-9486	10235	10174	11856	Ebb
Chef Menteur	-517	-536	-600	660	662	762	Ebb
Half Moon Island	-7155	-7297	-8709	8677	8810	10781	Ebb
Chandeleur Islands	-31118	-32315	-36039	35509	37109	45332	Ebb
ICWW	-400	-408	-476	478	485	541	Ebb
Rigolets	-2216	-2188	-2559	2719	2815	3038	Ebb
Ship Island to Hewes Point	-23143	-22393	-21022	30929	29936	28753	Ebb

Table 7 - Average flood and ebb flows (m^3/s) through each transect during winter storm conditions (April 22 through May 7).

Transect Name	Average flood flow (m^3/s)			Average ebb flow(m^3/s)			Flow Dominance
	Base-case	H1	H2	Base-case	H1	H2	
Bayou La Loutre	-65.4	-68.5	-107	38.1	47.6	131	Flood except H2
Cat Island	-8478	-8580	-10005	9923	9970	10815	Ebb
Chef Menteur	-639	-648	-706	633	642	713	Flood except H2
Half Moon Island	-8240	-8341	-9805	8646	8832	10117	Ebb
Chandeleur Islands	-25367	-26482	-30679	35807	37242	43273	Ebb
ICWW	-536	-551	-574	401	401	461	Flood
Rigolets	-2543	-2610	-2831	2530	2535	2875	Flood except H2
Ship Island to Hewes Point	-29012	-28912	-29061	24718	23794	23074	Flood

The percent change in flow between normal conditions and winter storms was calculated with the results shown in Table 8. Only the transect along the Chandeleur Islands does not show a decrease in ebb flow during winter storm conditions under present conditions. From the analysis performed in Table 6 and Table 7, the Chef Menteur, Rigolets, ICWW, and Ship Island to Hewes Point transects show the largest percent changes, describing the shift from an ebb- to flood-dominant transect during winter storm conditions.

Table 8 – Comparison of the normal period and the winter storm period (Table 6 and Table 7) in terms of percent change in flow through each transect. Negative percentages indicate that the flow (ebb or flood) was reduced due to winter storms.

	Percent difference in flood flow			Percent difference in ebb flow		
Transect Name	**Base-case**	**H1**	**H2**	**Base-case**	**H1**	**H2**
Bayou La Loutre	-4.06%	-0.76%	1.89%	-1.65%	1.42%	14.6%
Cat Island	3.06%	1.95%	5.19%	-3.14%	-2.05%	-9.63%
Chef Menteur	19.2%	17.4%	15.1%	-4.34%	-3.03%	-6.91%
Half Moon Island	13.2%	12.5%	11.2%	-0.37%	0.24%	-6.56%
Chandeleur Islands	-22.7%	-22.0%	-17.5%	0.83%	0.36%	-4.76%
ICWW	25.3%	25.8%	17.1%	-19.3%	-20.8%	-17.5%
Rigolets	12.8%	16.2%	9.62%	-7.47%	-11.1%	-5.67%
Ship Island to Hewes Point	20.2%	22.5%	27.7%	-25.1%	-25.8%	-24.6%

Time-dependent contour plots of flow through each transect were constructed and analyzed to further isolate the cause and accurately determine the location of the simulated changes in flow direction and magnitude discussed in previous sections. These figures show the transect's evolution in time (y-axis) and space (x-axis) of a selected quantity (in this case flow perpendicular to the transect). This allows for dynamic observations to be viewed statically, and quickly infer likely meteorological influences on estuarine exchange, as well as to identify regional changes or departures in instantaneous flow (and hence exchange) at a given instant in time. The contour plots describe conditions during the winter storm (from 4/16/10 through 5/7/10). In wide channels where there was a noticeable channel for flow, a contour plot with a magnified x-axis is provided. All transect distances originate at the northern end of the transect. The ICWW and Chef Menteur flows are illustrated through a line graph because of the small cross-sectional area of the channel. Figure 31 through Figure 41 show that the passing of a winter storm (from 4/28/10 to 5/3/10) does increase the magnitude of flow, as expected. Additionally, the instantaneous flow increases from the present day conditions to H1 and H2 conditions, respectively. This change is a direct reflection of the increase in tidal prism, caused by an increase in the increase in the bay area contributing to the tidal prism due to the conversion of interior wetlands to open water (Jarrett, 1976; O'Brien, 1969).

Flow through Bayou La Loutre (Figure 31) shows a significant increase in the flow magnitude, especially during the H2 scenario (significant interior wetland loss). During both neap and flood tides, Bayou La Loutre is flood-dominant; however, during neap tide the flood-dominant flow is rather small. Figure 31 shows that the majority of the flow through this transect, logically, is confined within the deep existing channel.

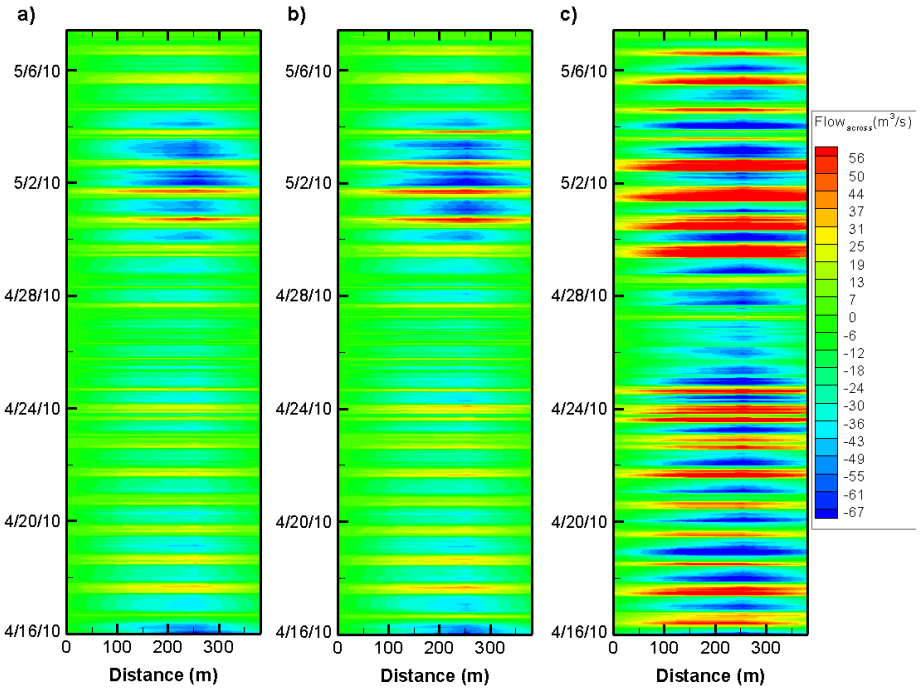

Figure 31 – Contour plot (time and space variant) of Bayou La Loutre cross-shore flux in m^3/s during the three simulation scenarios: (a) Base-case, (b) H1, and (c) H2. Distance is from north to south.

Up-estuary, at the Rigolets, we notice nearly constant instantaneous flow across the transect, likely due to the uniform depth and narrow width of the channel (Figure 32). The flow across this transect becomes more flood-dominant with the passage of a winter storm, but is affected only slightly when compared to other scenarios.

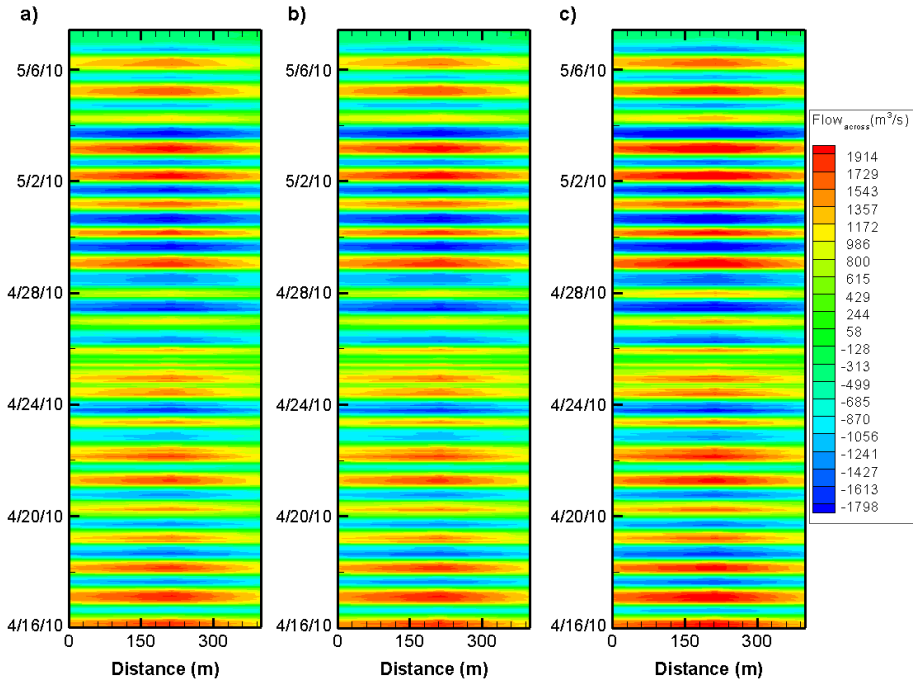

Figure 32 - Contour plot (time and space variant) of the Rigolets transect's cross-shore flux in m^3/s during the three simulation scenarios: (a) Base-case, (b) H1, and (c) H2. Distance is from north to south.

At Cat Island, the majority of the flow through the transect is confined to the deep navigation channel present (Figure 33). Figure 34 shows a closer view of this channel (from 4,000 to 7,000 m) along the transect. Similar to Bayou La Loutre, neap tides are flood-dominant with the ebb-flows along this transect being very small. The flows occurring during the winter storm have larger flood-dominance when compared to those produced during normal conditions.

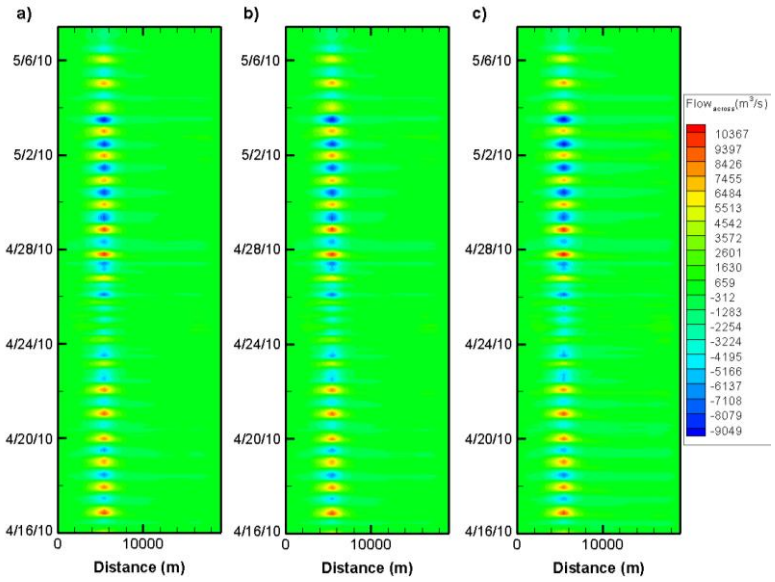

Figure 33 - Contour plot (time and space variant) of Cat Island cross-shore flux in m^3/s during the three simulation scenarios: (a) Base-case, (b) H1, and (c) H2. Distance is from north to south.

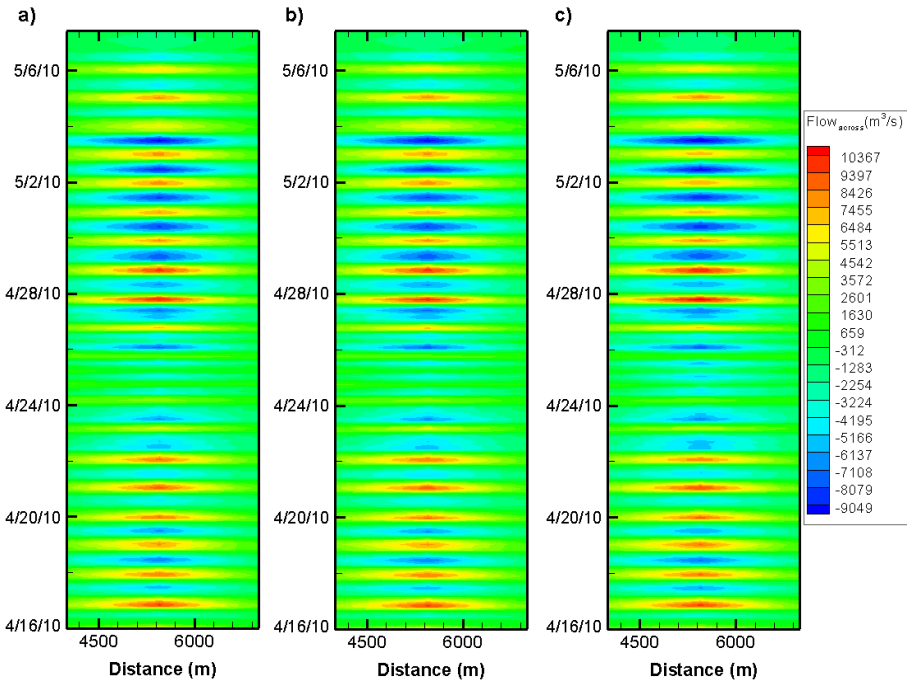

Figure 34 - Contour plot (time and space variant) of the primary Cat Island channel cross-shore flux in m^3/s from distance 4,000 to 7,000 m from north to south during the three simulation scenarios: (a) Base-case, (b) H1, and (c) H2. Distance is from north to south.

The majority of the flow across the Half Moon Island transect passes through the northern end of the transect (Figure 35), and flows occurring both during spring and neap tides are ebb-dominant. Flow during the winter storm has a greater magnitude, but remains ebb-dominant. Figure 36 shows a closer view of this primary flow channel (from 0 to 4,000 m) along the transect.

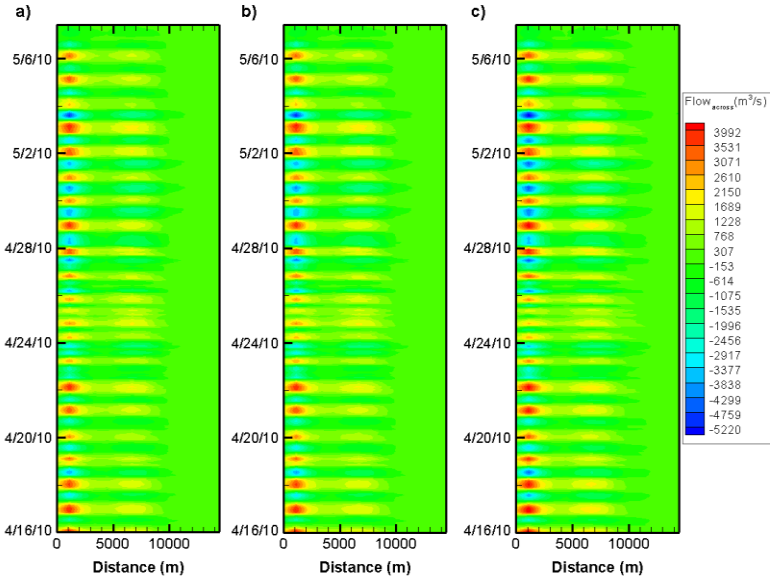

Figure 35 - Contour plot (time and space variant) of Half Moon Island cross-shore flux in m^3/s during the three simulation scenarios: (a) Base-case, (b) H1, and (c) H2. Distance is from north to south.

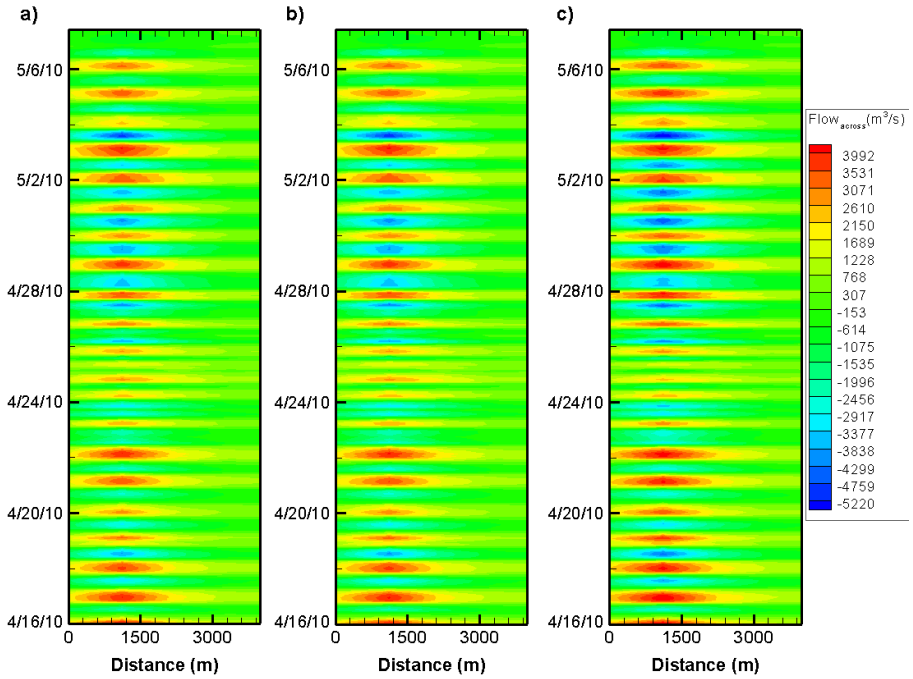

Figure 36 - Contour plot (time and space variant) of the primary Half Moon Island channel cross-shore flux in m^3/s from distance 0 to 4,000 m from north to south during the three simulation scenarios: (a) Base-case, (b) H1, and (c) H2. Distance is from north to south.

Along the Chandeleur Islands, the majority of flow passes through the southern end (near the historic MRGO channel; between Grand Gossier Island and Breton Island) (Figure 37). Figure 38 shows this primary conveyance channel as well as the region southwest of Breton Island in detail. It reveals that the region is ebb-dominant, with only small flow differences between the scenarios simulated.

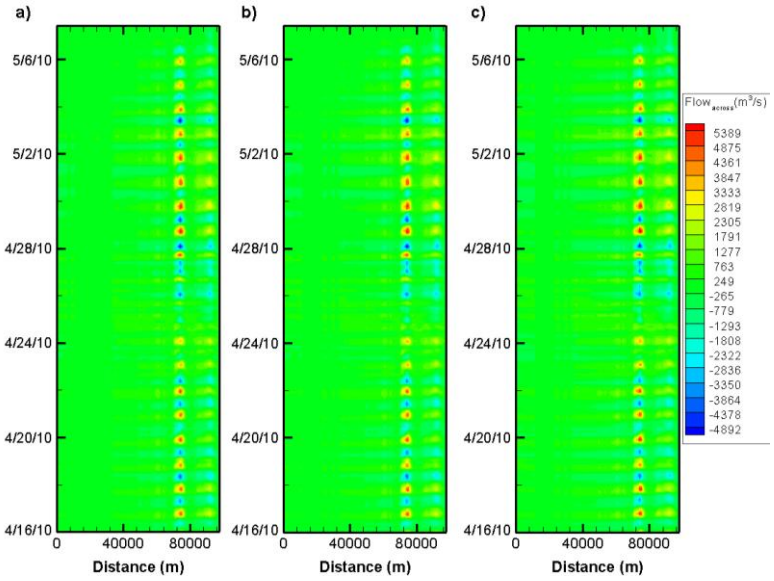

Figure 37 - Contour plot (time and space variant) of the Chandeleur Island transect's cross-shore flux in m^3/s during the three simulation scenarios: (a) Base-case, (b) H1, and (c) H2. Distance is from north to south.

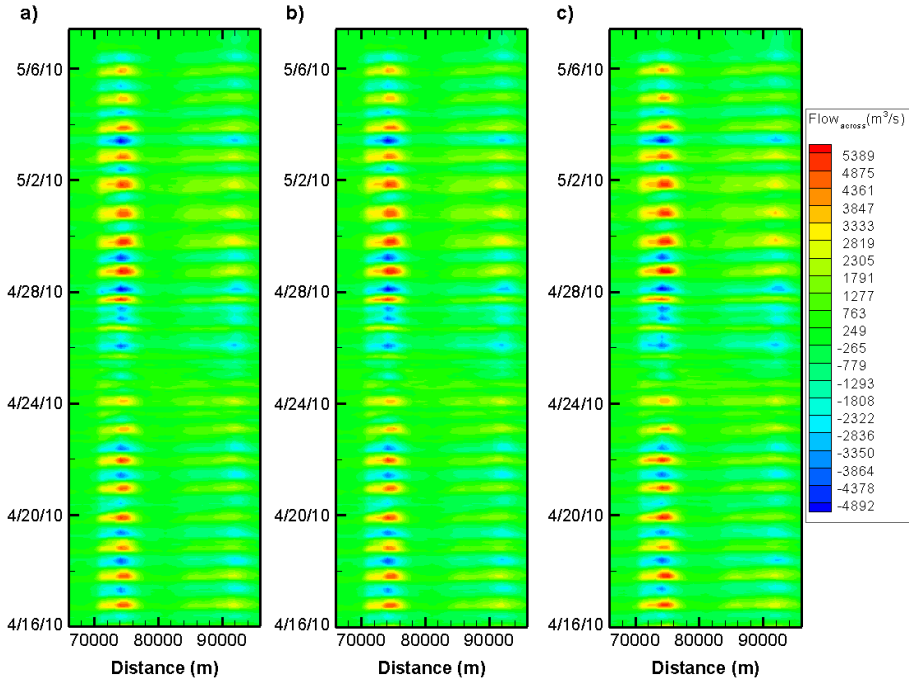

Figure 38 - Contour plot (time and space variant) of the primary Chandeleur Island transect's cross-shore flux in m^3/s from distance 66,000 to 96,000 m from north to south during the three simulation scenarios: (a) Base-case, (b) H1, and (c) H2. Distance is from north to south.

Flow across the transect from Ship Island to Hewes Point is concentrated at the southern end, as seen in Figure 39. Flow is ebb-dominant during normal conditions and flood-dominant during winter storm conditions. There is only a slight difference in flow magnitude between the bathymetric scenarios.

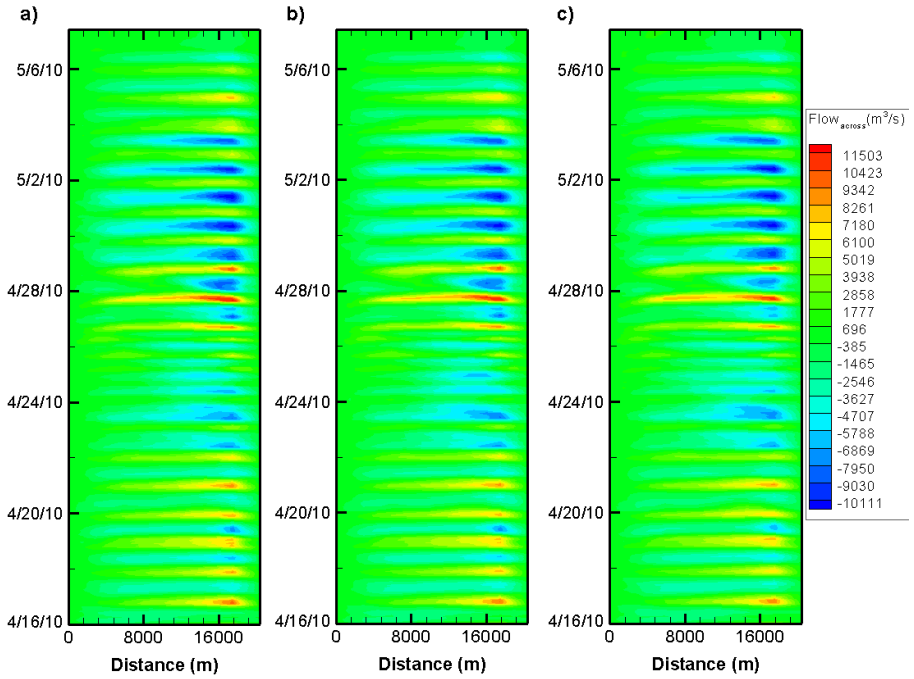

Figure 39 - Contour plot (time and space variant) of the Ship Island to Hewes Point transect's cross-shore flux in m^3/s during the three simulation scenarios: (a) Base-case, (b) H1, and (c) H2. Distance is from north to south.

Both the Chef Menteur and ICWW transects are flood-dominant during neap tide (Figure 40 and Figure 41, respectively). In addition, both transects experience an increase in flow magnitude during H2 conditions, indicating an increase in exchange flows into Lakes Pontchartrain and Maurepas. Moreover, winter storms cause a stronger flood-dominant response across these transects.

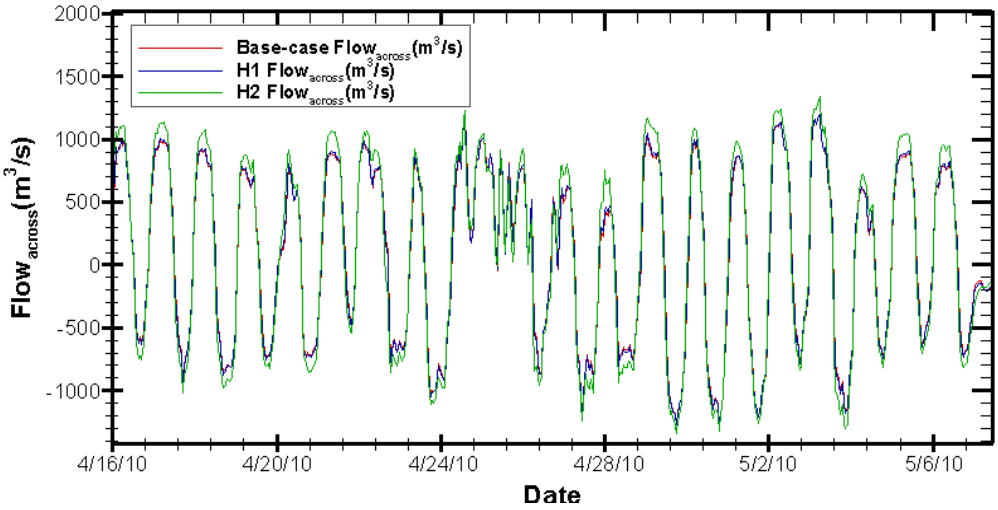

Figure 40 – Instantaneous flow (m^3/s) across the Chef Menteur transect during the three simulation scenarios: Base-case, H1, and H2.

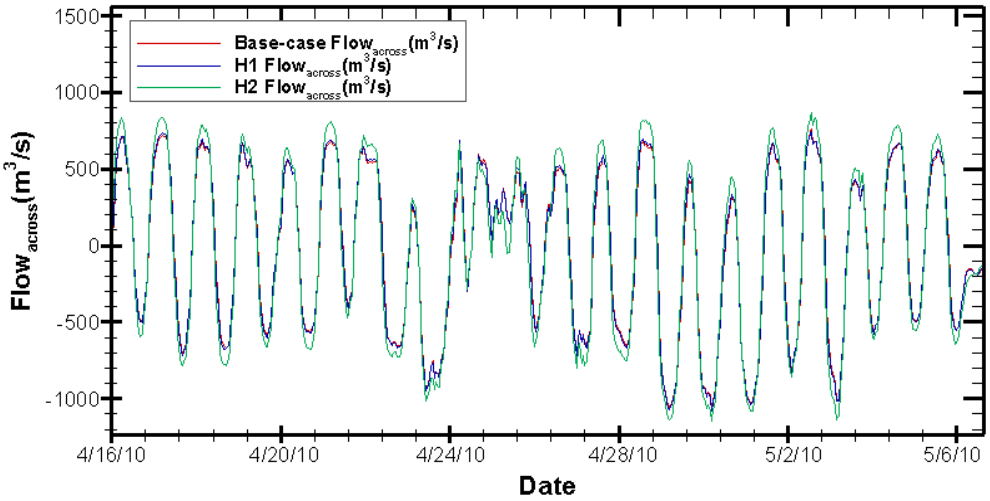

Figure 41 - Instantaneous flow (m³/s) across the ICWW transect during the three simulation scenarios: Base-case, H1, and H2.

To examine possible phase differences between scenarios and throughout the estuary, from lower to upper, instantaneous flows (m³/s) across each transect were plotted against time (Figure 42 to Figure 45). The estuary was divided into the upper, middle, lower-middle, and lower basin (or region of the domain). The upper basin includes the ICWW, Chef Menteur, and Rigolets transects. The middle basin is comprised of the Half Moon Island and Bayou La Loutre transects. The Cat Island transect is the lower-middle basin. The lower basin includes the Ship Island to Hewes Point transect and the Chandeleur Island transect. By comparison of flow between the H1 and H2 scenarios during the normal period (Figure 42 and Figure 43, respectively) we clearly see a two to three hour phase difference between each region. Logically, under a progressive wave behavior, high tide reaches the lower estuary first and propagates up-estuary. As a result, the apparent tidal prism throughout the estuary will be proportional to the tidal range. We can see that while the flow magnitude changes between scenarios, the phase is nearly identical. This suggests that the loss of interior wetlands does not significantly affect tidal attenuation, despite the respective increase in tidal prism.

By comparing the flows for the H1 and H2 scenarios during the winter storm period (Figure 44 and Figure 45, respectively) we see a similar phase difference between each region (two to three hours). In addition, we see similar tidal wave propagation characteristics through the estuary, showing a proportional increase in flow magnitude between scenarios despite the lack of changes observed in phase. The flow magnitudes during the winter period are greater than the flow magnitudes during the normal period; this was previously confirmed in this study.

Figure 42 through Figure 45 show that the instantaneous flow magnitudes in the lower basin are approximately seven times higher than flow magnitudes in the lower-middle basin. Flow magnitudes in the lower-middle basin are approximately 1.5 times higher than flow magnitudes in the middle basin. Flow magnitudes in the middle basin are approximately 2.25 times higher than flow magnitudes in the upper basin. This is a direct result of the small tidal channels and tidal prism in those regions. The flow magnitudes are largest in the lower basin and decrease towards the upper basin, confirming the progressive nature of the tidal wave.

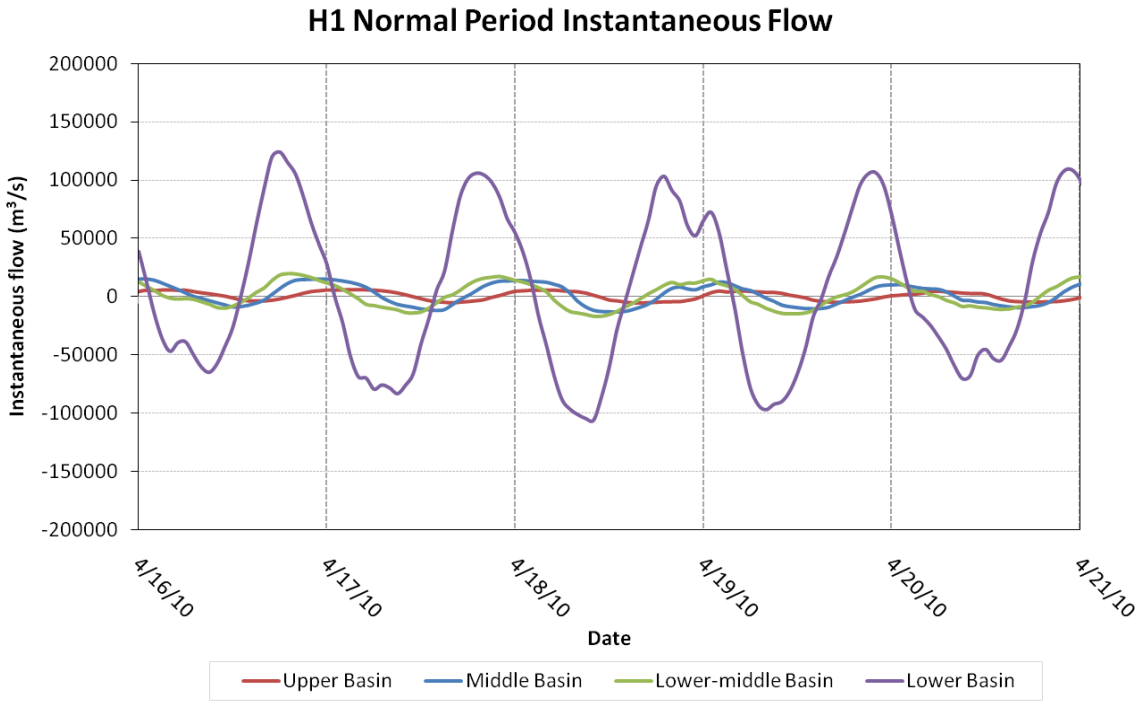

Figure 42 – H1 instantaneous flow (m^3/s) across the domain during the normal period. The domain was divided into sections referred to as the upper, middle, lower-middle, and lower basin.

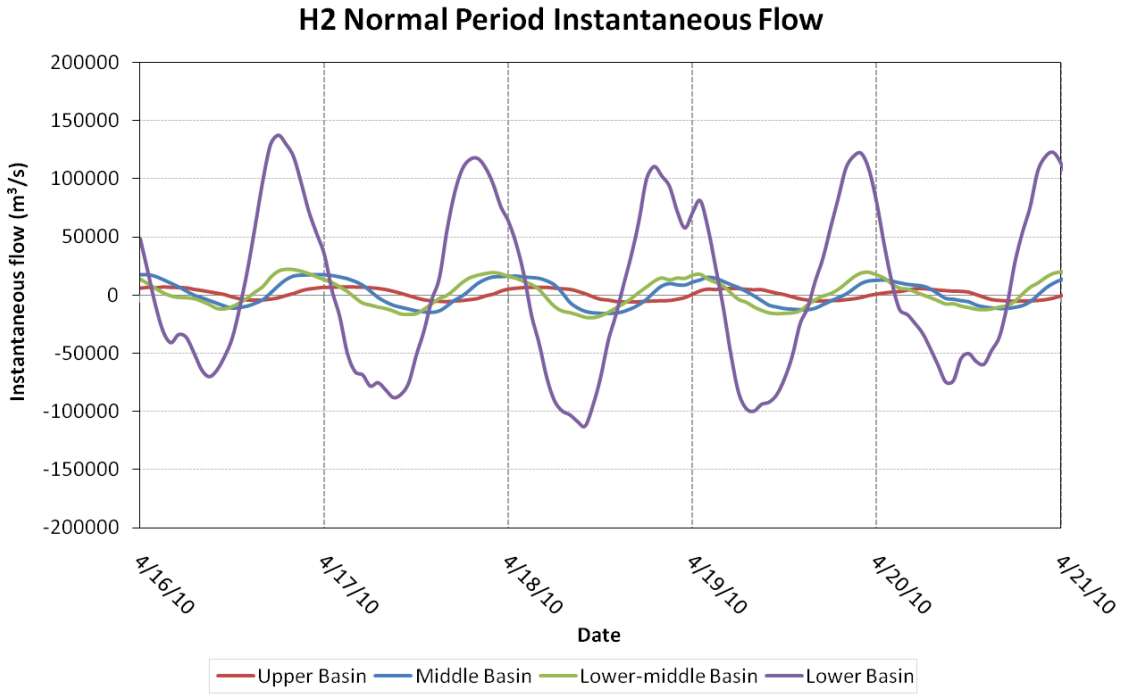

Figure 43 – H2 instantaneous flow (m^3/s) across the domain during the normal period. The domain was divided into sections referred to as the upper, middle, lower-middle, and lower basin.

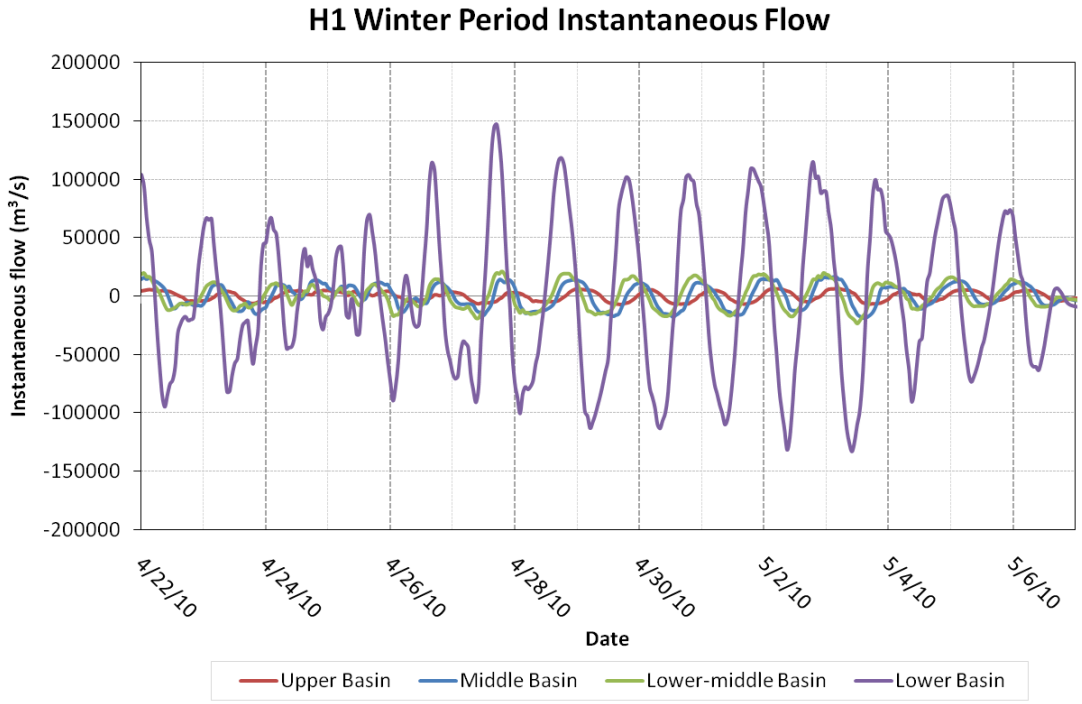

Figure 44 – H1 instantaneous flow (m^3/s) across the domain during the winter storm period. The domain was divided into sections referred to as the upper, middle, lower-middle, and lower basin.

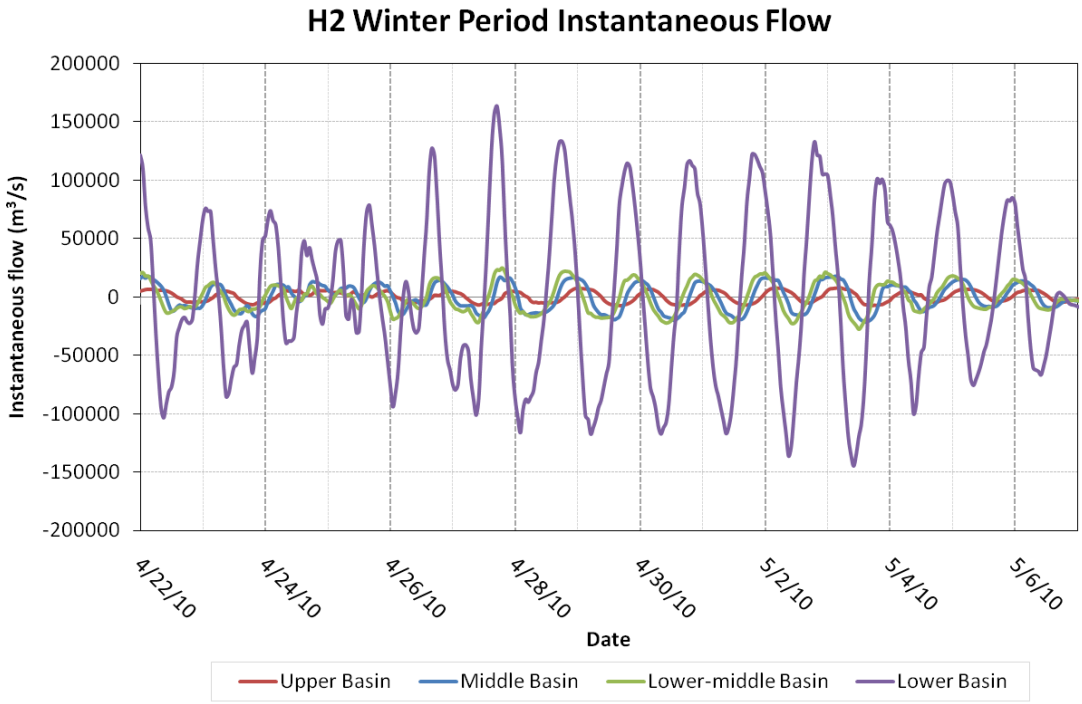

Figure 45 – H2 instantaneous flow (m^3/s) across the domain during the winter storm period. The domain was divided into sections referred to as the upper, middle, lower-middle, and lower basin.

Discussion

Figure 46 through Figure 47 compare the average difference in tides at each location that analysis was performed. These figures compare the base-case to H1 and base-case to H2 scenarios, respectively. Figure 48 through Figure 49 compare the average difference in salinity at each location that analysis was performed. These figures compare the base-case to H1 and base-case to H2 scenarios, respectively. In Mississippi Sound, a general increase in salinity was evident once the interior marsh was converted to open water. It is believed that this increase is the result of increased exchange between the coastal ocean and interior estuaries. This trend was not obvious by observing the change in tidal signature alone. In fact, even when tidal fluctuations were approximately equal, the resulting transport at these open water areas was significantly different. This increase in salinity indicates that the loss of protection offered by the wetlands alters regional circulation patterns, and therefore tidal transport.

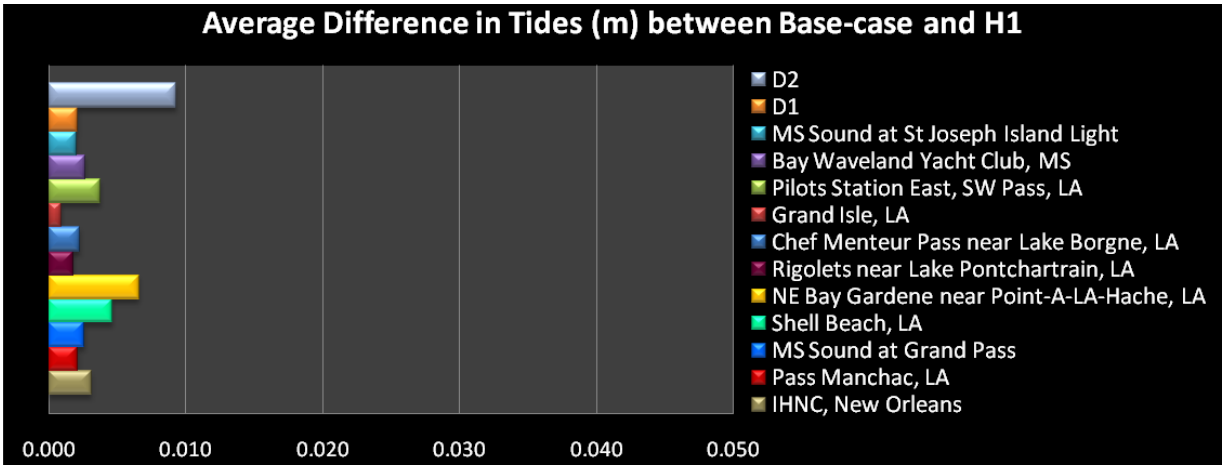

Figure 46 - Average difference in tides (m) between the base-case and H1 scenarios. Tides were averaged over the entire simulation period.

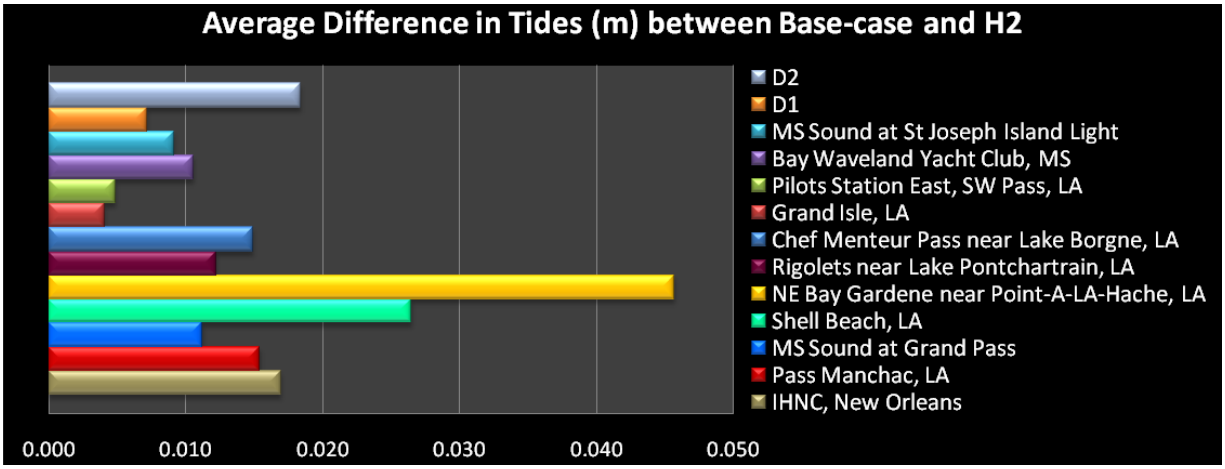

Figure 47 - Average difference in tides (m) between the base-case and H2 scenarios. Tides were averaged over the entire simulation period.

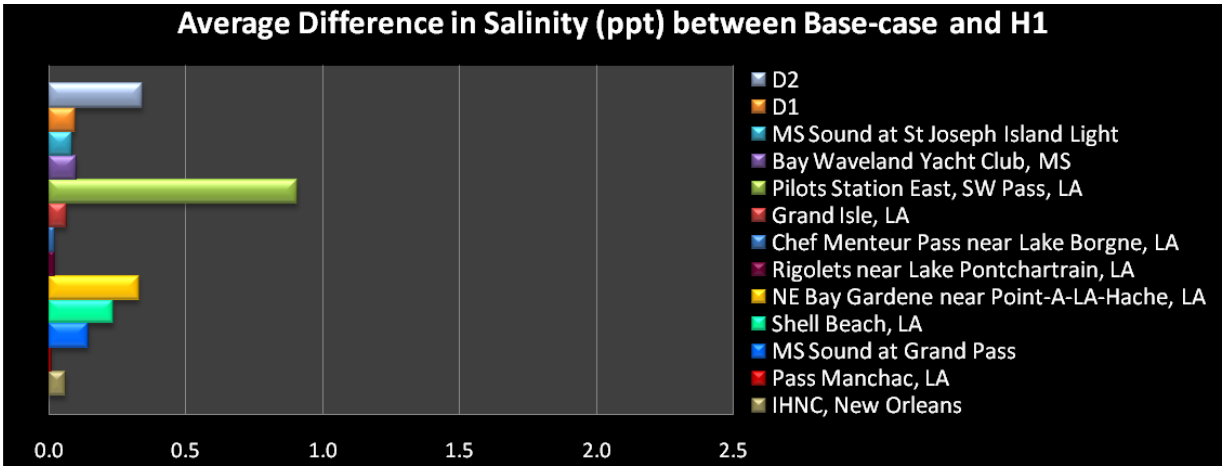

Figure 48 - Average difference in salinity between the base-case and H1 scenarios (salinity in ppt). Salinity was averaged over the entire simulation period.

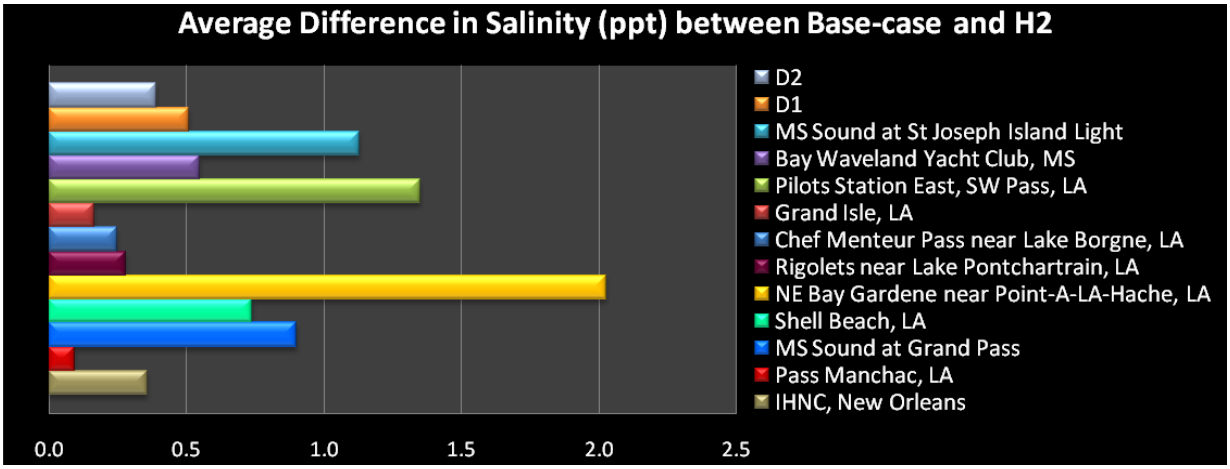

Figure 49- Average difference in salinity between the base-case and H2 scenarios (salinity in ppt). Salinity was averaged over the entire simulation period.

The winter storm circulation patterns between the base-case and H1 scenarios are identical with the exception of the Chef Menteur Pass. During the H2 scenario, the winter storm alters the circulation pattern dramatically, indicating that circulation patterns are highly dependent on wind direction and speed. It should be noted that the dominance across each transect described in Table 6 and Table 7 is averaged over the entire transect length. Across the Cat Island transect, for instance, a close examination of velocity direction indicates that the flow during westerly winds (base-case scenario) is flood-dominant in the existing navigation channel, but ebb-dominant towards the southern end of the transect near the Biloxi marsh (Figure 50). In Figure 50, the arrows represent velocity vectors that describe in which direction the current is moving. The length of the vector indicates the current magnitude (the upper right corner of Figure 50 shows the reference vector). Color contours in Figure 50 represent water elevation above mean sea level. This is an image of one such time on 4/25/10 when the flow was flood-dominant in the existing navigation channel but ebb-dominant towards the southern end of the transect. At this time, the winds were 15 m/s from the west/southwest. Because the water depth is greater in the channel,

the current magnitude (vector length) is higher near the shallow, southern end of the transect. This explains why Table 7 shows the Cat Island transect as ebb-dominant while the Rigolets and Ship Island to Hewes Point transects are flood-dominant.

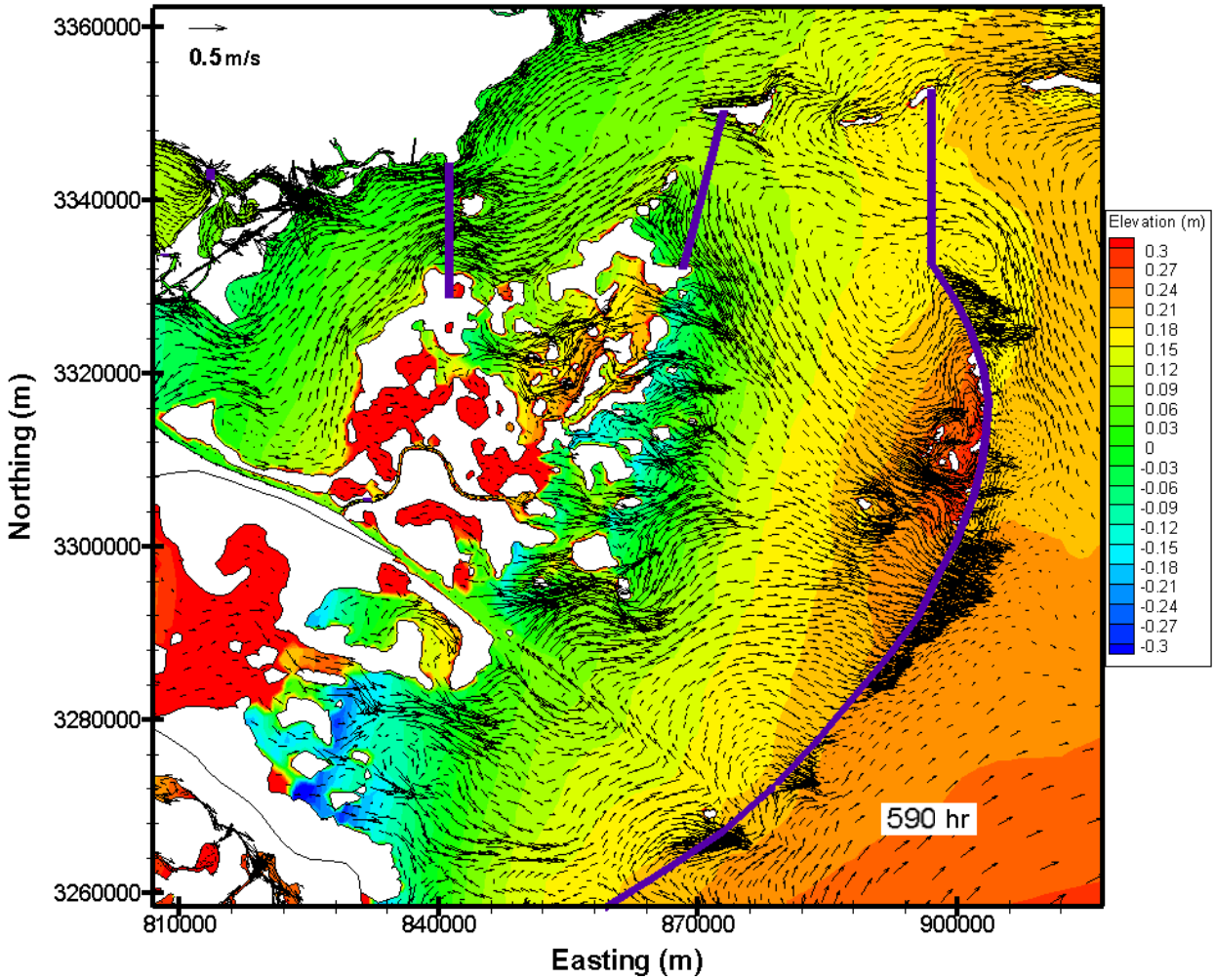

Figure 50 – Base-case water elevation as well as depth-averaged current velocity and magnitude on 4/25/10; winds are 15 m/s from the west/southwest. The velocity vectors orientation indicates the direction the current is moving. The length of the vector indicates the current magnitude (see upper right corner of figure for reference vector). Color contours represent water elevation above mean sea level.

The color contours in Figure 50 show the water setup (high water elevation) in the back-barrier of the Chandeleur Islands and the western edge of the domain and setdown (low water elevation) at the eastern end of the domain caused by high westerly winds. Current velocities between scenarios differ due to changes in depth. The depth-averaged current velocities (represented by vector length) are higher in the base-case scenario (Figure 50) than in the H2 scenario (Figure 51). This is especially noticeable near the Chandeleur Islands and the Biloxi marshes. Because current magnitude decreases with depth (due to boundary layer friction and the inability of wind shear to transfer momentum through the water column), an increase in water

depth coincides with a decrease in depth-averaged current magnitude. It is therefore logical that, in the H2 scenario, the current velocity decreases in these regions.

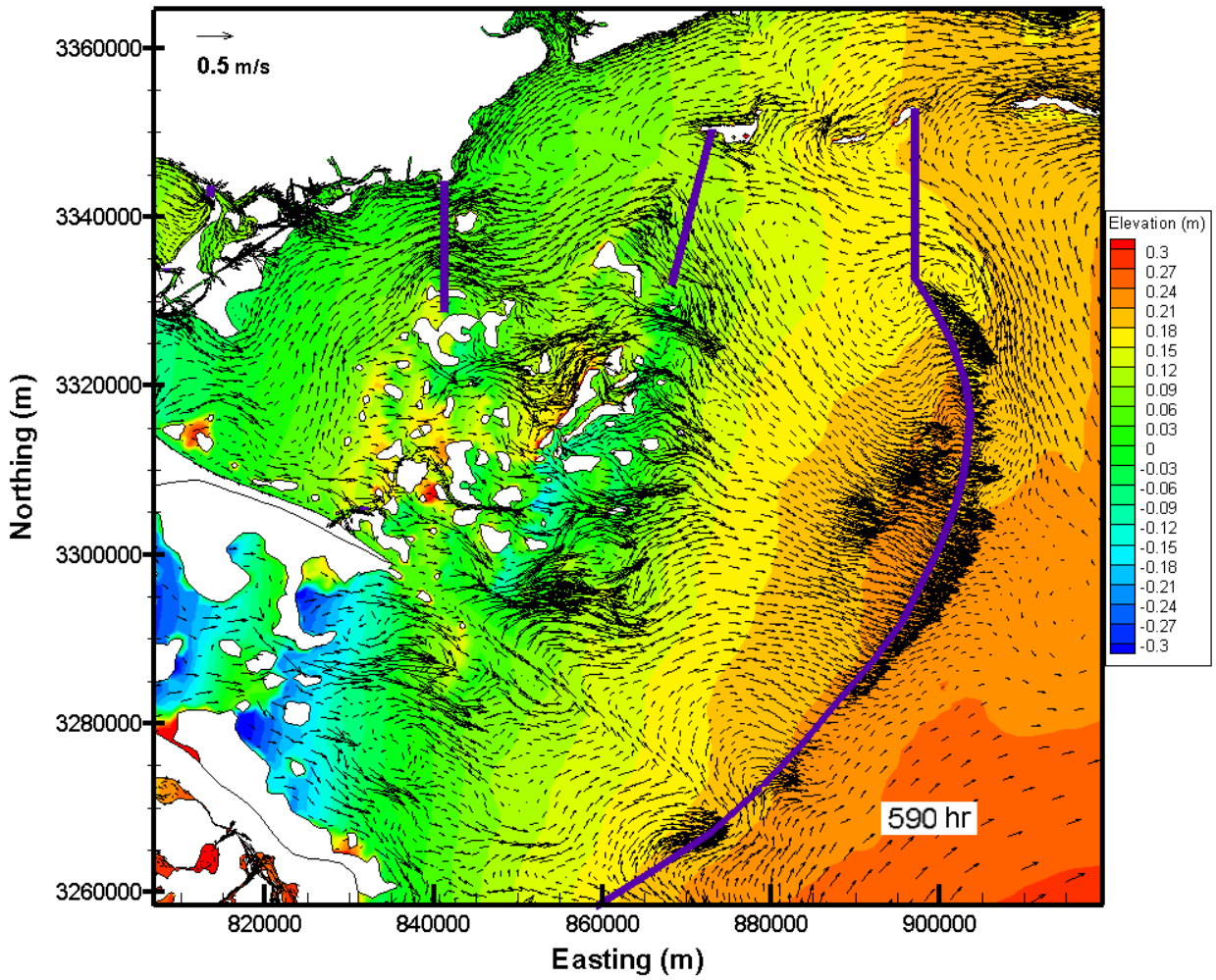

Figure 51 – H2 water elevation as well as depth-averaged current velocity and magnitude on April 25, 2010; winds are 15 m/s from the west/southwest. The velocity vectors orientation indicates the direction the current is moving. The length of the vector indicates the current magnitude (see upper right corner of figure for reference vector). Color contours represent water elevation above mean sea level.

Overall, the system's circulation pattern is altered by both the lack of buffering by the interior marsh and the increase in available fetch present once wetlands have converted to open water (Figure 52). During normal conditions, circulation patterns remain primarily the same, with the exception of Bayou La Loutre, which becomes ebb-dominant.

The reduction in salinity at NE Bay Gardene during average conditions after significant wetland loss is perhaps due to the conversion of Bayou La Loutre from flood- to ebb- dominant. For the same scenario (significant wetland loss) but during winter storm events, the salinity at this location is higher compared to all other scenarios. This could be in part due to altered circulation patterns, resulting in more flushing near the site once the marsh is submerged or eroded.

Therefore, the freshwater being transported through Bayou La Loutre mixes with Chandeleur Sound waters more rapidly once the nearby marsh is converted to open water.

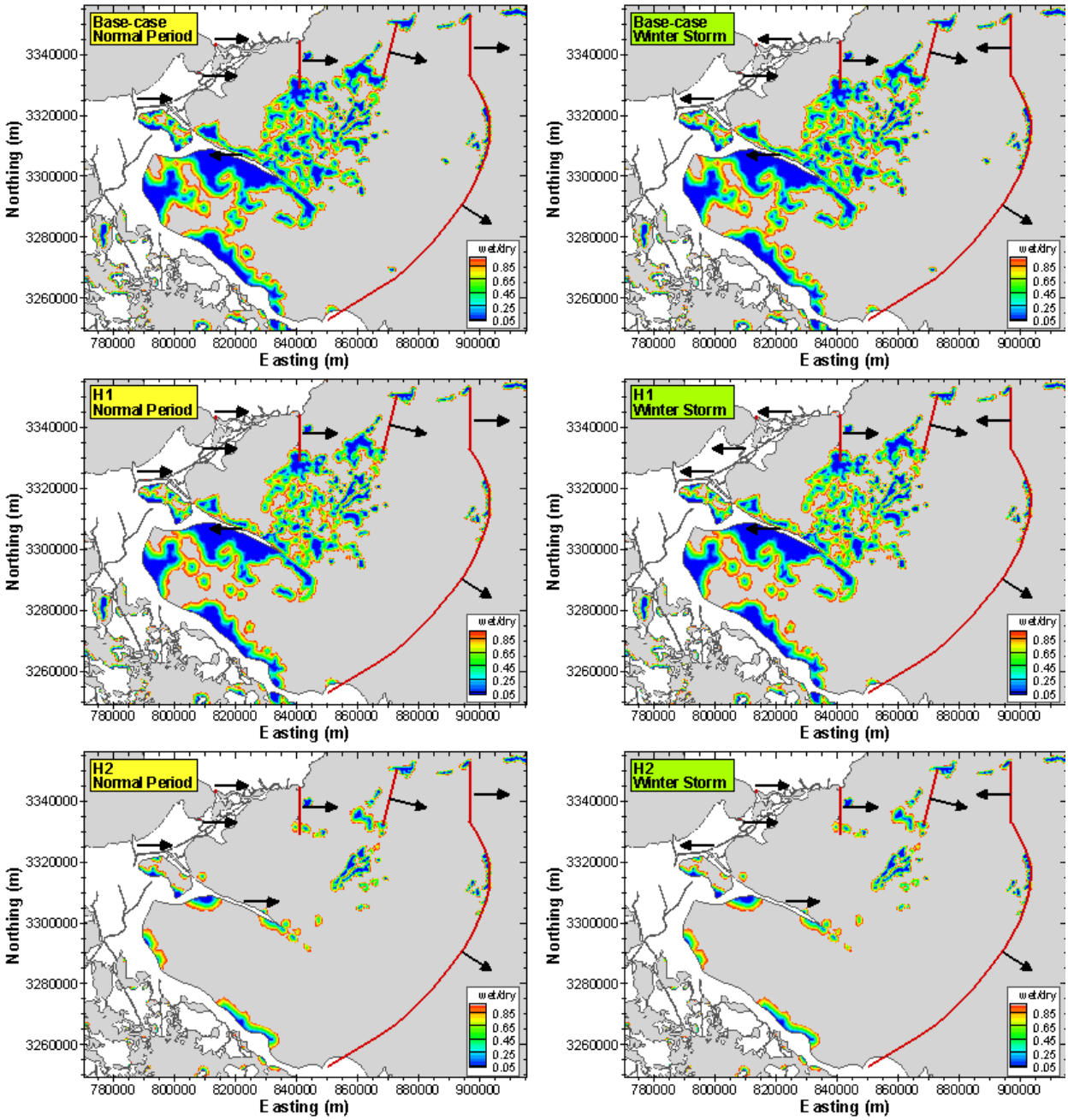

Figure 52 - Circulation patterns based on flow dominance specified in Table 6 and Table 7. The left panel shows circulation patterns for the normal period while the right panel shows winter storm circulation patterns. The base-case, H1, and H2 circulation patterns are shown in top, middle, and bottom panels, respectively. Contours show the wet/dry parameter for the base-case scenario (zero represents subaerial elements, gray represents water elements). An arrow to the right represents ebb-dominant flow conditions.

CHAPTER 6

Conclusions

Results show that the transformation from barrier islands to inner shoals does not cause a large increase in the tidal prism. This was expected since the bay area was only slightly increased by RSLR rates. Therefore, Hypothesis 1 is accepted; however, a small increase in tidal prism and tidal exchange was observed during winter storms. While differences in tides were typically less than 2.5 cm between the present-day and transgressive phase of barrier islands (present day and H1), the transgressive state of the barriers islands did produce variabilities in salinity. This indicates that tidal exchange and transport is heightened, despite the small increase in the tidal prism. In relation to tidal exchange, circulation patterns during normal conditions are identical. During winter storm conditions, only the Chef Menteur Pass changes flow dominance.

The largest difference in salinity between present day and future land-loss conditions occurred during winter storms. This research shows that the conversion from barrier islands to inner shoals would cause an increase in salinity ranging from 0.01 to 0.9 ppt. This increase, regardless of how small it may be, confirms that the barrier islands do provide protection from marine saltwater fluxes in the back-basins and perhaps aid in preserving salinity gradients across the islands. With barrier island transgression and subsequent disappearance, it is expected that the increased exchange between the coastal ocean and the estuary will facilitate the landward migration of marine conditions into the back-basins. Open water areas (the lower to middle basin) experienced the largest changes in salinity (0.08 to 0.9 ppt). Analysis at the back-barrier D2 location (Chandeleur Islands), for instance, indicates that as the barrier islands transgress, marine conditions migrate landward. There was an average 0.34 ppt increase in salinity at D2 once the barrier islands were converted to inner shoals. An even higher increase in salinity is expected when favorable winds (southeasterlies) are present. At interior locations throughout the estuary, the transport of a conservative quantity (i.e., salinity) is not significantly affected by barrier island transgression; the salinity increases by less than 0.06 ppt. It can therefore be concluded that the marsh acts as a barrier preventing mixing across the domain, thereby reducing the estuarine gradient.

Through this research, Hypothesis 2, which states that interior marsh degradation will cause an increase in tidal exchange and tidal prism, has also been accepted as true. The significant difference in tidal amplitude (0.4 cm to 4.6 cm) that occurs at interior locations such as NE Bay Gardene, the Rigolets, and Chef Menteur once the marsh has eroded and submerged proves that the conversion of marsh to open water increases both the tidal prism and tidal exchange within the estuary. Increases in tidal volume due to increased bay area, indicate a corresponding increase in tidal prism. Simulated salinity in the region is amplified by 0.09 to 2 ppt after marsh deterioration. This proves that the loss of interior wetlands and marshes greatly affects the hydrodynamics and resulting transport and exchange in this region.

The loss of wetlands as well as changes in the depth of bays and estuaries as a result of RSLR causes a change in circulation patterns within both the estuary and coastal ocean. This change in circulation is most evident during H2 conditions, where the basin is very dynamic and responsive to wind stress. These changes in circulation, along with the increase in transport capacity of what is now a more open inner shelf as a result of transgression, promote transport and diffusion of marine water into interior back-basins. Conversely, this large and open system will equally respond to flux from low salinity sources from other areas of the basin as a result of northerly and westerly wind stress.

Winter storms also influence the circulation in existing tidal channels. The presence of winter storms causes dynamic changes in wind direction, magnitude, and duration, thereby

affecting currents resulting from wind shear. Additionally, the passage of these storms causes a change in atmospheric pressure that has noticeable affects on water elevations in the vicinity of the front. These winter storms amplify the instantaneous flow across the entire estuary, increase tidal exchange, and at times cause changes in the current direction and dominance. This research shows that winter storms increase the amplitude and fluctuations in tidal elevation and resulting salinity, especially once interior wetlands have converted to open water. This increase in exchange due to the presence of winter storms is largely the result of 1) wind-induced currents that are no longer being dissipated through friction or redirected by land boundaries within the estuary, 2) currents produced by wind setup and setdown, and 3) currents produced by increased horizontal density gradients.

Future Recommendations

The author recommends that during future studies, initial salinity conditions are generated using spatially and temporally variant observed salinity data. This salinity data should coincide with the time period of simulation. These values should then be interpolated across the domain, instead of interpolating average annual or average seasonal salinity. This will produce calibration results that are more accurate and, as a result, salinity simulations that are more accurate. Additionally, assurances should be made to extract model salinity at the same depth as the observed salinity. By comparing surface salinity to bottom salinity an adjustment must be applied, which is a function of vertical density gradient and stratification. This will result in the loss of calibration accuracy. By applying an adjustment to salinity data, it is assumed that the salinity gradient is linear with depth. This is often not the case and could be a major reason for divergences between observed and simulated salinities in this study.

Tide simulations could be improved by ensuring that all tidal gauging stations and bathymetry are referenced to the same vertical datum. Without this standardization, calibration results become less accurate. Additionally, the most recent and accurate bathymetric data should be used if trying to replicate an existing system.

To ensure accurate tidal simulations, the author stresses the importance of including spatially and temporally variant meteorological conditions. Changes in barometric pressure greatly affect the water elevation, as illustrated in this study. This varying parameter is not readily available in FVCOM, and therefore a model that incorporates user-defined atmospheric pressures into calculations may be better suited for modeling these dynamic conditions. Spatially variant winds are recommended to replicate variable wind stresses throughout the domain.

Finally, for interest in salinity distribution and relative change between scenarios in the upper estuary, the model should be run for several months (about 5 or 6 months), in order to diffuse salinity into the upper estuary. This need is primarily due to the long retention times of this part of the estuary. The retention time in Lake Pontchartrain, for example, is approximately five months. This added simulation time is necessary if one is interested in simulating salinity changes in the upper estuary.

REFERENCES

Abadie, S. and Poirrier, M., 2000. Increased density of large Rangia clams in Lake Pontchartrain after the cessation of shell dredging. *Journal of Shellfish Research*, 19(1), p.481–485.

Allison, M.A. and Meselhe, E.A., 2010. The use of large water and sediment diversions in the lower Mississippi River (Louisiana) for coastal restoration. *Journal of Hydrology*, 387, pp.346-60.

Barras, J. *et al.*, 2003. *Historical and projected coastal Louisiana land changes: 1978-2050*. Open File Report 03-334. USGS.

Baumann, H.; Day, J.W. ; and Miller, C.A., 1984. Mississippi deltaic wetland survival: Sedimentation versus coastal submergence. *Science*, 224, pp.1093-95.

Blum, M.D. and Roberts, H.H., 2009. Drowning of the Mississippi Delta due to insufficient sediment supply and global sea-level rise. *Nature Geoscience Letters*, 2, pp.481-91.

Boyd, R. and Penland, S., 1981. Washover of Deltaic Barriers on the Louisiana Coast. *Gulf Coast Association of Geological Societies Transactions*, 31, p.243 – 248.

Burchard, H., 2002. *Applied Turbulence Modeling in Marine Waters*. Berlin: Springer.

Chen, C.; Cowles, G. ; and Beardsley, R.C., 2004. *An Unstructured Grid, Finite-Volume Coastal Ocean Model: FVCOM User Manual*. UMASS-Dartmouth Technical Report-04-0601. New Bedford, MA: University of Massachusetts, School of Marine Science and Technology.

Chen, C.; Liu, H. ; and Beardsley, R., 2003. An unstructured grid, finite-volume, three-dimensional, primitive equations ocean model: application to coastal ocean and estuaries. *Journal of Atmospheric and Oceanic Technology, America Meteorological Society*, 20, pp.159-86.

Coleman, J.M., 1988. Dynamic Changes and Processes in the Mississippi River Delta. *Geological Society of America Bulletin*, 100, p.999 – 1015.

D' Alpaos, A.; Lanzoni, S.; Maranti, M. ; and Rinaldo, A., 2010. On the tidal prism-channel area relations. *Journal of Geophysical Research*, 115, p.F01003.

Day, J.W.J. *et al.*, 2007. Restoration of the Mississippi Delta: Lessons from Hurricanes Katrina and Rita. *Science* , 315(5819), pp.1679 - 1684.

Day, J.W.J.; Britsch, L.D.; Hawes, S.R.; Shaffer, G.P.; Reed, D.J. ; and Cahoon, D., 2000. Pattern and process of land loss in the Mississippi Delta: A Spatial and temporal analysis of wetland habitat change. *Estuaries and Coasts* , 23(4), pp.425-38.

Emanuel, K., 2005. Increasing destructiveness of tropical cyclones over the past 30 years. *Nature*, 436, pp.686-88.

Fearnley, S.M.; Miner, M.D.; Kulp, M.; Bohling, C. ; and Penland, S., 2009. Hurricane impact and recovery shoreline change analysis of the Chandeleur Islands, Louisiana, USA: 1855 to 2005. *Geo-Marine Letters*, 29(6), pp.455-66.

Feng, Z. and Li, C., 2010. Cold-front-induced flushing of the Louisiana Bays. *Journal of Marine Systems*, 82(4), pp.252-64.

Feng, Z., 2009. *Hydrodynamic Response to Cold Fronts Along the Louisiana Coast*. Thesis. Louisiana State University and Agricultural and Mechanical College Department of Oceanography and Coastal Sciences.

FitzGerald, D.M.; Fenster, M.S.; Argow, B.A. ; and Buynevich, I.V., 2008. Coastal Impacts Due to Sea-Level Rise. *Annual Review of Earth and Planetary Sciences*, pp.604-47.

FitzGerald, D.M.; Kulp, M.A.; Huges, Z.; Georgiou, I.; Miner, M.D.; Penland, S. ; and Howes, N., 2007. Impacts of rising sea level to backbarrier wetlands, tidal inlets, and barrier islands: Barataria Coast, Louisiana. pp.1179-92.

Frazier, D.E., 1967. Recent Deltaic Deposits of the Mississippi River: Their Development and Chronology. *Gulf Coast Association of Geological Societies Transactions*, 17, p.287 – 315.

Frazier, D.E., 1967. Recent Deltaic Deposits of the Mississippi River: Their Development and Chronology. *Gulf Coast Association of Geological Societies Transactions*, 17, pp.287-315.

Georgiou, I. and McCorquodale, J., 2002. Stratification and circulation patterns in Lake Pontchartrain. In M.a.B.L. Spaulding, ed. *Estuarine and Coastal Modeling*. New York: ASCE. p.140–151.

Georgiou, I.Y. and Schindler, J.K., 2009. Wave Forecasting and Longshore Sediment Transport Gradients along a Transgressive Barrier Island: Chandeleur Islands, Louisiana. *Geo-Marine Letters*, 29(6), pp.467 - 476.

Georgiou, I.Y.; FitzGerald, D.M. ; and Stone, G.W., 2005. The Impact of Physical Processes along the Louisiana Coast. *Journal of Coastal Research*, SI(44), pp.72-89.

Georgiou, I.Y.; Kulp, M.A.; FitzGerald, D.M. ; and Miner, M., 2010. The Louisiana Coastline. In E. Bird, ed. *Coastlines of the World*. New York: Elsevier. p.12.

Georgiou, I.Y.; McCorquodale, J.A.; Neupani, J.; Howes, N.; Hughes, Z.; FitzGerald, D.M. ; and Schindler, J.K., 2010. *Modeling the Hydrodynamics of Diversion into Barataria Basin*. Final report submitted to the Lake Pontchartrain Basin Foundation. New Orleans, LA: Pontchartrain Institute for Environmental Sciences, University of New Orleans.

Georgiou, I.Y.; McCorquodale, J.A.; Schindler, J.; Retana, A.G.; FitzGerald, D.M.; Hughes, Z. ; and Howes, N., 2009. Impact of Multiple Freshwater Diversions on the Salinity Distribution in the Pontchartrain Estuary under Tidal Forcing. *Journal of Coastal Research*, 54(SI), pp.59-70.

Goldenberg, S.B.; Landsea, C.W.; Mestas-Nuñez, A.M. ; and Gray, W.M., 2001. The Recent Increase in Atlantic Hurricane Activity: Causes and Implications. *Science*, 293, pp.474-79.

Haralampides, K., 2000. *A study of the hydrodynamics and salinity regimes of the Lake Pontchartrain system*. Ph.D. Dissertation. Dept. of Civil and Environmental Engineering, University of New Orleans: New Orleans, LA.

Hart, W. and Murray, S., 1978. Energy Balance and Wind Effects in a Shallow Sound. *Journal of Geophysical Research*, 83(C8), pp.4097-106.

Horowitz, A.J.; Kelrick, K.A. ; and Smith, J.J., 2001. Estimating suspended sediment and trace element fluxes in the Mississippi, Columbia, Colorado and Rio Grande drainage basins. *Hydrological Processes*, 15, p.1169–1207.

Horowitz, A.J., 2006. The effects of the "Great Flood of 1993" on subsequent suspended sediment concentrations and fluxes in the Mississippi River Basin, USA. In *Sediment Dynamics and the Hydromorphology of Fluvial Systems, International Association of Hydrological Sciences Publication 306*. Dundee, UK, 2006. IAHS Publ.

Horowitz, J., 2010. A quarter century of declining suspended sediment fluxes in the Mississippi River and the effect of the 1993 flood. *Hydrological Processes*, 24, pp.13-34.

Howes, N.C.; FitzGerald, D.M.; Hughes, Z.J.; Georgiou, I.Y. ; and Kulp, M.A., 2010. Hurricane-induced failure of low salinity wetlands. *Proceedings of the National Academy of Sciences*, 107(32), pp.14014-14019.

Hughes, S.A., 2002. Equilibrium Cross Sectional Area at Tidal Inlets. *Journal of Coastal Research*, 18(1), pp.160-74.

International Panel on Climate Change, 2007. *Climate change 2007: the physical science basis, summary for policymakers*. Group I Fourth Assessment Report of the Intergovernmental Panel on Climate Change. Cambridge, UK.

Jarrett, J.T., 1976. *Tidal prism-inlet area relationships, General Investigation of Tidal Inlets Report 3*. Final Report. Fort Belvoir, VA: U.S. Army Coastal Engineering Research Center.

Jin, K.-R.; Hamrick, J.H. ; and Tisdale, T., 2000. Application of Three-Dimensional Hydrodynamic Model for Lake Okeechobee. *Journal of Hydraulic Engineering*, 126(10), pp.758-71.

Keen, T.R.; Stone, G.; Kaihatu, J. ; and Hsu, Y.L., 2003. Barrier Island Erosion during a Winter Cold Front in Mississippi Sound. pp.1-13.

Keen, T.R., 2002. Waves and Currents during a Winter Cold Front in the Mississippi Bight, Gulf of Mexico. *Journal of Coastal Research*, 18(4), pp.622-36.

Keown, M.P.; Dardeau, E.A..J. ; and Causey, E.M., 1986. Historic trends in the sediment flow regime of the Mississippi River. *Water Resources Research*, 22, p.1555–1564.

Kindinger, J., 1988. Seismic stratigraphy of the Mississippi-Alabama shelf and upper continental slope. *Marine Geology*, 83(1), pp.79-94.

Lake Pontchartrain Basin Foundation, 2006. *Comprehensive Habitat Management Plan for the Lake Pontchartrain Basin*. [Online] Lake Pontchartrain Basin Foundation (Final) Available at: http://www.saveourlake.org/PDF-documents/CHMP_final_%2022706.pdf [Accessed 12 October 2010].

Lavoie, D.; Miner, M.; Georgiou, I.Y.; Fearnley, S.; Sallenger, A.H.J.; Williams, S.J.; Twichell, D.; Flocks, J. ; and Kulp, M., 2009. Chapter I. Summary and discussion. In D. Lavoie, ed. *Sand resources, regional geology, and coastal processes of the Chandeleur Islands coastal system - an evaluation of the Breton National Wildlife Refuge: U.S. Geological Survey Scientific Investigations Report 2009–5252*. pp.169-80.

Li, C.; Walker, N.; Hou, A.; Georgiou, I.; Roberts, H.H.; Laws, E.; McCorquodale, J.A.; Weeks, E.; Li, X. ; and Crochet, J., 2008. Circular plumes in Lake Pontchartrain Estuary under wind straining. *Estuarine, Coastal and Shelf Sciences*, 80, pp.161-72.

Marchi, E., 1990. Sulla stabilitá delle bocche lagunari a marea. *Rendiconti Lincei*, 1(2), pp.137-50.

Marmar, H.A., 1954. Tides and sea level in the Gulf of Mexico. In P.S. Galtsoff, ed. *Gulf of Mexico, Its Origins, Waters, and Marine Life: Fishery Bulletin 89*. U.S. Fish and Wildlife Service. pp.101-18.

Meade, R.H. and Moody, J.A., 2008. Changes in the discharge of sediment through the Missouri–Mississippi River system, 1940–2007. In *Proceeding of the VIII National Meeting of Sedimentary Engineers*. Brazilian Association of Sedimentary Engineers, Campo Grande,Brazil, 2–8 December, 2008.

Mellor, G. and Yamada, T., 1982. Development of a turbulence closure model for geophysical fluid problems. *Reviews of Geophysics*, 20, pp.851-75.

Milliman, J.D. and Syvitski, J.P.M., 1992. Geomorphic/tectonic control of sediment discharge to the ocean: The importance of small mountainous rivers. *The Journal of Geology*, 100, p.525–544.

Miner, M.; Kulp, M.; FitzGerald, D.; Flocks, J. ; and Weathers, H.D., 2009. Delta lobe degradation and hurricane impacts governing large-scale coastal behavior, South-central Louisiana, USA. *Geo-Marine Letters*, 29(6), pp. 441-453.

Morton, R.A.; Bernier, J.C.; Barras, J.A. ; and Ferina, N.F., 2005. *Rapid Subsidence and Historical Wetland Loss in the South-Central Mississippi Delta Plain: Likely Causes and Future Implications*. Open-file Report 2005-1216. U.S. Geological Survey.

O'Brien, M.P., 1969. Equilibrium flow areas of inlets in sandy coasts. *Journal of the Waterways, Harbors and Coastal Engineering Division ASCE*, 95, pp.43-52.

Penland, S.; Boyd, R. ; and Suter, J.R., 1988. Transgressive Depositional Systems of the Mississippi Delta Plain: A Model for Barrier Shoreline and Shelf Sand Development. *Journal of Sedimentary Petrology*, 58(6), pp.932-49.

Penland, S.; Connor, P.J.; Beall, A.; Fearnley, S. ; and Williams, S., 2005. Changes in Louisiana's Shoreline: 1855-2002. *Journal of Coastal Research*, 44(SI), pp.7-39.

Reed, D.J. and Cahoon, D.R., 1993. Marsh submergence vs. marsh accretion: Interpreting accretion deficit data in coastal Louisiana. In Magoon, 0.T.; Wilson, W.S.; Converse, H. ;and Tobin, L.T., eds. *Coastal Zone '93: Proceedings of the Eighth Symposium on Coastal and Ocean Management*. New York, 1993. American Society of Civil Engineers.

Reed, D.J.; de Luca, N. ; and Foote, A.L., 1997. Effect of Hydrologic Management on Marsh Surface Sediment Deposition in Coastal Louisiana. *Estuaries*, 20, pp.301-11.

Reyes, E.; Georgiou, I.; Reed, D. ; and McCorquodale, A., 2005. Using Models to Evaluate the Effects of Barrier Islands on Estuarine Hydrodynamics and Habitats: A Numerical Experiment. *Journal of Coastal Research*, 44(SI), pp.176-85.

Ritchie, W. and Penland, S., 1985. Overwash Process-Response Characteristics of the Caminada-Moreau Barrier Shoreline, Louisiana. In S. Penland and R. Boyd, eds. *Transgressive Depositional Environments of the Mississippi River Delta Plain: A Guide to the Barrier Islands, Shoals, and Beaches in Louisiana, Louisiana State Geological Survey Guidebook Series, no. 3*. Baton Rouge, Louisiana: Louisiana Geological Survey. pp.141-74.

Ritchie, W. and Penland, S., 1988. Rapid dune changes associated with overwash processes on the deltaic coast of South Louisiana. *Marine Geology*, 81, pp.97-122.

Roberts, H.H., 1997. Dynamic Changes of the Holocene Mississippi River Delta Plain: The Delta Cycle. *Journal of Coastal Research*, 13(3), pp.605-27.

Rosati, J. and Stone, G., 2009. Geomorphologic Evolution of Barrier Islands along the Northern U.S. Gulf of Mexico and Implications for Engineering Design in Barrier Restoration. *Journal of Coastal Research*, 25(1), pp.8-22.

Sallenger, A.H.; Wright, C.W.; Howd, P.; Doran, K. ; and Guy, K., 2009. Chapter B. Extreme Coastal Changes on the Chandeleur Islands, Louisiana, during and after Hurricane Katrina. *in Lavoie, D., ed., Sand resources, regional geology, and coastal processes of the Chandeleur Islands coastal system—an evaluation of the Breton National Wildlife Refuge: U.S. Geological Survey Scientific Investigations Report 2009–5252*, pp.27-36.

Shroeder, W.W.; Dinnel, S.P. ; and Wiseman, W.J..J., 1990. Salinity Stratification in a River-Dominated Estuary. *Estuaries*, 13(2), pp.145-54.

Signell, R.P. and List, J.H., 1997. Modeling Waves and Circulation in Lake Pontchartrain. *Gulf Coast Association of Geological Societies Transactions*, 47, pp.529-32.

Soulsby, R., 1997. *Dynamics of Marine Sands*. London: Thomas Telford Publications.

Stone, G.W. and McBride, R.A., 1998. Louisiana Barrier Islands and Their Importance in Wetland Protection: Forecasting Shoreline Change and Subsequent Response of Wave Climate. *Journal of Coastal Research*, 14(3), pp.900-15.

Stone, G.W.; Liu, B.; Pepper, D.A. ; and Wang, P., 2004. The importance of extratropical and tropical cyclones on the short-term evolution of barrier islands along the northern Gulf of Mexico, USA. *Marine Geology* , 210 , p.63–78.

Stone, G.; Zhang, X. ; and Sheremet, A., 2005. The Role of Barrier Islands, Muddy Shelf and Reefs in Mitigating. *Journal of Coastal Research*, 44(SI), pp.72-89.

Taylor, G.I., 1920. Tidal Friction in the Irish Sea. *Philosophical Transactions of the Royal Society of London. Series A, Containing Papers*, 220, pp.1-33.

Thorne, C.; Harmar, O.; Watson, C.; Clifford, N.; Biedenharn, D. ; and Measures, R., 2008. *Current and Historical Loads in the Lower Mississippi River*. Final Report to the U.S. Army, Contract Number 1106-EN-01. Nottingham,UK: University of Nottingham, University Park School of Geography.

Törnqvist, T.E.; Bick, S.J.; van der Borg, K. ; and de Jong, A.F.M., 2006. How Stable is the Mississippi Delta? *Geology*, 34(8), pp.697-700.

Twichell, D.; Pendleton, E.; Baldwin, W. ; and Flocks, J., 2009. Subsurface control on seafloor erosional processes offshore of the Chandeleur Islands, Louisiana. *Geo-Marine Letters*, 29(6), pp.349-58.

U.S. Army Corps of Engineers New Orleans District, 1982. *Lake Pontchartrain, Louisiana and vicinity Hurricane Protection Project*. Environmental Impact Statemen. New Orleans, LA: US Army Corps of Engineers.

van Heerden, I.L. and DeRouen, K.J., 1997. Implementing a Barrier Island and Barrier Shoreline Restoration Program: The State of Louisiana's Perspective. *Journal of Coastal Research*, 13(3), pp.679-85.

Yuill, B.; Lavoie, D. ; and Reed, D., 2009. Understanding Subsidence Processes in Coastal Louisiana. *Journal of Coastal Research*, SI 54, p.23–36.

APPENDICES

Appendix A: Domain Maps

Domain Mesh

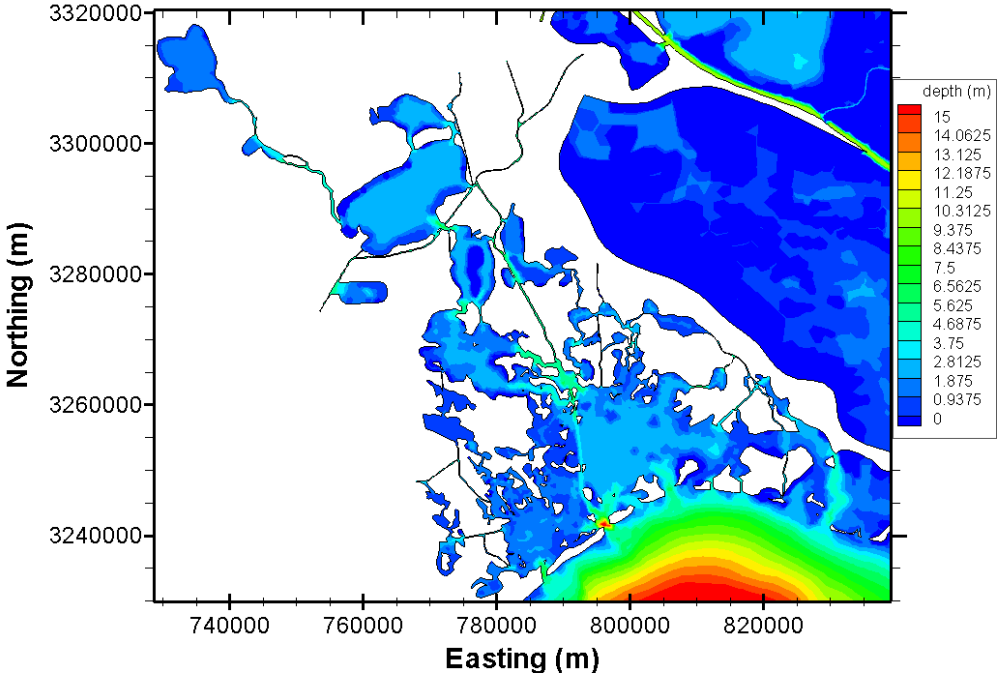

Figure 53 – Bathymetric contours of the Barataria Basin and Mississippi River delta. (UTM 15 coordinates and bathymetries in meters)

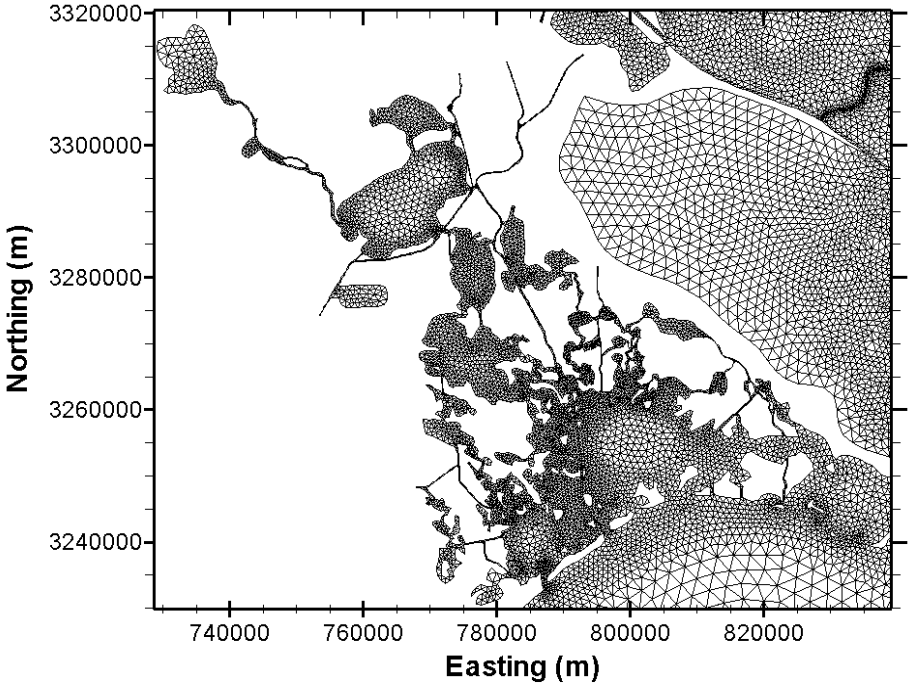

Figure 54 – Mesh of the Barataria Basin and Mississippi River delta (UTM 15 coordinates in meters).

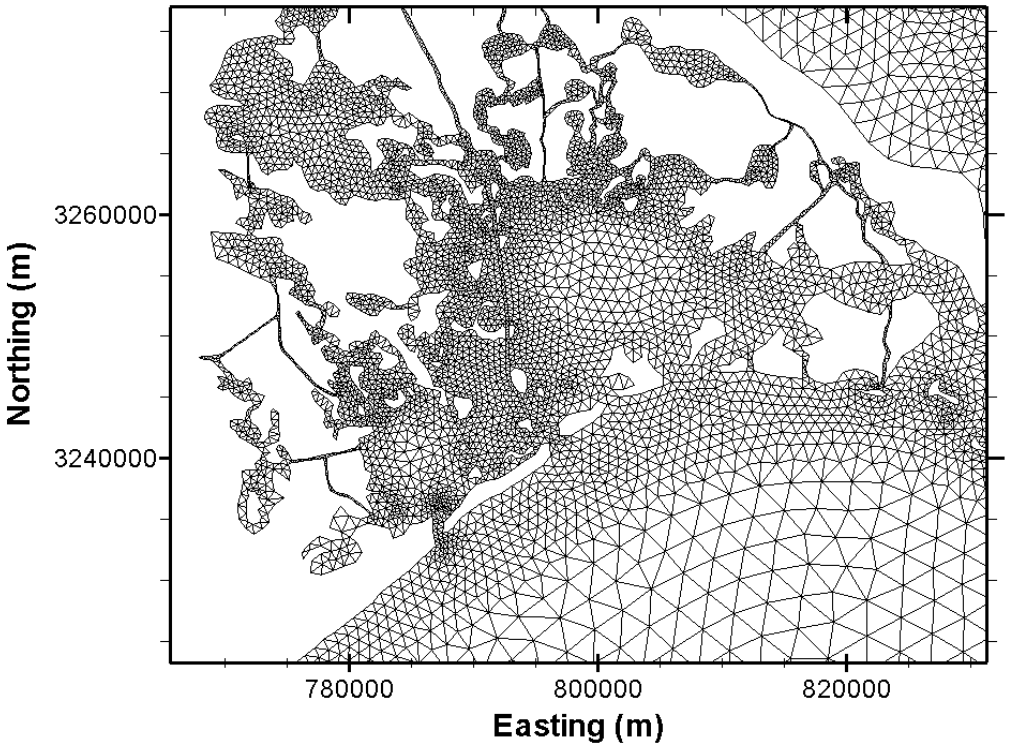

Figure 55– Detailed view of the Barataria Basin mesh. (UTM 15 coordinates in meters)

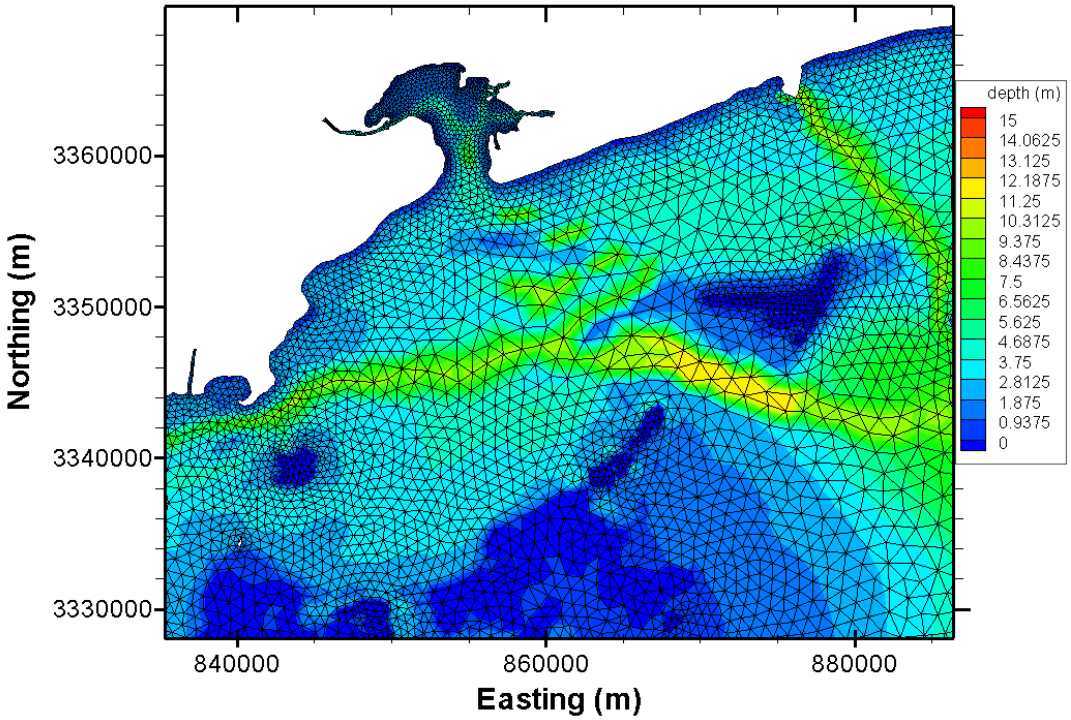

Figure 56– Detailed view of the Bay St. Louis mesh and bathymetric contours. (UTM 15 coordinates and bathymetries in meters)

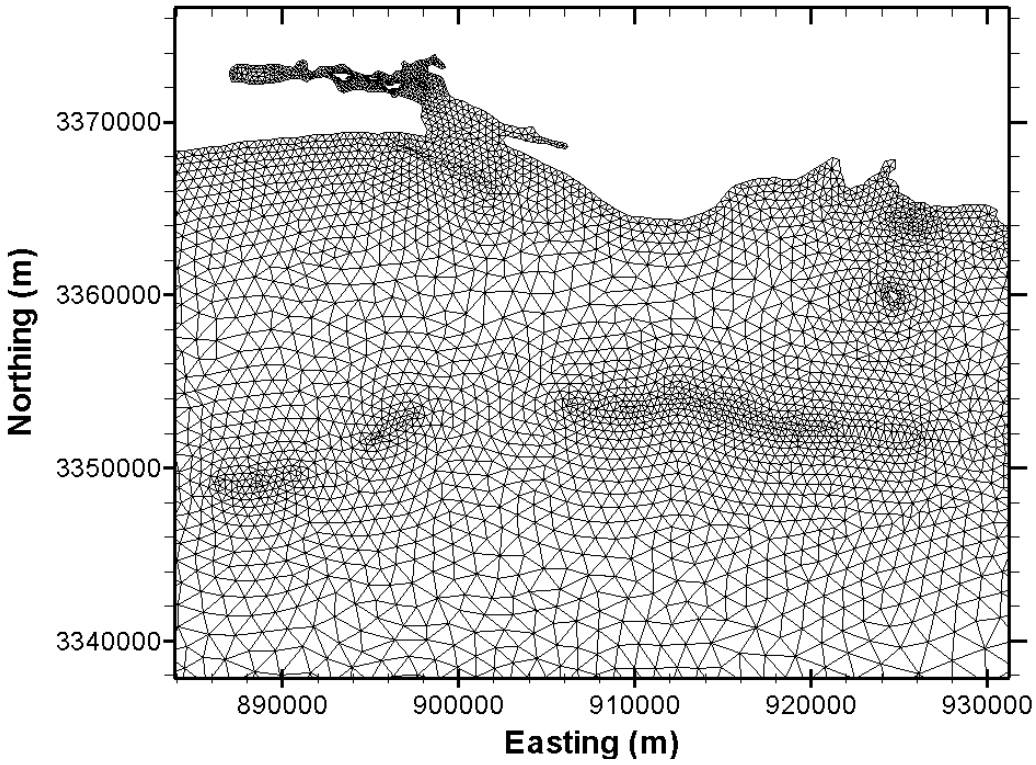

Figure 57 – Mesh of Biloxi Bay including Ship Island and Horn Island. (UTM 15 coordinates in meters)

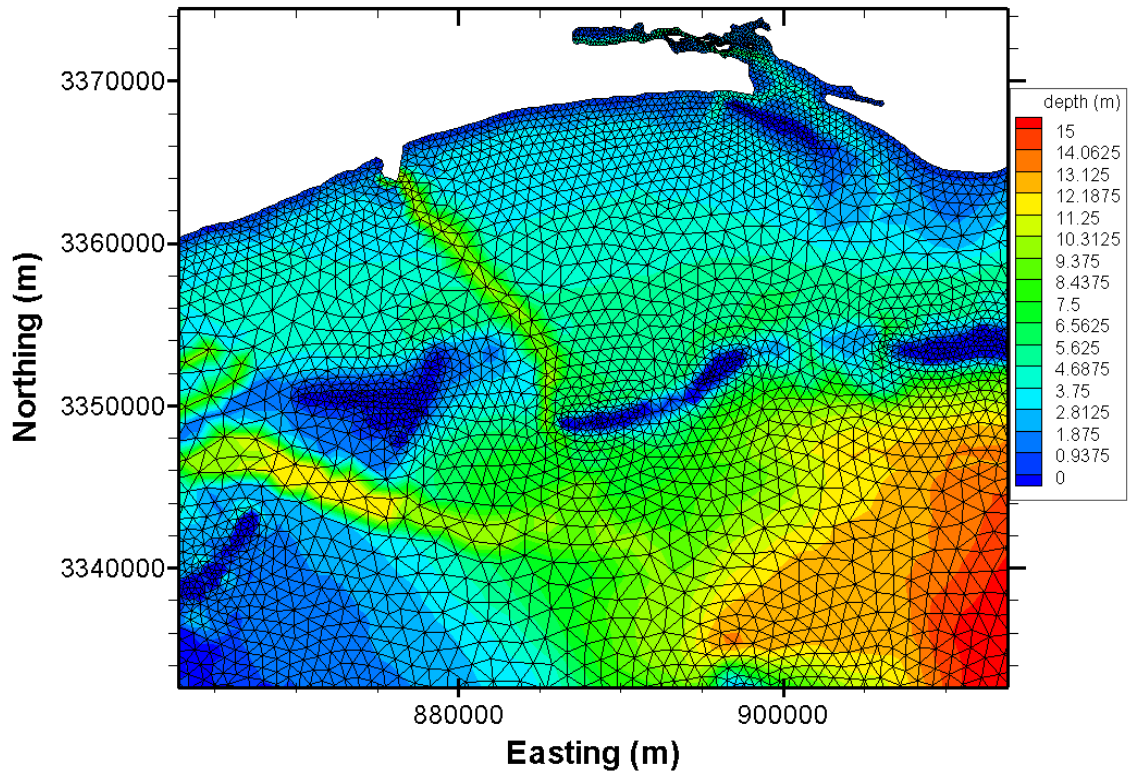

Figure 58 – Mesh of the Mississippi Sound including Biloxi Bay, Cat Island, Ship Island, and Horn Island. (UTM 15 coordinates in meters)

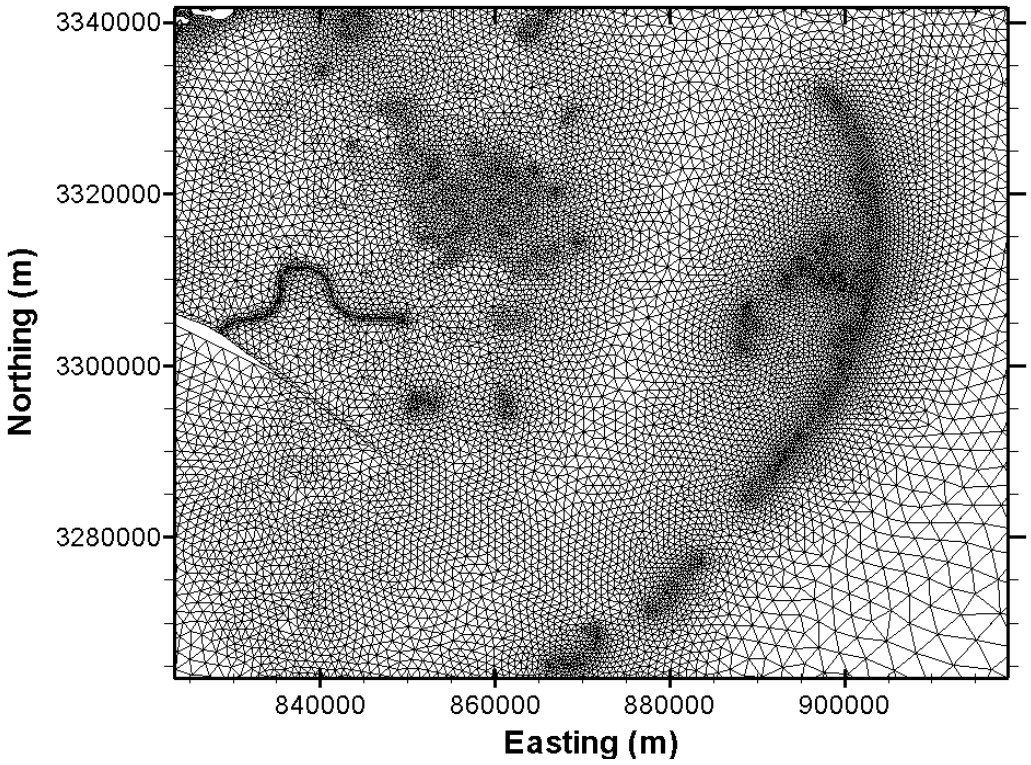

Figure 59 - Detailed view of the Chandeleur and Breton Sound mesh including the Chandeleur Islands, Biloxi Marsh, Bayou La Loutre, and Breton Island. (UTM 15 coordinates in meters)

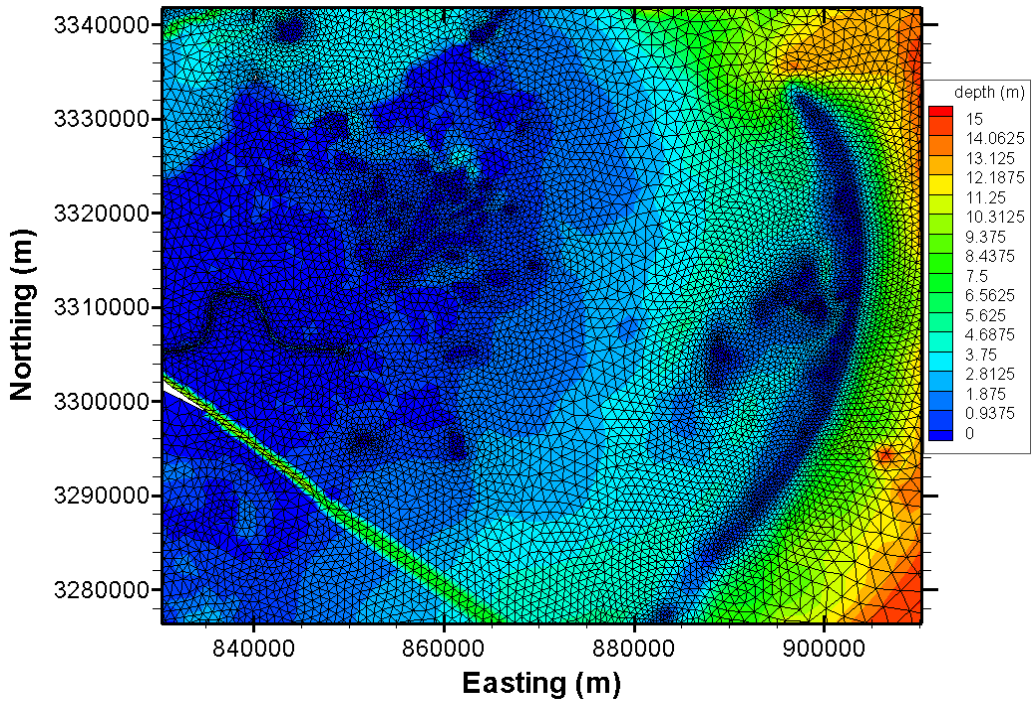

Figure 60- Detailed view of the Chandeleur and Breton Sound mesh, including the Chandeleur Islands, Biloxi Marsh, Bayou La Loutre, and Breton Island, with bathymetric contours. (UTM 15 coordinates and bathymetries in meters)

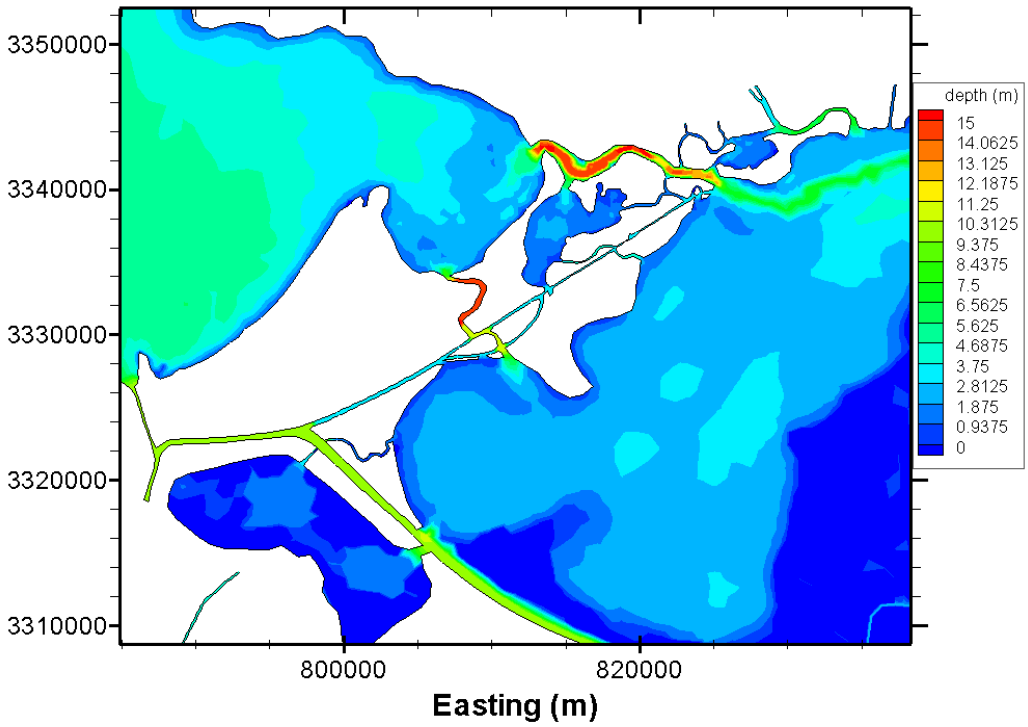

Figure 61– Bathymetric contours of the eastern Pontchartrain Estuary including Lake Pontchartrain, Lake Borgne, and major channels such as the Rigolets, IHNC, ICWW, and MRGO. (UTM 15 coordinates and bathymetries in meters)

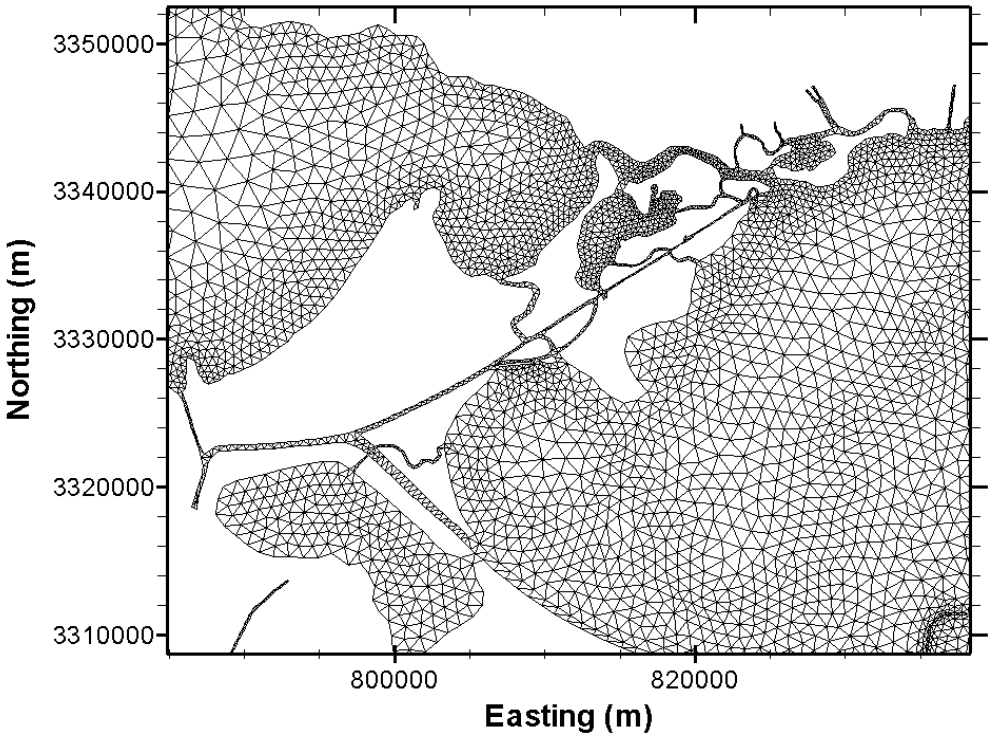

Figure 62 – Mesh of the eastern Pontchartrain Estuary including Lake Pontchartrain, Lake Borgne, and major channels such as the Rigolets, IHNC, ICWW, and MRGO. (UTM 15 coordinates and bathymetries in meters)

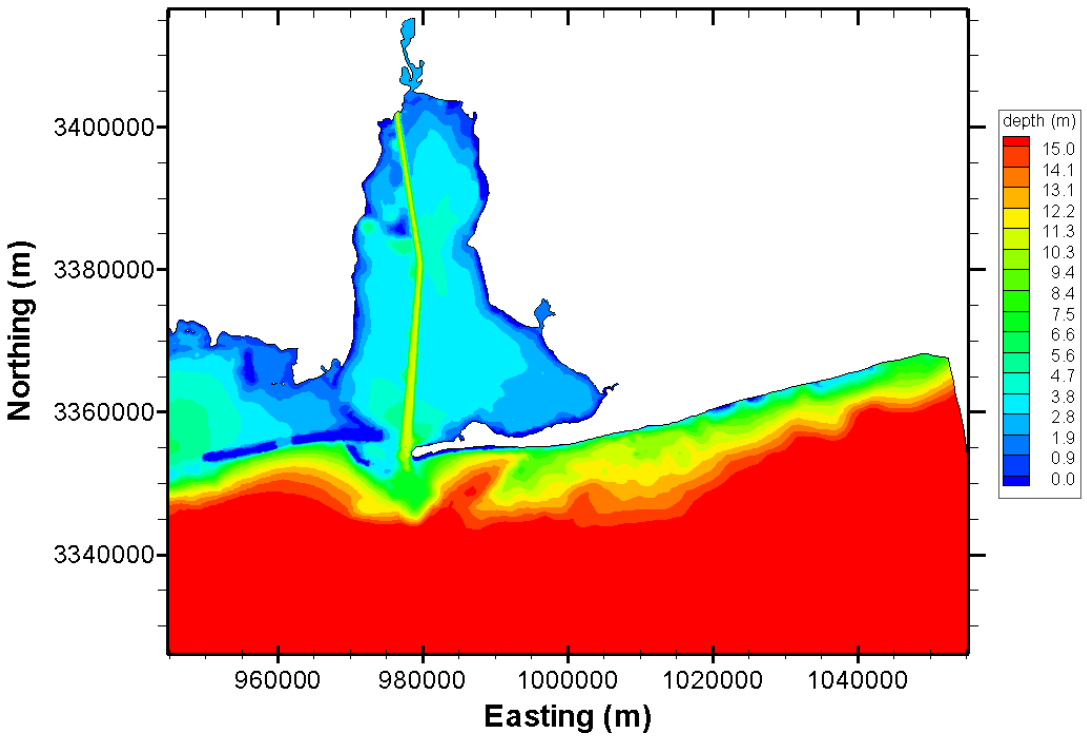

Figure 63 – Bathymetric contours of the Mobile Bay including Dauphin Island and the Mobile Bay Ship Channel. (UTM 15 coordinates and bathymetries in meters)

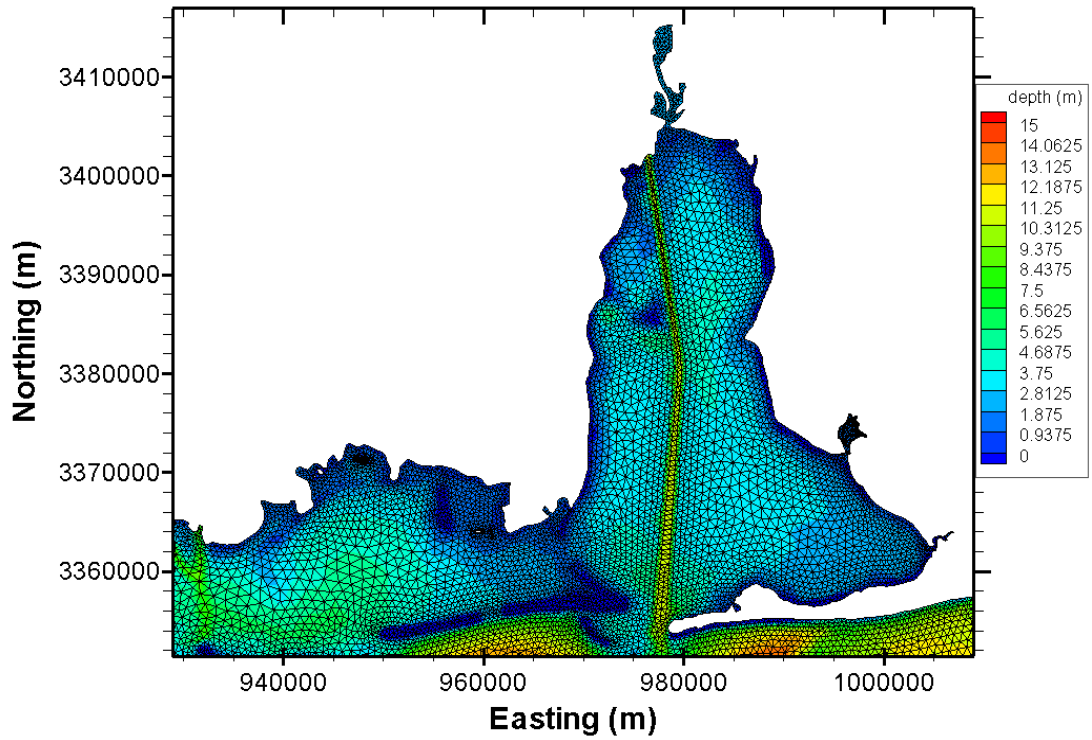

Figure 64– Detailed view of the mesh and bathymetric contours of the Mobile Bay including Dauphin Island and the Mobile Bay Ship Channel. (UTM 15 coordinates and bathymetries in meters)

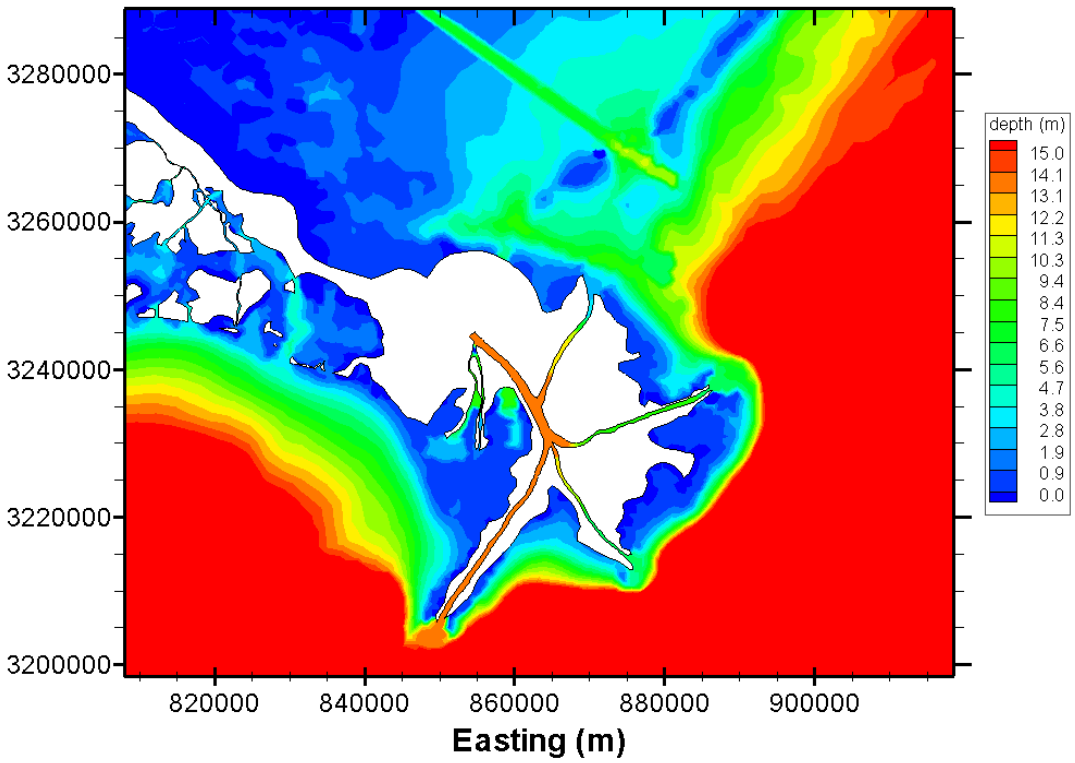

Figure 65 – Bathymetric contours of the Mississippi River Delta. (UTM 15 coordinates and bathymetries in meters)

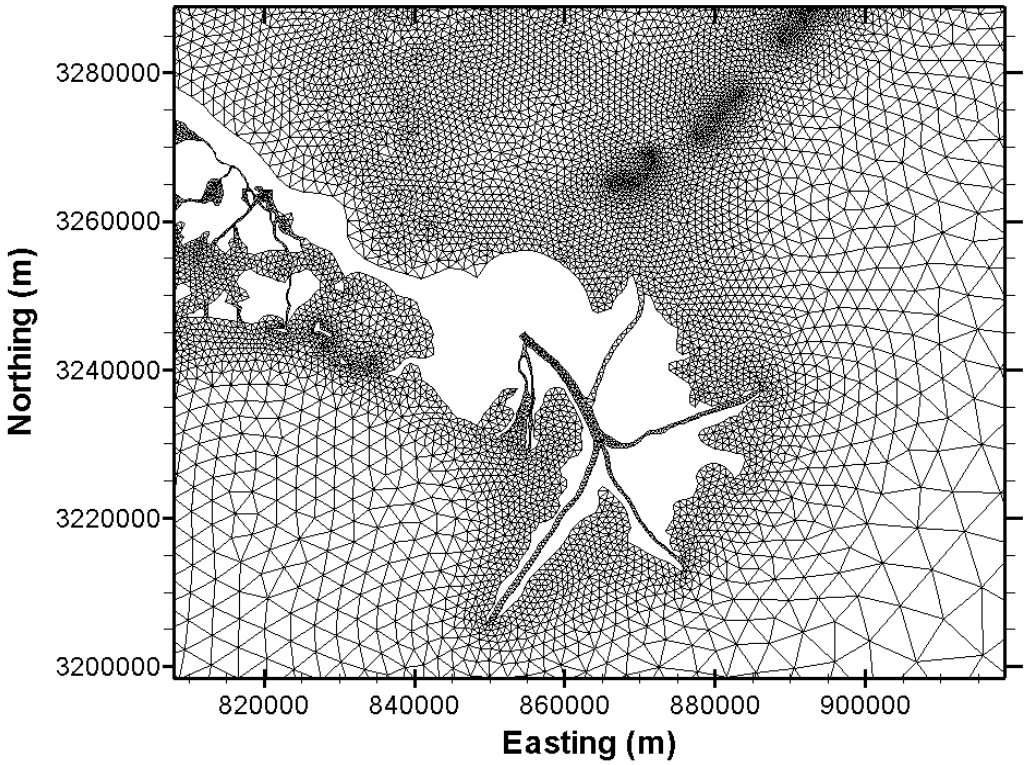

Figure 66 – Mesh of the Mississippi River Delta. (UTM 15 coordinates in meters)

Appendix B: Calibration Plots

Tidal Calibration

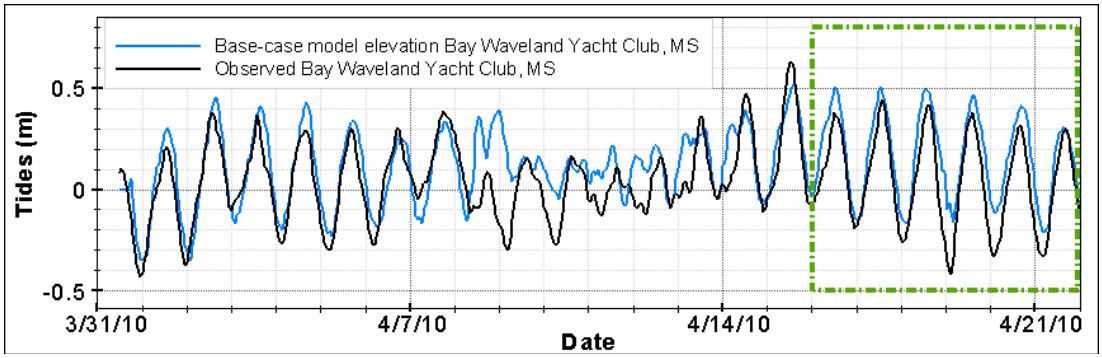

Figure 67 - Comparison of base-case scenario tides (meters) and observed tide data for the calibration period (3/31/10 to 4/22/2010). Calibration efforts focused on good correlation during the period of 4/16/10 to 4/22/10 at the Bay Waveland Yacht Club station. An adjustment was applied to observed data to account for vertical datum differences.

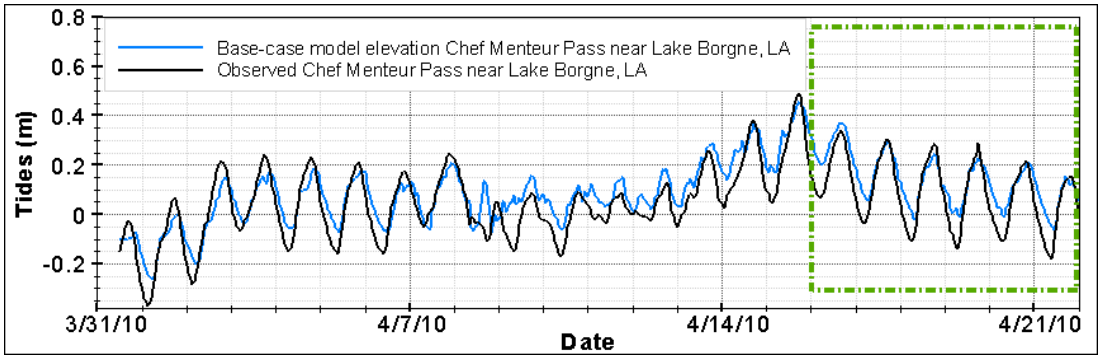

Figure 68 - Comparison of base-case scenario tides (meters) and observed tide data for the calibration period (3/31/10 to 4/22/2010). Calibration efforts focused on good correlation during the period of 4/16/10 to 4/22/10 at the Chef Menteur Pass near Lake Borgne station. An adjustment was applied to observed data to account for vertical datum differences.

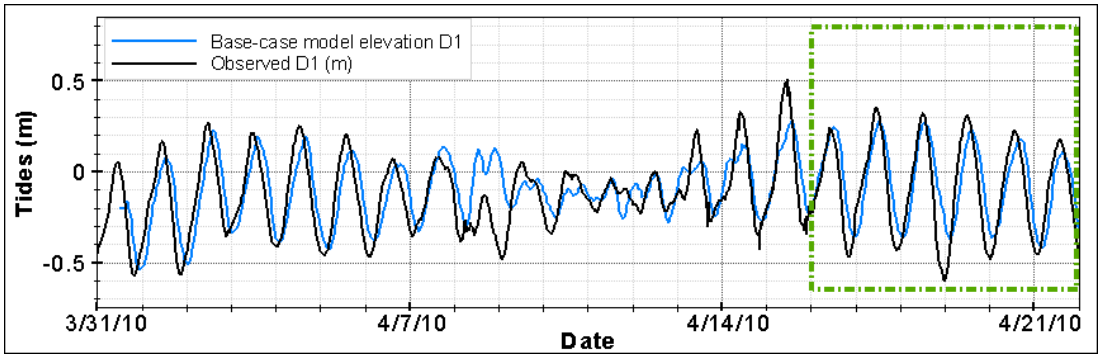

Figure 69 - Comparison of base-case scenario tides (meters) and observed tide data for the calibration period (3/31/10 to 4/22/2010). Calibration efforts focused on good correlation during the period of 4/16/10 to 4/22/10 at the D1 location. An adjustment was applied to observed data to account for vertical datum differences.

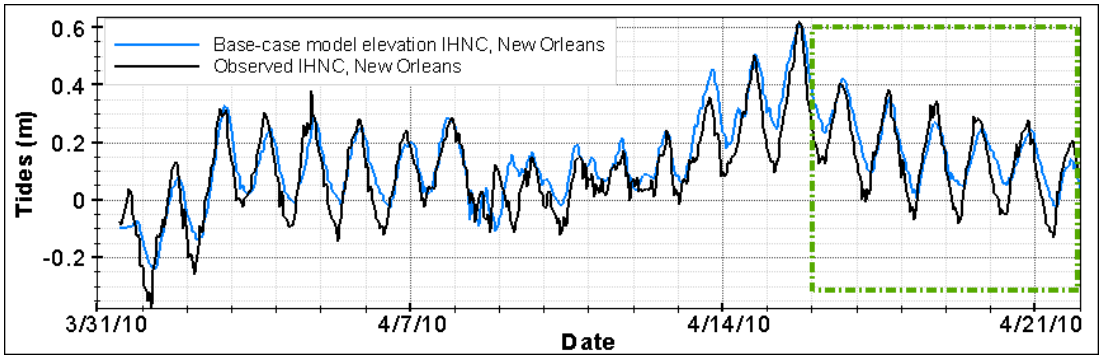

Figure 70 - Comparison of base-case scenario tides (meters) and observed tide data for the calibration period (3/31/10 to 4/22/2010). Calibration efforts focused on good correlation during the period of 4/16/10 to 4/22/10 at the IHNC, New Orleans station. An adjustment was applied to observed data to account for vertical datum differences.

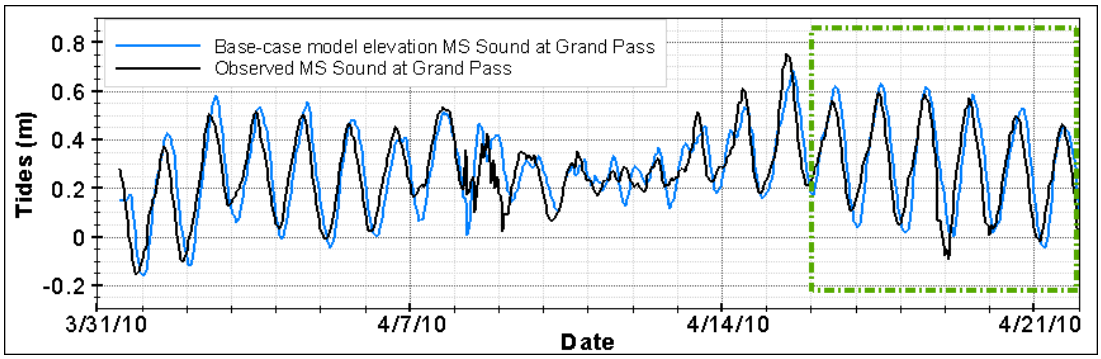

Figure 71 - Comparison of base-case scenario tides (meters) and observed tide data for the calibration period (3/31/10 to 4/22/2010). Calibration efforts focused on good correlation during the period of 4/16/10 to 4/22/10 at the Mississippi Sound at Grand Pass station. An adjustment was applied to observed data to account for vertical datum differences.

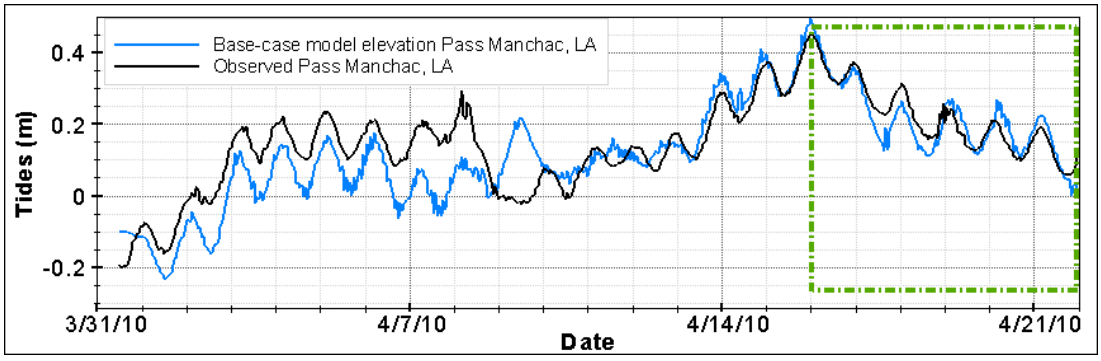

Figure 72 - Comparison of base-case scenario tides (meters) and observed tide data for the calibration period (3/31/10 to 4/22/2010). Calibration efforts focused on good correlation during the period of 4/16/10 to 4/22/10 at the Pass Manchac station. An adjustment was applied to observed data to account for vertical datum differences.

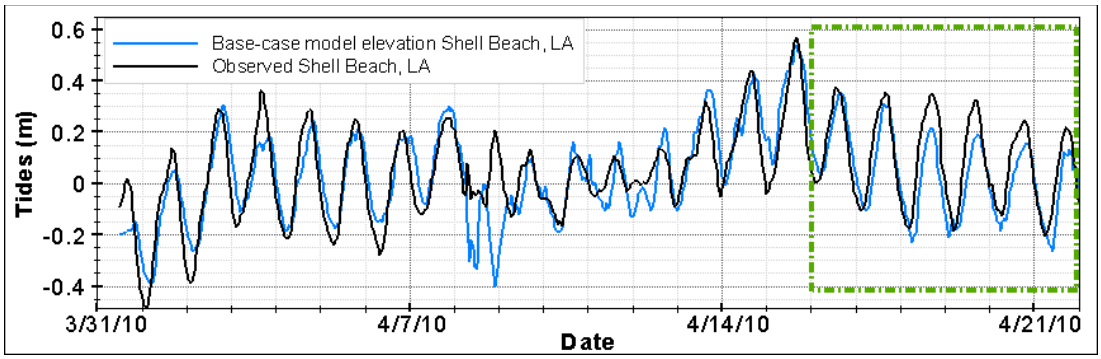

Figure 73 - Comparison of base-case scenario tides (meters) and observed tide data for the calibration period (3/31/10 to 4/22/2010). Calibration efforts focused on good correlation during the period of 4/16/10 to 4/22/10 at the Shell Beach, Louisiana, station. An adjustment was applied to observed data to account for vertical datum differences.

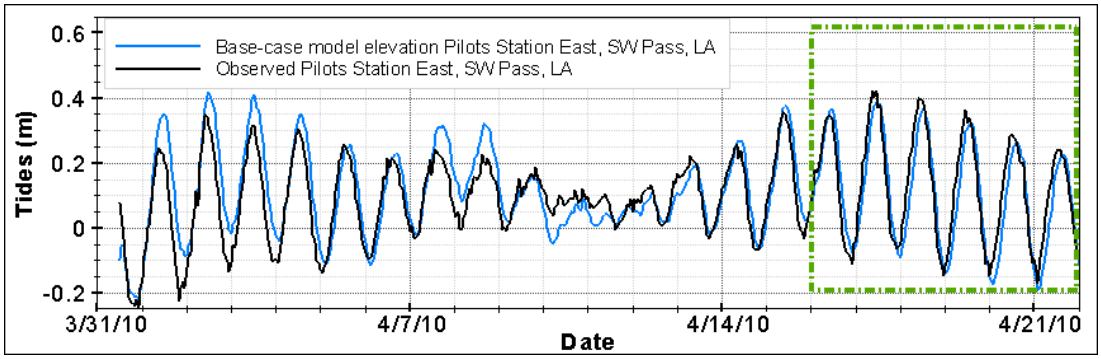

Figure 74 - Comparison of base-case scenario tides (meters) and observed tide data for the calibration period (3/31/10 to 4/22/2010). Calibration efforts focused on good correlation during the period of 4/16/10 to 4/22/10 at the Pilots Station East, SW Pass, Louisiana, station. An adjustment was applied to observed data to account for vertical datum differences.

Salinity Calibration

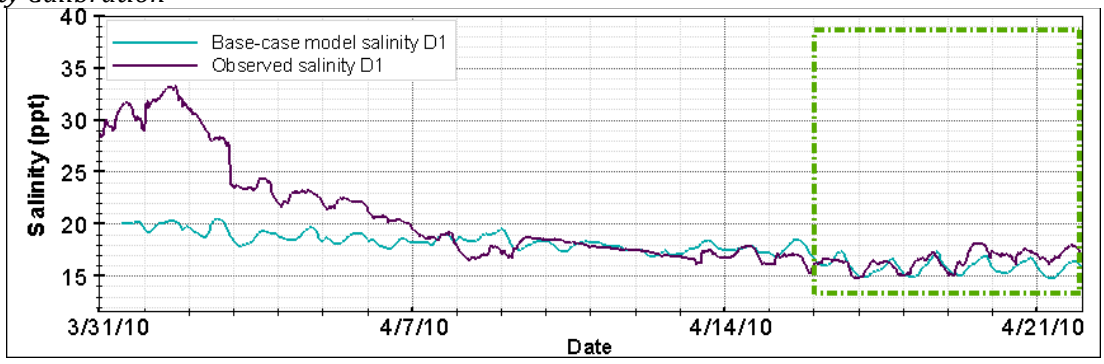

Figure 75 - Comparison of base-case scenario salinities (ppt) and observed salinity data for the calibration period (3/31/10 to 4/22/2010). Calibration efforts focused on good correlation during the period of 4/16/10 to 4/22/10 at the D1 station. An adjustment was applied to observed data to account for sensor height differences.

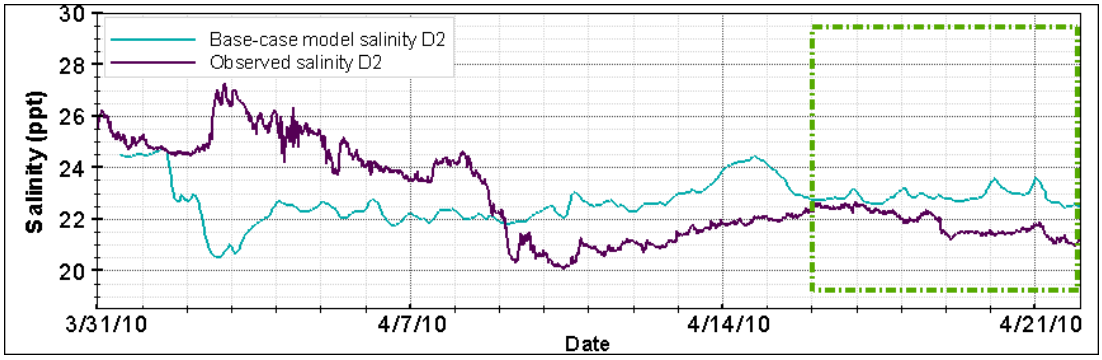

Figure 76 - Comparison of base-case scenario salinities (ppt) and observed salinity data for the calibration period (3/31/10 to 4/22/2010). Calibration efforts focused on good correlation during the period of 4/16/10 to 4/22/10 at the D2 station. An adjustment was applied to observed data to account for sensor height differences.

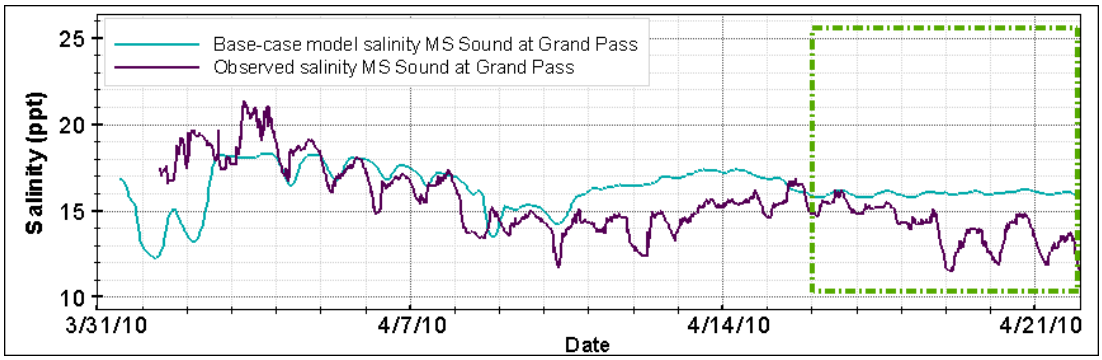

Figure 77 - Comparison of base-case scenario salinities (ppt) and observed salinity data for the calibration period (3/31/10 to 4/22/2010). Calibration efforts focused on good correlation during the period of 4/16/10 to 4/22/10 at the Mississippi Sound at Grand Pass station. An adjustment was applied to observed data to account for sensor height differences.

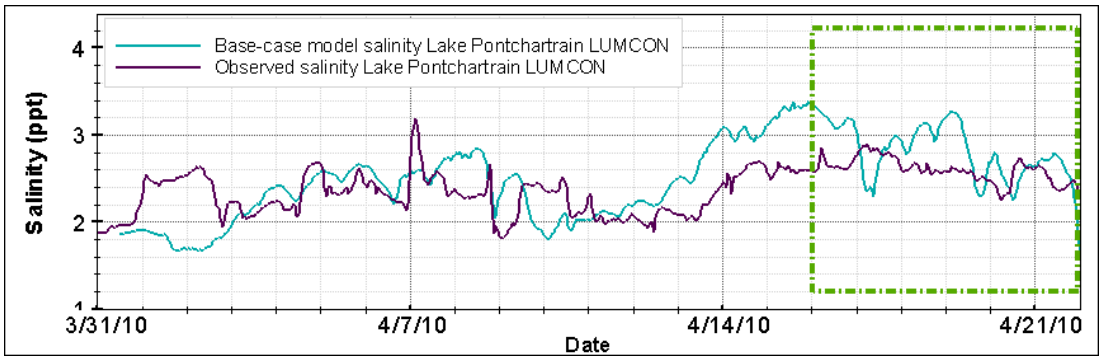

Figure 78 - Comparison of base-case scenario salinities (ppt) and observed salinity data for the calibration period (3/31/10 to 4/22/2010). Calibration efforts focused on good correlation during the period of 4/16/10 to 4/22/10 at the Lake Pontchartrain LUMCON station. An adjustment was applied to observed data to account for sensor height differences.

Appendix C: Simulation Result Plots

Tidal Simulation Results

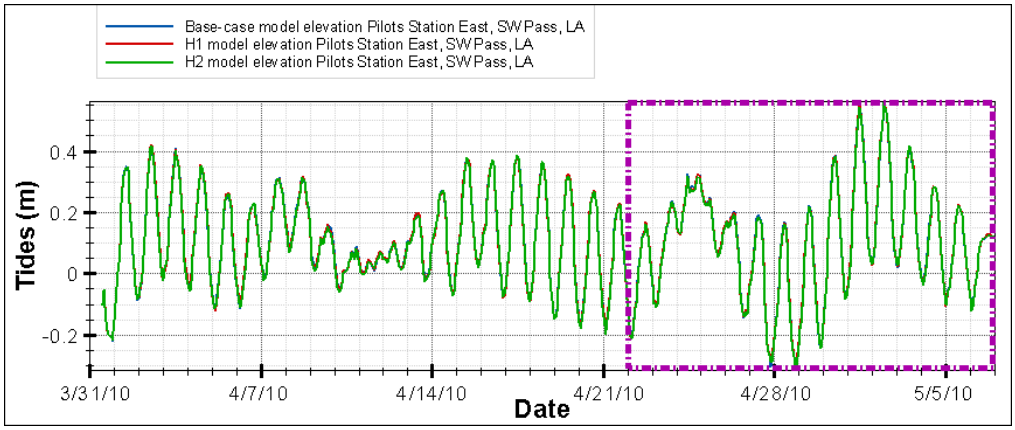

Figure 79 - A comparison of the tidal elevations (in meters) across the model scenarios (base-case, H1, and H2) at the SW Pass station for the entire simulation period. The winter storm period of 4/22/10 through 5/7/10 is bounded by the purple box.

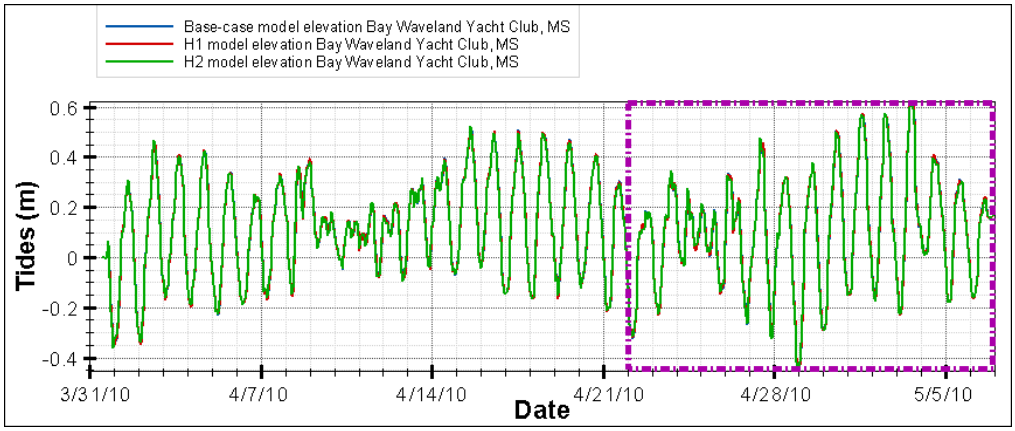

Figure 80 - A comparison of the tidal elevations (in meters) across the model scenarios (base-case, H1, and H2) at the Bay Waveland Yacht Club station for the entire simulation period. The winter storm period of 4/22/10 through 5/7/10 is bounded by the purple box.

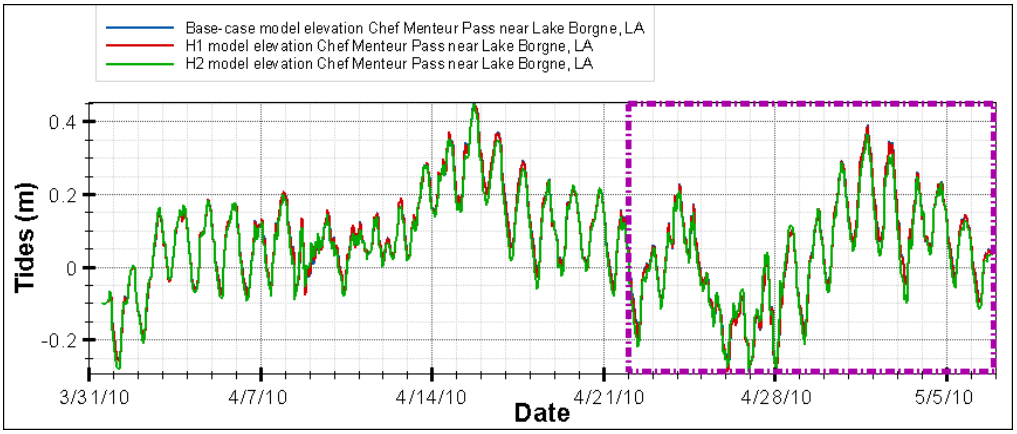

Figure 81- A comparison of the tidal elevations (in meters) across the model scenarios (base-case, H1, and H2) at the Chef Menteur Pass station for the entire simulation period. The winter storm period of 4/22/10 through 5/7/10 is bounded by the purple box.

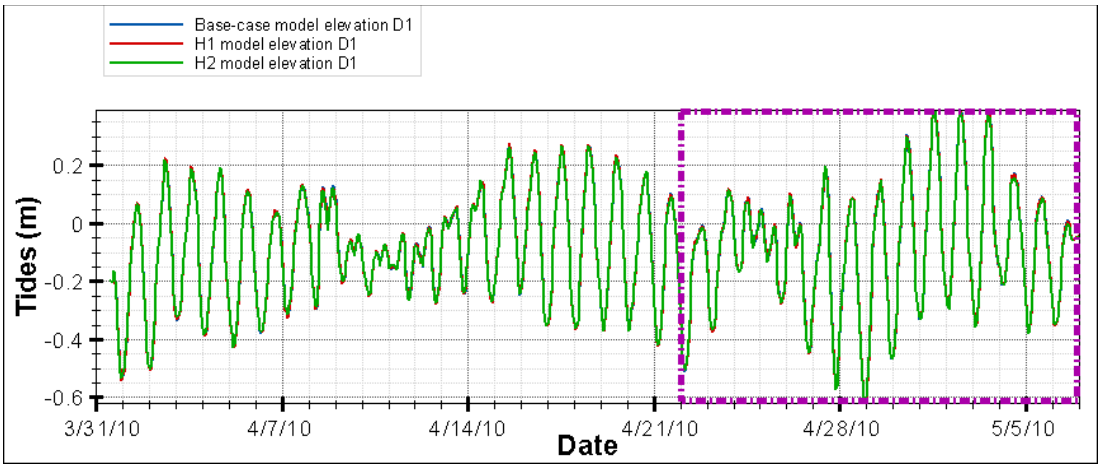

Figure 82- A comparison of the tidal elevations (in meters) across the model scenarios (base-case, H1, and H2) at the D1 station for the entire simulation period. The winter storm period of 4/22/10 through 5/7/10 is bounded by the purple box.

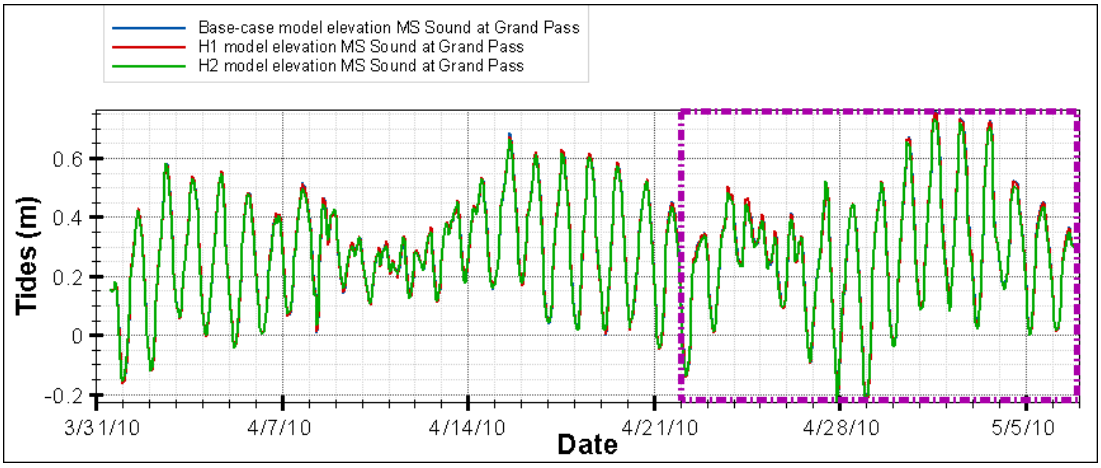

Figure 83- A comparison of the tidal elevations (in meters) across the model scenarios (base-case, H1, and H2) at the Mississippi Sound at Grand Pass station for the entire simulation period. The winter storm period of 4/22/10 through 5/7/10 is bounded by the purple box.

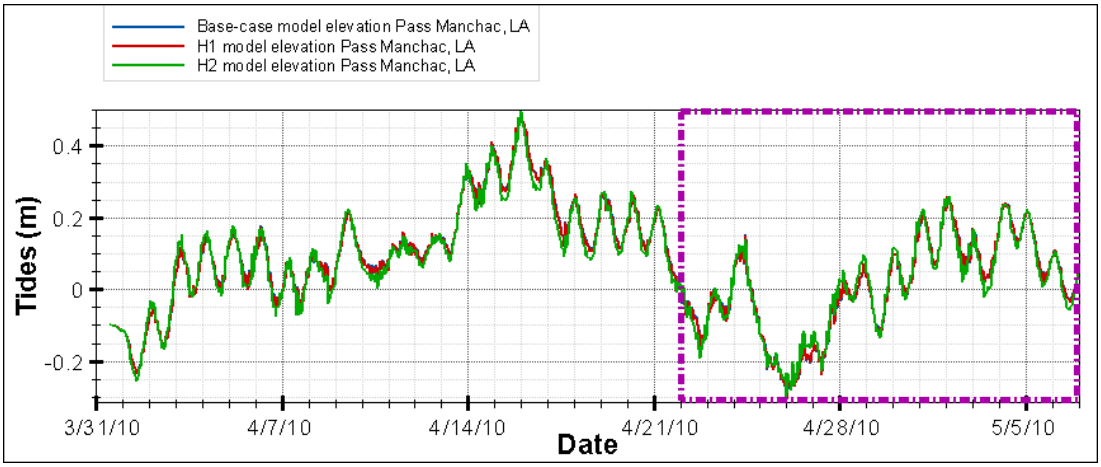

Figure 84- A comparison of the tidal elevations (in meters) across the model scenarios (base-case, H1, and H2) at the Pass Manchac station for the entire simulation period. The winter storm period of 4/22/10 through 5/7/10 is bounded by the purple box.

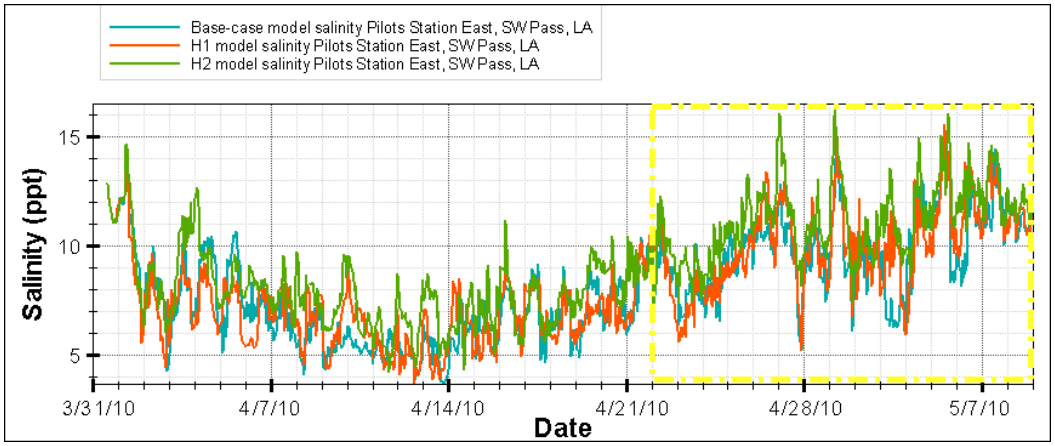

Figure 85 - A comparison of the salinity fluctuations (in ppt) across the model scenarios (base-case, H1, and H2) at the SW Pass station for the entire simulation period. The winter storm period of 4/22/10 through 5/7/10 is bounded by the yellow box.

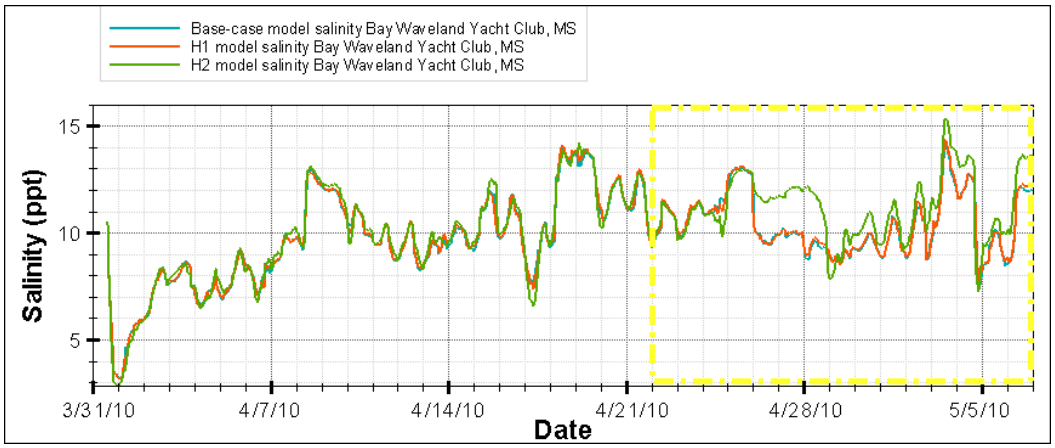

Figure 86 - A comparison of the salinity fluctuations (in ppt) across the model scenarios (base-case, H1, and H2) at the Bay Waveland Yacht Club station for the entire simulation period. The winter storm period of 4/22/10 through 5/7/10 is bounded by the yellow box.

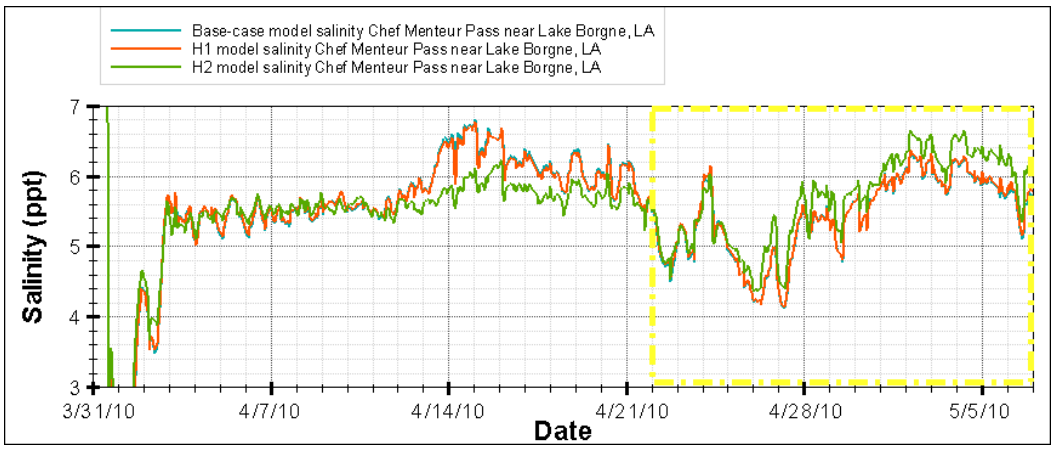

Figure 87 - A comparison of the salinity fluctuations (in ppt) across the model scenarios (base-case, H1, and H2) at the Chef Menteur Pass station for the entire simulation period. The winter storm period of 4/22/10 through 5/7/10 is bounded by the yellow box.

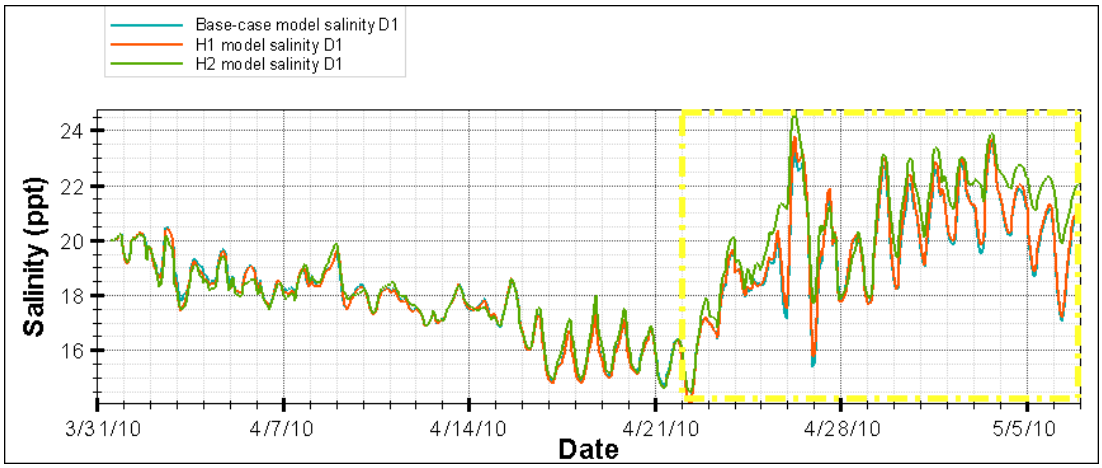

Figure 88 - A comparison of the salinity fluctuations (in ppt) across the model scenarios (base-case, H1, and H2) at the D1 station for the entire simulation period. The winter storm period of 4/22/10 through 5/7/10 is bounded by the yellow box.

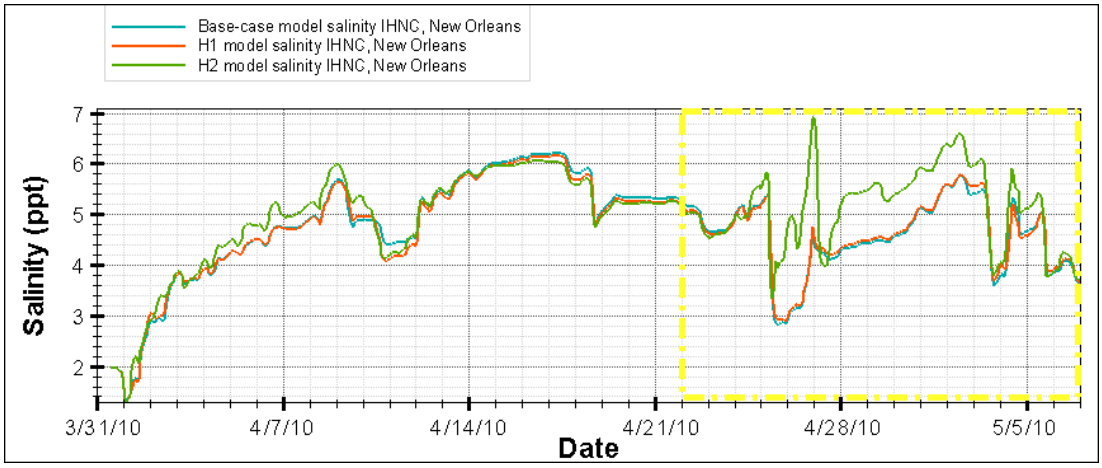

Figure 89 - A comparison of the salinity fluctuations (in ppt) across the model scenarios (base-case, H1, and H2) at the IHNC station for the entire simulation period. The winter storm period of 4/22/10 through 5/7/10 is bounded by the yellow box.

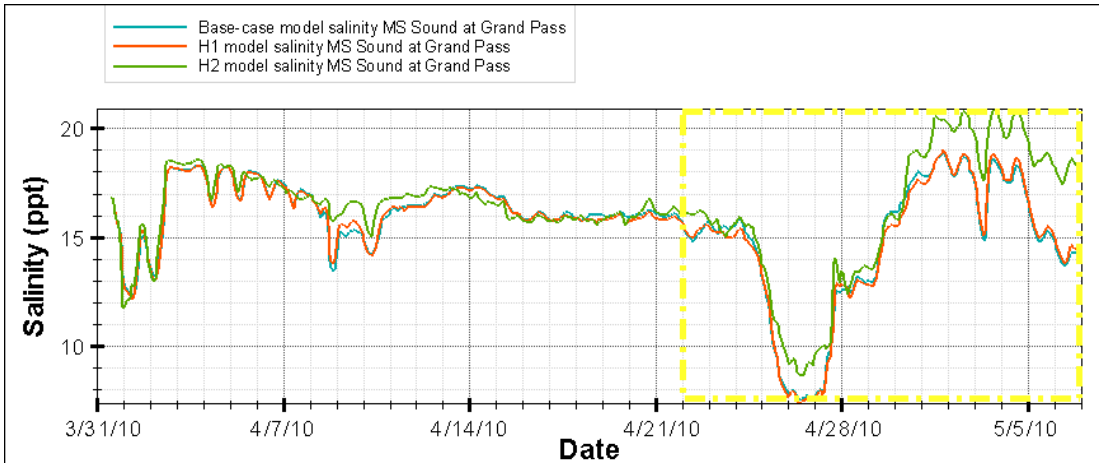

Figure 90 - A comparison of the salinity fluctuations (in ppt) across the model scenarios (base-case, H1, and H2) at the Mississippi Sound at Grand Pass station for the entire simulation period. The winter storm period of 4/22/10 through 5/7/10 is bounded by the yellow box.

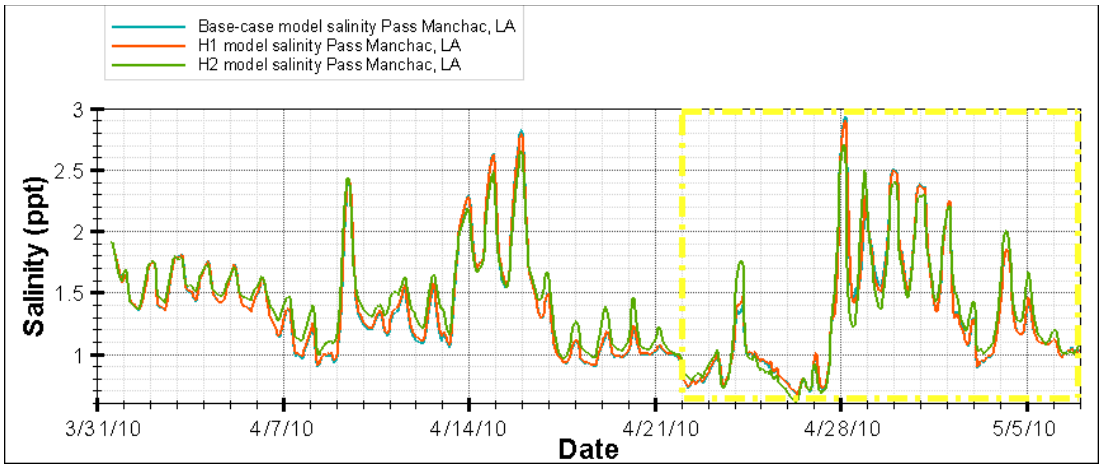

Figure 91 - A comparison of the salinity fluctuations (in ppt) across the model scenarios (base-case, H1, and H2) at the Pass Manchac station for the entire simulation period. The winter storm period of 4/22/10 through 5/7/10 is bounded by the yellow box.

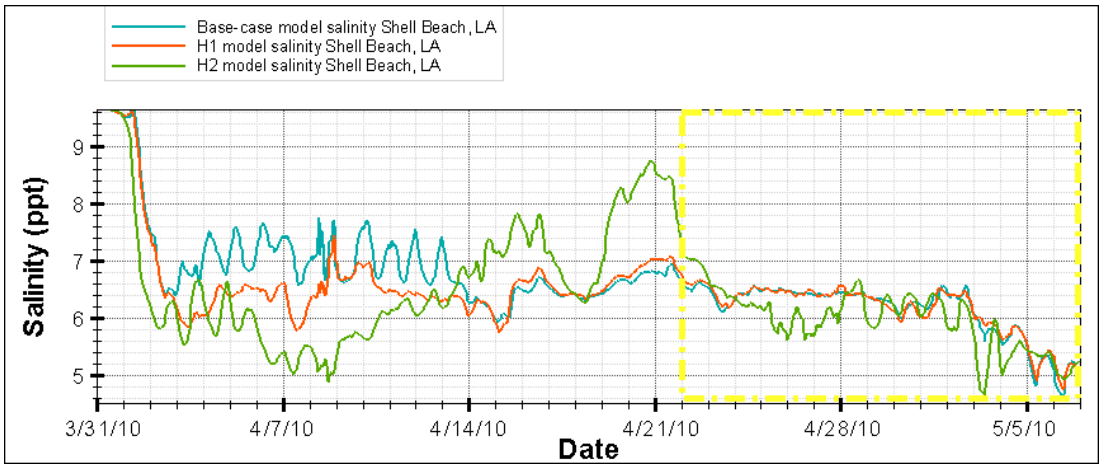

Figure 92 - A comparison of the salinity fluctuations (in ppt) across the model scenarios (base-case, H1, and H2) at the Shell Beach station for the entire simulation period. The winter storm period of 4/22/10 through 5/7/10 is bounded by the yellow box.

VITA

The author was raised in Covington, LA. She graduated as valedictorian of her Covington High class in May 2003 and began attending the University of New Orleans (UNO) as a Civil and Environmental Engineering student that fall. She began research work as an undergraduate student worker with Dr. Ioannis Georgiou and the Pontchartrain Institute for Environmental Sciences in February 2007. In December 2008, she graduated magna cum laude, earning a Bachelor's degree in Civil and Environmental Engineering. In the fall of 2008, she joined the UNO Earth and Environmental Science Masters' program as a Graduate Research Assistant for Dr. Ioannis Georgiou.